Scaling and balancing carbon fluxes in a heterogeneous tundra ecosystem of the Lena River Delta

Dissertation with the Aim of achieving a Doctoral Degree

Faculty of Mathematics, Informatics and Natural Sciences

Department of Earth Sciences

University of Hamburg

Norman Rößger

Hamburg, 2018

The dissertation was submitted on 31st January 2018 and has been accepted by the Department of Earth Sciences at the University of Hamburg on account of the evaluations of Prof. Dr. Lars Kutzbach and Dr. Mathias Göckede.

The disputation was held on 27th April 2018; the examination commission was composed of Prof. Dr. Lars Kutzbach, Dr. Mathias Göckede, Prof. Dr. Felix Ament, Prof. Dr. Eva-Maria Pfeiffer and Prof. Dr. Gerhard Schmiedl.

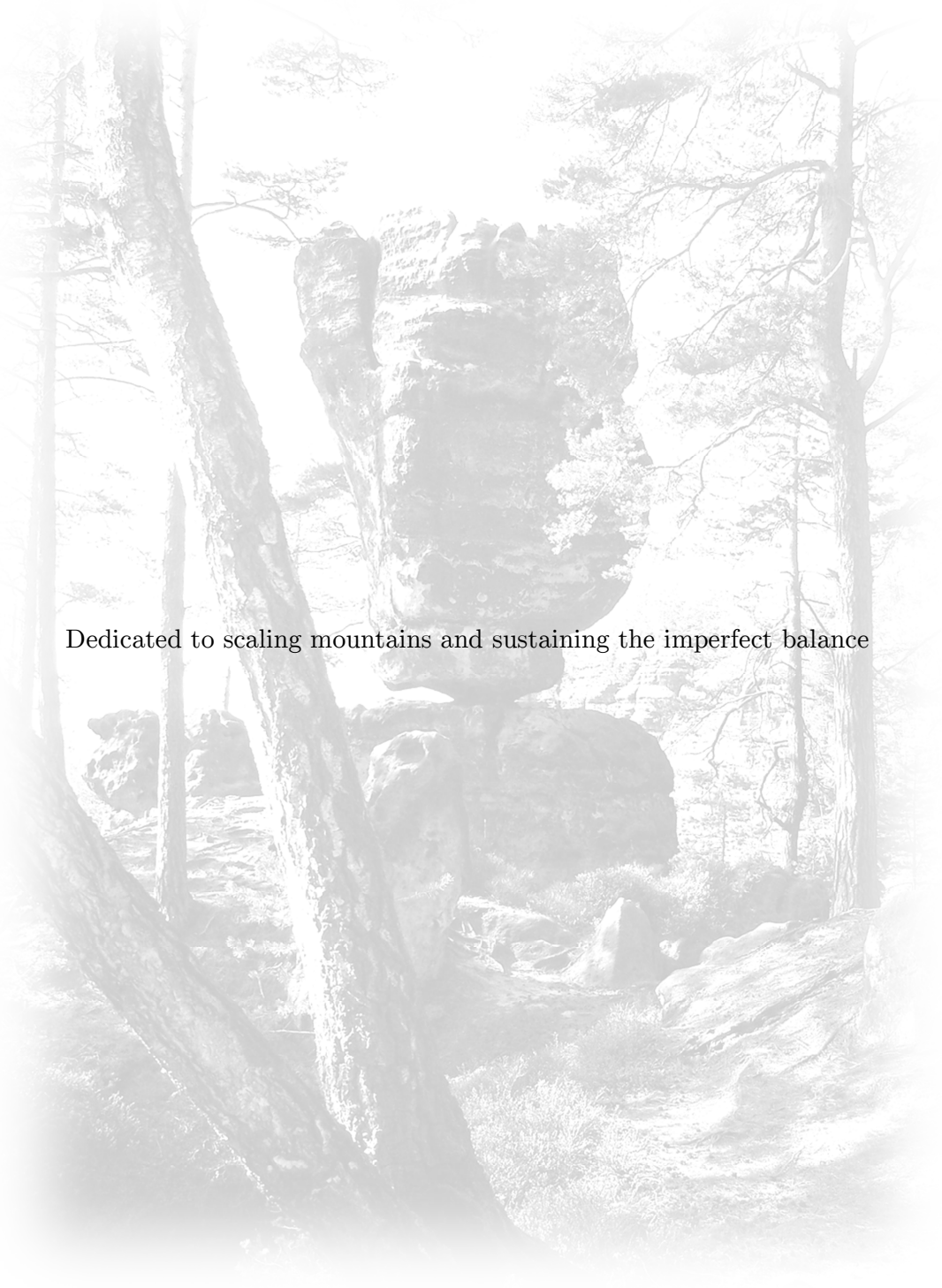

Dedicated to scaling mountains and sustaining the imperfect balance

Contents

Abstract

The Arctic tundra has been a carbon sink through the comprehensive accumulation of carbon in permafrost-affected soils over thousands of years. This carbon may be remobilised in the course of climate change, which occurs more pronounced in the Arctic region than on the global average. With growing concern about rising emissions of the greenhouse gases methane and carbon dioxide, the current and prospective carbon turnover of the terrestrial Arctic is regularly assessed. However, these assessments are associated with large uncertainties, which can (inter alia) be ascribed to both the general shortage of flux data from the vast and sparsely inhabited Arctic region, and the typically high spatiotemporal variability of carbon fluxes in tundra ecosystems. Thus, this study aims at providing robust carbon budgets from a Siberian tundra landscape that has not yet been investigated: an active flood plain situated in the Lena River Delta.

Applying the eddy covariance methodology, methane and carbon dioxide fluxes were determined during the growing seasons 2014 and 2015. These fluxes exhibited a great deal of temporal variability, which was, besides seasonal variation, largely the result of the pronounced spatial variability of soil and vegetation characteristics within the footprint. In order to explain this flux variability, the vegetation of the entire flood plain was classified utilising a high-resolution orthomosaic. In this process, three vegetation classes were designated accounting for shrubs (large *Salix* spp.), sedges (*Carex* spp., *Eriophorum* sp., *Equisetum* sp.) and intermediate (low *Salix* spp., *Carex* spp.) vegetation. These classes were well coupled with environmental variables such as soil moisture, moss properties and active layer depth. Hence, the vegetation served as an integrated proxy for potential soil-related flux drivers, whose contribution to the flux signal permanently varied according to the shifting source area. Applying footprint information in the form of relative contributions of vegetation classes to the flux signal facilitated the diagnostic modelling of the observed fluxes in the heterogeneous footprint to a large extent.

The modelling of the methane fluxes was based on three data-driven approaches: the automatically operating algorithms stepwise regression as well as artificial neural

network, and a mechanistic model, which utilises exponential relationships between the methane flux and both flux drivers soil temperature and friction velocity. On balance, the neural network exhibited the best model performance. However, verifying the models' generalisability revealed that the mechanistic model provided the most predictive power suggesting that this model best captured the causality between the methane flux and its drivers. After integrating the accordingly gap-filled time series, all models yielded footprint budgets that were very similar in magnitude; e.g. the footprint budget estimated with the mechanistic model amounted to 96.1 mmol m^{-2} (2014) and 104.3 mmol m^{-2} (2015).

The modelling of the carbon dioxide fluxes was based on another mechanistic model, which simultaneously computed the respiratory loss and the photosynthetic gain. This model was run with both flux drivers air temperature and irradiance, and it required a comprehensive calibration process, in the course of which its parameterisation repeatedly varied. Aggregating the time series after accordingly filling the data gaps yielded footprint budgets of -3.81 mol m^{-2} (2014) and -5.27 mol m^{-2} (2015).

For assessing the carbon sink/source strength of the tundra landscape in question, the footprint budgets of carbon dioxide were mostly applicable on account of the frequently minor differences between the flux rates of the vegetation classes. The footprint budgets of methane, however, lacked representativeness due to the sensor location bias, i.e. their strong dependence on tower location, measurement height and wind field conditions. For an unbiased appraisal of the sink/source function, a robust greenhouse gas budget of the entire flood plain was hence estimated.

Since both mechanistic models for methane carbon dioxide were additive models that account for the flux dynamics of each vegetation class, the footprint fluxes could be decomposed. For methane, this downscaling procedure partitioned the observed fluxes with a seasonal mean of 0.012 μmol m^{-2} s^{-1} into three individual vegetation class fluxes with the following mean rates: 0.0004 μmol m^{-2} s^{-1} for shrubs, 0.052 μmol m^{-2} s^{-1} for sedges and 0.018 μmol m^{-2} s^{-1} for intermediate vegetation. While these individual methane fluxes respectively featured similar seasonal courses for both years, the downscaling procedure unveiled a differing seasonality of the individual fluxes for carbon dioxide. In this process, the observed fluxes with a seasonal mean of -0.61 μmol m^{-2} s^{-1} were separated into two individual fluxes, whose mean rates were as follows: -0.79 μmol m^{-2} s^{-1} for shrubs and -0.53 μmol m^{-2} s^{-1} for both sedges and intermediate vegetation together. During the comparatively warm spring in 2014, the shrubs exhibited a considerably greater net uptake than the sedges. On the contrary, shrubs and sedges displayed a more similar net uptake during the climatologically usual measurement period in 2015. This varying ratio of net uptakes between the vegetation classes indicates a seasonally varying implication of

the sensor location bias; i.e. climatologically unusual conditions might adversely affect the representativeness of a footprint due to sharpened contrasts between vegetation classes.

The downscaled fluxes in turn formed the initial data for the upscaling procedure, which was based on the area-weighted projection of the cumulative vegetation class-specific fluxes. While the methane release for the entire flood plain was estimated at 0.171 Mmol and 0.177 Mmol for 2014 and 2015, respectively, the carbon dioxide net uptake was estimated at -4.42 Mmol and -6.17 Mmol. The conversion of the methane budgets according to their global warming potential yielded a greenhouse gas sink strength of -2.31 ± 0.64 Mmol CO_2 eq in 2014 and -3.98 ± 0.78 Mmol CO_2 eq in 2015. This carbon turnover, which is larger than at many other Arctic sites, can be attributed to the annual spring flood and the associated fluvial deposition of both fresh organic matter and nutrients, which enhance productivity and microbial breakdown.

Alternatively, the footprint budgets were simply projected on the flood plain: these subsidiary budgets of methane and carbon dioxide were, respectively, on average roughly 42 % and 4 % lower than the adequately estimated flood plain budgets utilising the preceding flux decomposition. Thus, the simple, commonly applied upscaling method overestimated the greenhouse gas sink strength in great measure. This comparison emphasises the necessity of considering the surface heterogeneity for modelling and balancing carbon flux dynamics in heterogeneous tundra regions and potentially other biomes with heterogeneous ecosystems, which the advanced scaling methodology of this study could also be applicable to.

Key Findings

- The vegetation served as an integrated proxy for soil-related flux drivers, and hence explained a great deal of the temporal variability in the observed fluxes.
- The spatial variability was more distinct for methane fluxes than carbon dioxide fluxes, which were subject to a varying implication of the sensor location bias.
- The observed fluxes, which integrated across a heterogeneous surface, could be downscaled into reliable flux rates accounting for multiple vegetation classes.
- The carbon dioxide net uptake dominated the robust greenhouse gas balance of the entire flood plain, which formed a sink during both growing seasons.
- The straightforward upscaling of footprint budgets led, compared to the robust balances, to a substantial overestimation of the greenhouse gas sink strength.

Zusammenfassung

Die arktische Tundra ist seit Jahrtausenden eine Kohlenstoffsenke auf Grund der Einlagerung beträchtlicher Mengen von Kohlenstoff in den Permafrostböden. Dieser gespeicherte Kohlenstoff ist von großer Bedeutung für das globale Klima, da dessen Freisetzung in Form von Methan und Kohlenstoffdioxid den in der Arktis ohnehin verstärkten Klimawandel weiter beschleunigen könnte. Grundlage zur Schätzung dieser Freisetzung in Gegenwart und Zukunft bilden Kohlenstoffbilanzen, welche jedoch meist mit großen Ungenauigkeiten behaftet sind. Diese Ungenauigkeiten können insbesondere auf den generellen Mangel von notwendigen Eingangsdaten aus den weiten und dünn besiedelten Gegenden der Arktis zurückgeführt werden, aber auch die typischerweise hohe räumlich-zeitliche Variabilität von Kohlenstoffflüssen in der Tundra spielt in diesem Zusammenhang eine übergeordnete Rolle. Ziel dieser Arbeit ist daher, belastbare Kohlenstoffbilanzen eines bisher unerforschten Ökosystems in der sibirischen Tundra zu schätzen: eine Überflutungsebene im Lena Delta.

Unter Anwendung der Eddy Kovarianz Methode wurden während der Vegetationsperiode in 2014 und 2015 Methan- und Kohlenstoffdioxidflüsse bestimmt. Diese Flüsse wiesen eine hohe zeitliche Variabilität auf, welche sich, neben den jahreszeitlichen Schwankungen, insbesondere aus der räumlichen Variabilität der Boden- und Vegetationseigenschaften innerhalb des Footprints (d.h. des beprobten Bereichs um den Messturm) ergab. Zur Erklärung dieser Variabilität wurde die Vegetation der gesamten Überflutungsebene mit Hilfe eines hochaufgelösten Orthomosaiks klassifiziert. Die dabei verwendeten Klassen bilden Büsche (hohe *Salix* spp.), Seggen (*Carex* spp., *Eriophorum* sp., *Equisetum* sp.) und Übergangsvegetation (niedrige *Salix* spp., *Carex* spp) ab. Diese drei Klassen waren eng mit den Parametern Bodenfeuchte, Mooseigenschaften und Auftautiefe verbunden, sodass die Vegetation als eine integrierend stellvertretende Größe für diese Steuerparameter diente. Deren sich ständig verändernde Zusammensetzung im Flusssignal konnte mittels Footprint-Informationen in Form der relativen Anteile der Vegetationsklassen im Flusssignal abgebildet werden, was die diagnostische Modellierung der Flüsse in dem heterogenen Footprint in hohem Maße gefördert hat.

Die Modellierung der Methanflüsse basierte auf drei Daten-getriebenen Ansätzen: die zwei automatisierten Algorithmen stufenweise Regression und künstliches neuronales Netzwerk sowie ein mechanistisches Modell, das exponentielle Zusammenhänge zwischen Methanfluss und den beiden Steuergrößen Bodentemperatur und Schubspannungsgeschwindigkeit verwendet. Dabei wies das neuronale Netzwerk die höchste Modellgüte auf. Die Überprüfung der Generalisierbarkeit der Modelle zeigte jedoch, dass das mechanistische Modell die meiste Vorhersagekraft besitzt, sodass dieses Modell den kausalen Zusammenhang zwischen Methanfluss und Steuergrößen am besten erfasst hat. Die nach Aufsummierung der entsprechend gefüllten Zeitreihen erhaltenen Bilanzen waren für alle drei Modelle sehr ähnlich; so betrugen zum Beispiel die mit dem mechanistischen Modell geschätzten Footprint-Bilanzen 96.1 mmol m^{-2} (2014) und 104.3 mmol m^{-2} (2015).

Die Modellierung der Kohlenstoffdioxidflüsse basierte auf einem weiteren mechanistischen Modell, welches die respiratorische Freisetzung und die photosynthetische Bindung von Kohlenstoffdioxid gleichzeitig berechnete. Dieses Modell wurde mit den beiden Steuergrößen Lufttemperatur und Strahlungsintensität angetrieben. Weiterhin erforderte es eine umfangreiche Kalibrierung, in deren Verlauf acht Modellparameter ausgegeben wurden, welche ökophysiologische Eigenschaften charakterisierten. Die Aufsummierung der entsprechend lückengefüllten Zeitreihen ergab Footprint-Bilanzen von -3.81 mol m^{-2} (2014) und -5.27 mol m^{-2} (2015).

Zur Beurteilung der Senken- bzw. Quellenfunktion dieser heterogenen Tundra waren die Footprint-Bilanzen für Kohlenstoffdioxid meistens geeignet, da die Unterschiede zwischen den Flüssen der Vegetationsklassen vorwiegend geringerer Größenordnung waren. Den Footprint-Bilanzen für Methan fehlte es jedoch an Repräsentativität auf Grund ihrer starken Abhängigkeit von der Position des Flussturms, der Messhöhe und den Windfeldbedingungen. Für eine unverfälschte Bewertung der Senken- bzw. Quellenstärke wurde daher eine belastbare Gesamtkohlenstoffbilanz für die gesamte Überflutungsfläche geschätzt.

Da die mechanistischen Modelle für Methan und Kohlenstoffdioxid additive Modelle sind, welche die Dynamik der Flüsse in den einzelnen Vegetationsklassen erfassen, konnten die Footprint-Flüsse zerlegt werden. Diese Runterskalierung der beobachteten Methanflüsse, welche im saisonalen Mittel 0.012 µmol m^{-2} s^{-1} betrugen, ergab folgende mittleren Flussraten für die einzelnen Vegetationsklassen: 0.0004 µmol m^{-2} s^{-1} für Büsche, 0.052 µmol m^{-2} s^{-1} für Seggen und 0.018 µmol m^{-2} s^{-1} für die Übergangsvegetation. Während diese einzelnen Methanflüsse in beiden Jahren jeweils einem ähnlichen Verlauf folgten, ergab die Flusszerlegung eine partiell unterschiedliche Saisonalität der Kohlenstoffdioxidflüsse für die einzelnen Vegetationsklassen. Die beobachteten Flüsse, welche im saisonalen Mittel -0.61 µmol m^{-2} s^{-1} betrugen, wurden in zwei einzelne Flüsse mit folgenden mittleren Flussraten aufge-

trennt: -0.79 μmol m^{-2} s^{-1} für Büsche und -0.53 μmol m^{-2} s^{-1} für Seggen und Übergangsvegetation zusammen. Während des vergleichsweise sehr warmen Frühlings in 2014 wiesen die Büsche eine wesentlich höhere Nettoaufnahme als die Seggen auf. Im Gegensatz dazu zeigten Büsche und Seggen eine ähnliche Nettoaufnahme während des klimatologisch durchschnittlichen Messzeitraums in 2015. Diese variable Ähnlichkeit zwischen den Nettoaufnahmen beider Vegetationsklassen weist auf eine Wetter-induzierte, zeitliche Einschränkung der Repräsentativität des Footprint hin.

Die Plausibilität der zerlegten Flüsse wurde anhand folgender Maßnahmen validiert: (i) deren Vergleich mit Flüssen, welche durch Haubenmessungen ermittelt wurden, (ii) deren Vergleich mit beobachteten Flüssen, welche erhalten wurden, wenn eine Vegetationsklasse die beprobte Fläche des Eddy Kovarianz Systems deutlich dominierte, (iii) deren Zusammenhang mit einem phänologischen Grünheitsindex, welcher mittels digitaler Zeitrafferaufnahmen des Footprints bestimmt wurde, (iv) der Vergleich deren acht Modellparameter mit Parametern, welche an anderen Standorten festgestellt wurden.

Die runterskalierten Flüsse bildeten den Ausgangspunkt für die Hochskalierung, welche auf einer Flächen-gewichteten Projektion der aufsummierten Flüsse aller Vegetationsklassen basierte. Während die Methanabgaben der gesamten Überflutungsebene auf jeweils 0.171 Mmol und 0.177 Mmol für 2014 und 2015 geschätzt wurden, betrugen die geschätzten Kohlenstoffdioxidaufnahmen jeweils -4.42 Mmol und -6.17 Mmol. Die Umrechnung der Methanbilanzen zur Berücksichtigung deren Treibhauspotentials ergaben eine robuste Schätzung der Treibhausgasbilanz von -2.31 ± 0.64 Mmol CO_2 eq in 2014 und -3.98 ± 0.78 Mmol CO_2 eq in 2015. Dieser im Vergleich zu vielen anderen arktischen Standorten hohe Kohlenstoffumsatz kann auf das jährliche Frühjahrshochwasser zurückgeführt werden, in dessen Verlauf frisches organisches Material und Nährstoffe abgelagert werden, welche die Aufnahme und Freisetzung von Treibhausgasen fördern.

Alternativ wurden Footprint-Bilanzen einfach auf die Überflutungsebene projiziert: die auf diese Weise geschätzten Methan- und Kohlenstoffdioxidbilanzen waren jeweils um 42 % und 4 % niedriger als die belastbaren Kohlenstoffbilanzen, welche mit der vorangegangenen Flusszerlegung geschätzt wurden. Demzufolge hat diese einfache sowie übliche Hochskalierung der Footprint-Bilanzen die Senkenfunktion für Treibhausgase in hohem Maße überschätzt. Dieser Vergleich verdeutlicht die Notwendigkeit der Berücksichtigung der heterogenen Unterlage bei der Modellierung und Bilanzierung von Kohlenstoffflüssen in heterogenen Tundren und darüber hinaus anderen Ökosystemen mit heterogener Unterlage, für welche die in dieser Studie entwickelte Skalierungsmethodik ebenfalls Anwendung finden kann.

Kernaussagen

- Die Vegetation diente als eine integrierende Hilfsgröße für potentielle Flusssteuerungsparameter und erklärte einen Großteil der zeitlichen Variabilität in den beobachteten Flüssen.
- Die räumliche Variabilität der Methanflüsse war wesentlich größer als die der Kohlenstoffdioxidflüsse, deren Repräsentativität im Footprint jedoch zeitweise eingeschränkt war.
- Die beobachteten Flüsse, welche über eine heterogene Fläche integriert wurden, konnten in plausible Flüsse, welche die Dynamik einzelner Vegetationsklassen abbilden, runterskaliert werden.
- Die Kohlenstoffdioxidflüsse dominierten die belastbar geschätzte Treibhausgasbilanz der gesamten Überflutungsebene, welche eine Senke während beider Vegetationsperioden bildete.
- Die direkte Hochskalierung der Footprint-Bilanzen hätte, im Vergleich zu den belastbaren Bilanzen, zu einer beträchtlichen Überschätzung der Senkenstärke der Überflutungsebene geführt.

Keywords

Arctic, tundra, permafrost, eddy covariance, heterogeneous footprint, sensor location bias, methane flux, carbon dioxide flux, stepwise regression, neural network, down- and upscaling, photosynthesis, respiration, phenocam

Nomenclature

A	Area	(m^2)
F_{CH4}	Methane flux	($\mu mol\ m^{-2}\ s^{-1}$)
$F_{CH4,1}$	Methane flux of vegetation class 1	($\mu mol\ m^{-2}\ s^{-1}$)
$F_{CH4,2}$	Methane flux of vegetation class 2	($\mu mol\ m^{-2}\ s^{-1}$)
$F_{CH4,3}$	Methane flux of vegetation class 3	($\mu mol\ m^{-2}\ s^{-1}$)
F_{CO2}	Carbon dioxide flux	($\mu mol\ m^{-2}\ s^{-1}$)
$F_{CO2,1}$	Carbon dioxide flux of vegetation class 1	($\mu mol\ m^{-2}\ s^{-1}$)
$F_{CO2,2\&3}$	Carbon dioxide flux of vegetation class 2 & 3	($\mu mol\ m^{-2}\ s^{-1}$)
GPP	Gross primary productivity	($\mu mol\ m^{-2}\ s^{-1}$)
MAE	Mean absolute error	(*)
ME	Mean error	(*)
NEE	Net ecosystem exchange	($\mu mol\ m^{-2}\ s^{-1}$)
P	Probability for statistical hypothesis testing	(-)
P_{max}	Maximum photosynthetic potential	($\mu mol\ m^{-2}\ s^{-1}$)
PPFD	Photosynthetic photon flux density	($\mu mol\ m^{-2}\ s^{-1}$)
Q_{10}	Temperature sensitivity	(-)
R^2	Coefficient of determination	(-)
R^2_{adj}	Adjusted coefficient of determination	(-)
R_{base}	Basal respiration	($\mu mol\ m^{-2}\ s^{-1}$)
RMSE	Root mean square error	(*)
SLB	Sensor location bias	(-)
TER	Total ecosystem respiration	($\mu mol\ m^{-2}\ s^{-1}$)
T_{air}	Air temperature	(°C)
T_{mean}	Mean temperature	(°C)
T_{ref}	Reference temperature	(°C)
T_{soil}	Soil temperature	(°C)
VPD	Vapour pressure deficit	(Pa)

a	Modelling coefficient	(μmol m^{-2} s^{-1})
b	Modelling coefficient	($°C^{-1}$)
c	Modelling coefficient	(m^{-1} s)
g_{cc}	Chromatic coordinate for green colour	(-)
i	Index of summation	(-)
n	Number of samples	(-)
u*	Friction velocity	(m s^{-1})
ΔT	Temperature spread	(°C)
Ω	Relative contribution of vegetation class	(-)
α	Initial quantum efficiency	(-)
γ	Scaling factor in Q_{10} relationships	(°C)

Remark: * indicates the dependency of the dimension on the nature of the variable.

Abbreviations

ATP	Adenosine triphosphate
CC	Closed chamber
DoY	Day of year
EC	Eddy covariance
GTP	Global temperature change potential
GWP	Global warming potential
IPCC	Intergovernmental panel on climate change
MM	Mechanistic model
NDVI	Normalised difference vegetation index
NN	Neural network
RCP	Representative concentration pathway
SR	Stepwise regression
eq	Equivalent
insig	Insignificant
p	Parameter
sig	Significant
t	Threshold

1. Introduction

1.1. Background

Since ancient times, when the world had been a barren, inanimate place, life has been developed in the course of evolution. As a result, today's animate beings present a massive abundance of shapes and colours. This vast variety could be attributed to complex series of basic molecules. However, it is one element only, which the diversity of nature is based upon: the carbon. This element forms the foundation of organic compounds and, hence, is of utter importance for all life on earth. Carbon also appears in various inorganic compounds and, thus, exists in all spheres of the world. Comprehending and quantifying its transport and conversion processes is crucial for understanding the earth and its ecosystems.

1.1.1. Permafrost-affected soils and carbon stocks

Permafrost is defined as ground, whose temperature remains below the freezing point of water for at least two consecutive years (Osterkamp, 2001). This definition corresponds to an area that covers between 12.8 % and 17.8 % of the exposed land area of the northern hemisphere (Zhang et al., 2000). Depending on climatic conditions (air temperature and snowfall in past and present) and local factors such as altitude, aspect and shelter, a spatial distribution has been developed involving four permafrost classes: continuous, discontinuous, sporadic and isolated (Figure 1). In the continuous zone, the permafrost thickness typically ranges between 350 and 650 m; larger depths down to 1450 m formed in Siberia as a consequence of very cold winters with little glaciation in the glacial ages (Schuur et al., 2008). Further south in the discontinuous zone, the thickness usually extends from less than one metre down to 50 m (Yershov, 1998). The top of the permafrost-affected soils thaw and refreeze annually forming the active layer, whose thickness varies between a few centimetres and several metres depending on snow cover and melt timing, air temperature, water content, soil properties as well as cover and insulation trough vegetation (Schuur et al., 2008).

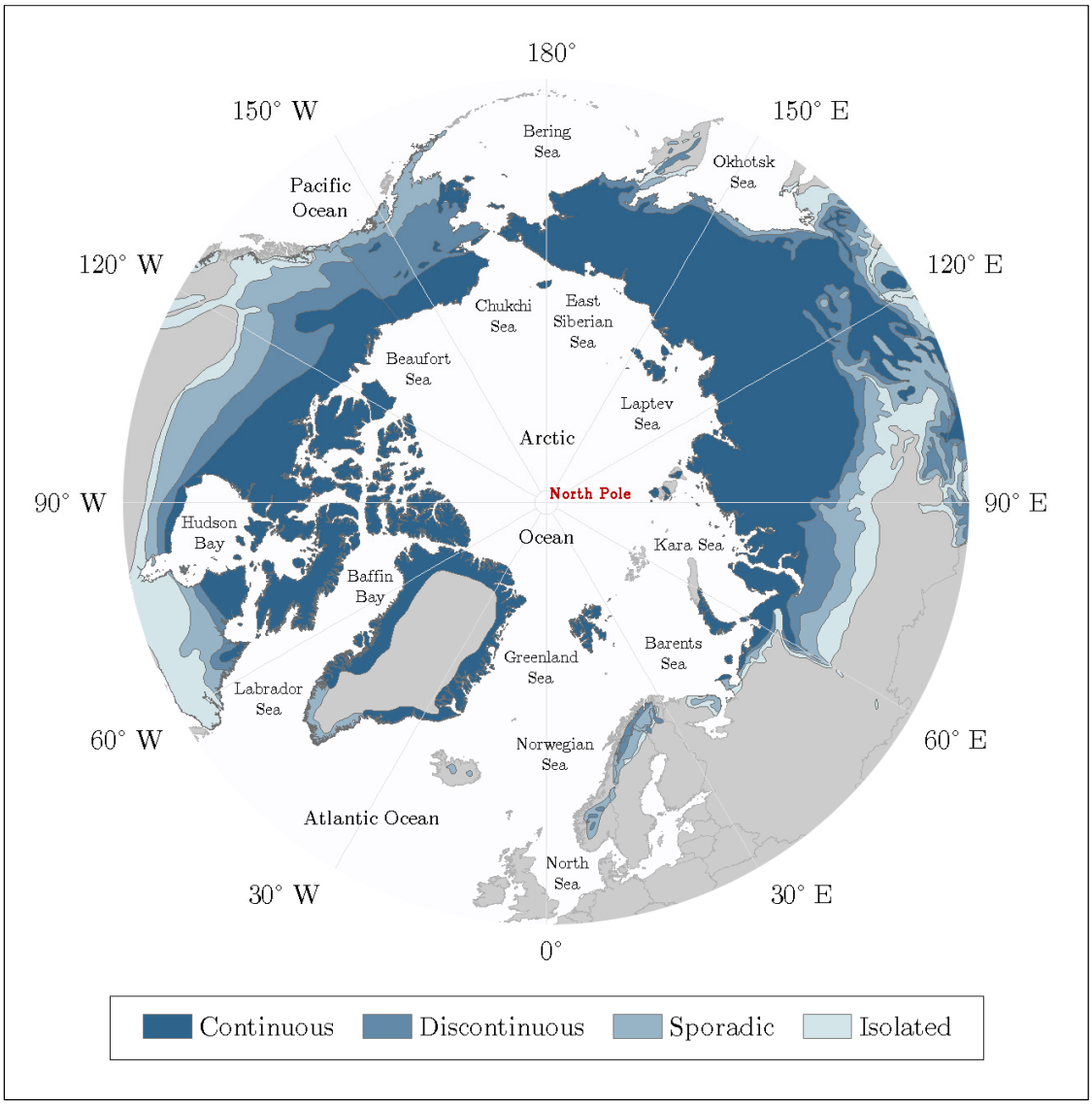

Figure 1 Circumpolar distribution of four permafrost zones (modified from IPA, 1998). Permafrost occurs, where the ground remains frozen for at least two years in a row (van Everdingen, 2005). If more than 90 % of the ground in a region is frozen, continuous permafrost prevails, whereas discontinuous permafrost is present, if 35 % to 90 % of the ground is frozen. Regions with a very fragmentary distribution of permafrost can be classified into zones with sporadic or isolated permafrost. Besides the terrestrial permafrost, sub-sea permafrost exists underneath the Arctic Ocean, in particular off the coast of Siberia.

Large parts of the permafrost area coincide with the Arctic tundra, which is situated north of the boreal treeline, stretching over 8 % of the global land surface (McGuire et al., 2012). The underlying permafrost forms a carbon

pool of global relevance; the latest estimate of soil organic carbon stored in the circumpolar permafrost region amounts to approximately 1300 ± 200 Gt (Hugelius et al., 2014). Roughly 500 Gt of this estimate can be assigned to the active layers or deeper taliks (non-frozen ground layers in permafrost areas) while the remaining around 800 Gt can be attributed to perennially frozen ground (Figure 2). The accumulation of these large quantities of car-

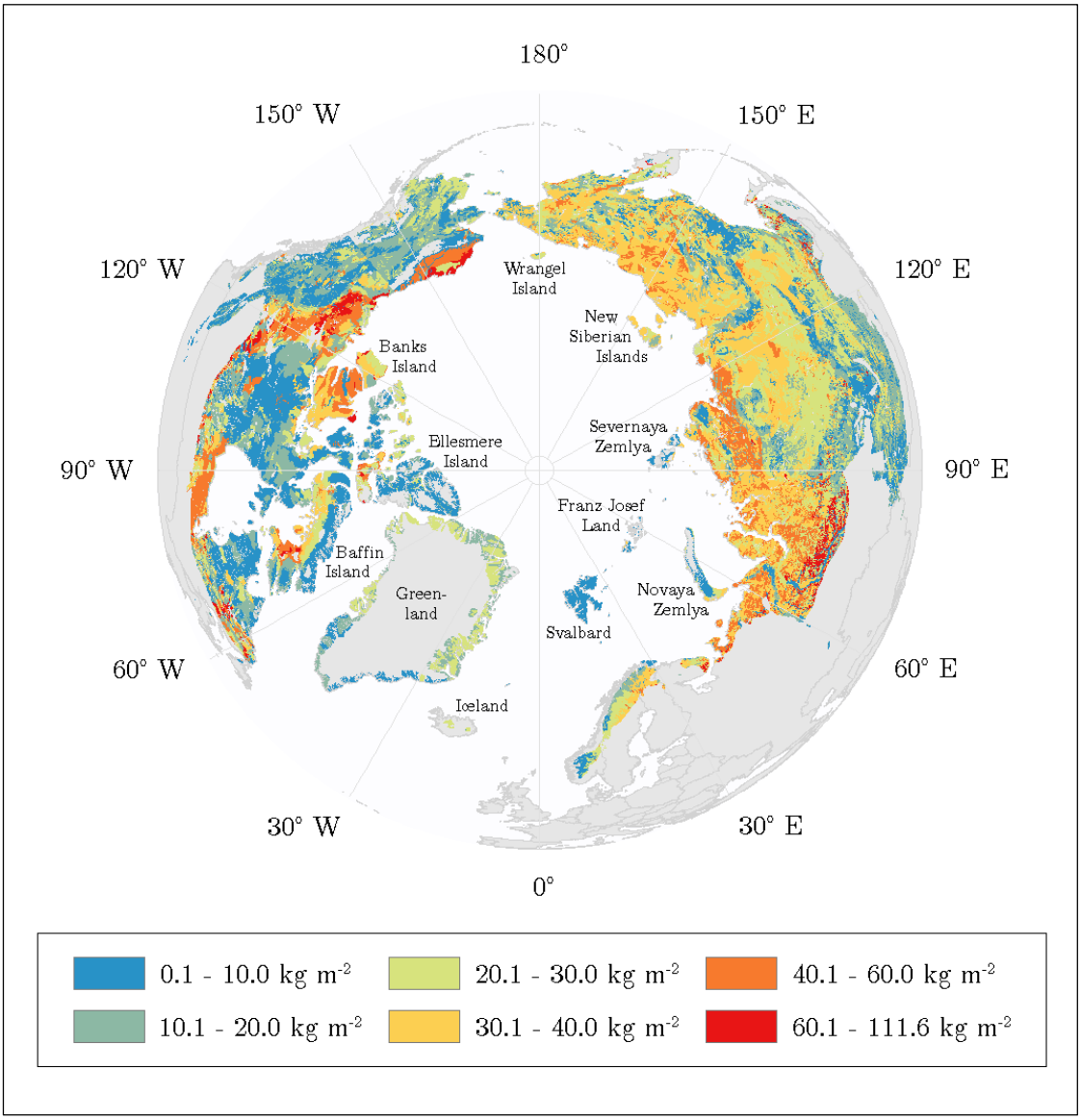

Figure 2 Circumpolar distribution of soil organic carbon (0–1 m depth) in the northern permafrost region (modified from Hugelius et al., 2013). Low temperatures and water-logged conditions in permafrost systems have reduced decomposition rates, which resulted in the accumulation of large carbon stocks.

bon occurred through the impeded decomposition of organic matter during the Holocene and Pleistocene (Gajewski et al., 2001). The hampered breakdown was due to both low temperatures and high water contents in the soil caused by the underlying permafrost that prevents downward infiltration (Ström et al., 2003). Thus, tundra ecosystems have historically been carbon sinks (Kutzbach et al., 2007b). However, large fractions of this carbon pool may be remobilised in response to a warming climate making the tundra a key ecosystem for climate change (Schuur et al., 2008).

1.1.2. Methane flux

On account of both frequently high soil water contents and the enormous carbon stock, tundra ecosystems hold the potential for substantial methane emissions, which adversely affect their carbon sink strength. In fact, wetlands constitute the largest natural source of methane, while anthropogenic sources are even greater in magnitude encompassing rice fields, ruminants, landfills and waste (Ciais et al., 2013). The largest important sink represents the methane oxidation through tropospheric hydroxyl radicals (Cicerone and Oremland, 1988).

Methane is produced by methanogenic bacteria metabolising substrates under anaerobic conditions. Over the course of mineralising soil organic matter in the absence of oxygen (O_2), intermediate products such as hydrogen (H_2), carbon dioxide (CO_2) and acetate (CH_3COOH) are produced (Lai, 2009). These compounds form the starting materials for the formation of methane (CH_4) utilising two different ways (Whalen, 2005). There is the hydrogenotrophic methanogenesis, where hydrogen is utilised as an electron donor for the reduction of carbon dioxide:

$$4H_2 + CO_2 \rightarrow CH_4 + 2H_2O \quad (1)$$

And there is the acetoclastic methanogenesis, where acetate is dismutated to methane and carbon dioxide:

$$CH_3COOH \rightarrow CH_4 + CO_2 \quad (2)$$

Both production ways occur in Arctic wetlands, and the dominance of either carbon dioxide reduction or acetate cleavage was found to vary between organic and mineral soils (Lee et al., 2012; Vaughn et al., 2016). The produced methane may migrate through the soil encountering aerobic zones, where methanotrophic bacteria partially oxidise the methane:

$$CH_4 + 2O_2 \rightarrow CO_2 + H_2O \quad (3)$$

The highest methanotrophic activity occurs at the interface of aerobic/anaerobic layers due to the optimal ratio of methane, oxygen and substrates (Dedysh, 2002). The oxidation efficiency was found to largely vary in high-latitude wetlands ranging between 30 % and 99 % (Knoblauch et al., 2015; Reeburgh et al., 1993). If methane is released to the atmosphere

after its formation, it is transported via three different ways:

- Diffusion: Following the production of methane in anaerobic peat layers, a methane concentration gradient evolves towards the atmosphere, which drives the comparatively slow transport via molecular diffusion (Lai, 2009).
- Ebullition: High rates of methanogenesis may lead to a supersaturation of methane in the pore water. When the partial pressure of dissolved methane exceeds the hydrostatic pressure, gas bubbles are formed and often remain trapped by adhesive forces (Chanton and Whiting, 1995). As a consequence of changes in water table and air pressure, the methane bubbles intermittently escape to the atmosphere (Whalen, 2005).
- Plant-mediated: Some vascular wetland plants develop internal gas spaces to provide aeration for submerged roots and rhizomes (Joabsson et al., 1999). This aerenchymatous tissue can also serve as a gas conduit for a transfer of methane towards the atmosphere whilst bypassing the aerobic, oxidised soil zone of methane consumption (Whalen, 2005). This vascular pathway enables a comparatively efficient methane transport (Lai, 2009).

Upon emission, methane remains in the atmosphere on average for 12 years and acts as a powerful greenhouse gas with a global warming potential of 34 times that of carbon dioxide, when climate carbon feedbacks are considered over 100 years (Myhre et al., 2013). Following carbon dioxide, methane is the second most important greenhouse gas, accounting for approximately 17 % of the rise in global radiative forcing due to raised concentrations of greenhouse gases since the pre-industrial era (NOAA, 2016). From 1750 to the present day, the global surface methane concentration has risen from 722 ppb to 1859 ppb (NOAA, 2018b; Stocker et al., 2013).

1.1.3. Carbon dioxide flux

While methane is mostly emitted into the atmosphere (apart from a few exceptions), carbon dioxide is exchanged between the atmosphere and tundra ecosystem in both directions as a result of two opposing mechanisms: respiratory loss and photosynthetic gain.

Respiration embraces a set of metabolic reactions, in the course of which biochemical energy from organic compounds is, with the aid of oxygen, transferred to endogenous energy carriers (ATP) whilst releasing carbon dioxide to the atmosphere. It is carried out by autotrophs (above-ground biomass and roots) and heterotrophs (animals and microbes in the soil) for growth and maintaining their metabolism (Luo and Zhou, 2006). In contrast to the anaerobic decomposition of soil organic

matter, in the course of which methane is produced, the aerobic decomposition yields considerably more energy and occurs generally at higher rates (Megonigal et al., 2004).

Photosynthesis denotes the generation of organic compounds through the removal of carbon dioxide from the atmosphere by primary producers utilising light as a source of energy and releasing oxygen as an end product. In this sense, the carbon of the extracted carbon dioxide is stored in the plant biomass and is, after the withering of the plant, either preserved as soil organic matter in permafrost-affected soils or returned to the atmosphere through microbial decomposition.

Carbon dioxide is the largest single contributor to the rise in global radiative forcing from greenhouse gases since pre-industrial times (Myhre et al., 2013). The additional anthropogenic radiative forcing due to rising concentrations of all greenhouse gases amounts to 2.83 W m^{-2} of which carbon dioxide accounts for 1.82 W m^{-2}; i.e. this trace gas has a share of approximately 64 % in the amplification of the greenhouse effect (Stocker et al., 2013). Its recent growth rate amounts to slightly less than 0.3 W m^{-2} per decade. Since the onset of industrialisation in the mid-18th century until 2011, the anthropogenic emissions of carbon dioxide can be estimated as follows: fossil fuel combustion and cement production amount to 375 Gt C while land use change (mainly deforestation) accounts for 180 Gt C (Ciais et al., 2013). This corresponds with a rise in the global surface carbon dioxide concentration from 278 ppm in 1750 to 407 ppm at present (NOAA, 2018a; Stocker et al., 2013). Of this cumulative anthropogenic emission of 555 Gt C, roughly 43 % have accumulated in the atmosphere, around 28 % have been absorbed by the oceans and the remaining 29 % have been aggregated as organic matter in terrestrial ecosystems (Ciais et al., 2013; Rhein et al., 2013). Since carbon dioxide is chemically inert in the atmosphere, it remains until its removal through natural process such as photosynthetic uptake, oceanic dissolution and silicate weathering, which, in view of the human-emitted carbon dioxide, would take a few hundred thousand years (Ciais et al., 2013).

1.2. State of the Art

1.2.1. Climate change in the Arctic

Arctic ecosystems are well-adapted to the extreme environmental conditions and highly sensitive to a changing climate (McGuire et al., 2012; Oechel et al., 1997). Based on both observations during the recent past and future projections, global climate change has its greatest implications in the Arctic (Räisänen, 2001; Serreze et al., 2000). Given both the vast area and the massive potentially mobilisable quantities of stored carbon, the tundra biome is

of major interest within the context of climate change (McGuire et al., 2009; Tarnocai et al., 2009).

Changes in the past

The Arctic north of 60° N has warmed at a rate of 1.36 °C per century since 1875 (i.e. roughly twice as fast as the global average); moreover, since 1979, the Arctic land surface has warmed at an even higher rate of 0.5 °C per decade (Masson-Delmotte et al., 2013). This rapid warming was much more pronounced than the global average and due the effects of polar amplification (Figure 3).

The strongest warming occurs in autumn and early winter, which can be attributed to feedbacks associated with the seasonal reduction in sea ice extent and duration as well as the insulating effect of sea ice in winter (Masson-Delmotte et al., 2013). Permafrost temperatures have also risen in most regions since the early 1980s: warming up to 3 °C was observed in parts of northern Alaska between early 1980s and mid-2000s, and up to 2 °C were ascertained in parts of the Russian European North between 1971 and 2010 (Vaughan et al., 2013). This rise in temperature has led to a reduction in permafrost thickness and areal extent.

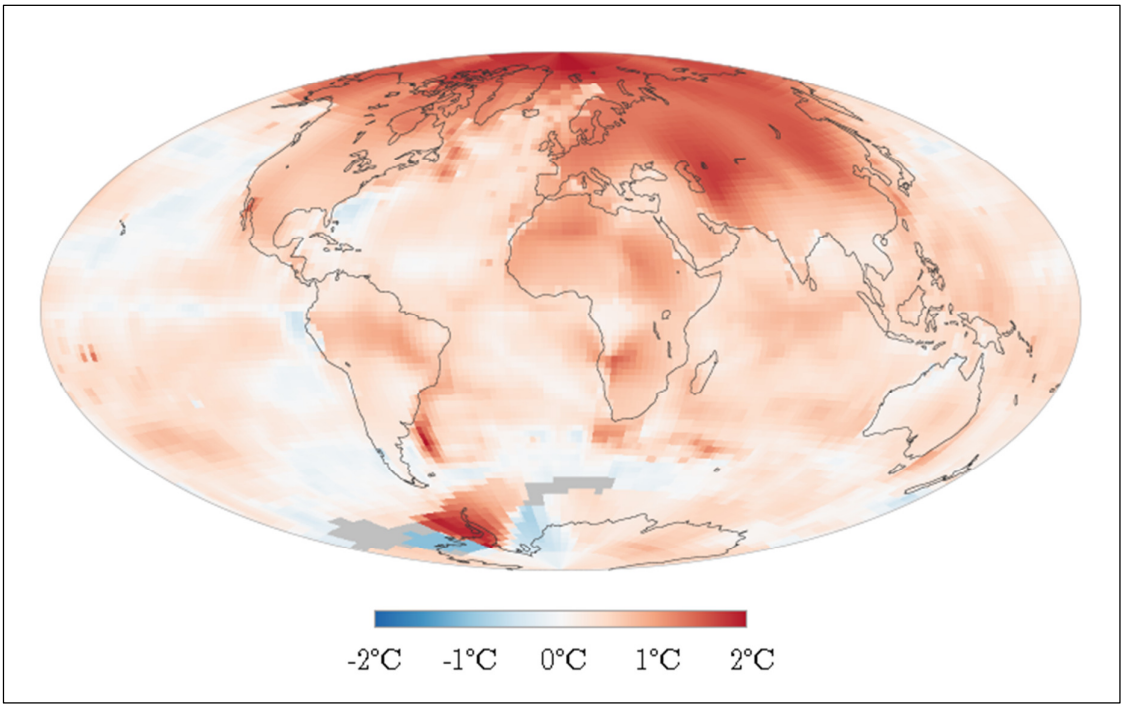

Figure 3 Global temperature anomalies for 2000-2009 relative to 1951-1980 illustrating the increased temperature rise in the Arctic due to polar amplification. During the observation period 2000-2009, the global temperature was approximately 0.9 °C higher than in the reference period 1951-1980, while the Arctic was roughly 2 °C warmer (NASA, 2013).

Based on multiple data sets, the averaged annual precipitation over land areas is estimated to have risen by about 3.4 mm yr^{-1} per decade in regions north of 60 °N between 1951 and 2008 (Hartmann et al., 2013). However, the positive trends in the individual data sets distinctly vary, and the certainty of the trends suffers from meagre data availability due to few high-latitude stations.

Projections for the future

The Arctic is anticipated to response more pronounced to climate change than the global average (Figure 4). The rapid warming trend will continue and is on average larger over land than over the ocean (Kirtman et al., 2013). Following the two representative concentration pathways RCP 2.6 and RCP 8.5, the mean surface air temperature in the Arctic will, respectively, rise by 2.2 °C and 8.3 °C until the projection period 2081-2100 relative to the reference period 1986-2005 (Collins et al., 2013). In the context of both RCP scenarios, the mean Arctic warming will then exceed the global average by roughly 2.2 times. As a consequence of both warming and changes in snow cover, which insulates the underlying soil, a substantial amount of near-surface permafrost (typically the upper 2 to 3 m) is facing degradation (Kirtman et al., 2013). By the end of the 21st century, between 37 % (RCP 2.6) and 81 % (RCP 8.5) of the near-surface permafrost area is projected to thaw (Collins et al., 2013). On account of a raised specific humidity in a warmer troposphere plus an enhanced transport of water vapour from the tropics, high-latitude land masses are likely to experience more precipitation. While a low increase by 0-20 % is projected under the RCP 2.6 scenario, the RCP 8.5 scenario is associated with a large increase in annual precipitation by 30-50 % between the periods 1986-2005 and 2081-2100 (Collins et al., 2013). The continuing warming also expedites the shrinking and thinning of the Arctic sea ice cover in great measure (Kirtman et al., 2013). The projections of average reductions in Arctic sea ice extent for 2081–2100 relative to 1986–2005 range from 43 % for RCP 2.6 to 94 % for RCP 8.5 in September (Collins et al., 2013). Under the RCP 8.5 scenario, a nearly ice-free Arctic Ocean in September before mid-century is likely. In summary, based on the robust evidence over multiple generations of models, there is very high confidence that the Arctic region will experience a considerable warming plus variably raised precipitation amounts.

Implications on the carbon cycle

The impact of the changing climate on the carbon turnover in high-latitude ecosystem is very complex on account of various interacting carbon flux drivers, whose prospective change is projected with varying confidences due to partly unidirectional and partly contrasting impacts, plus resulting feedbacks, which vary both in direction and magnitude.

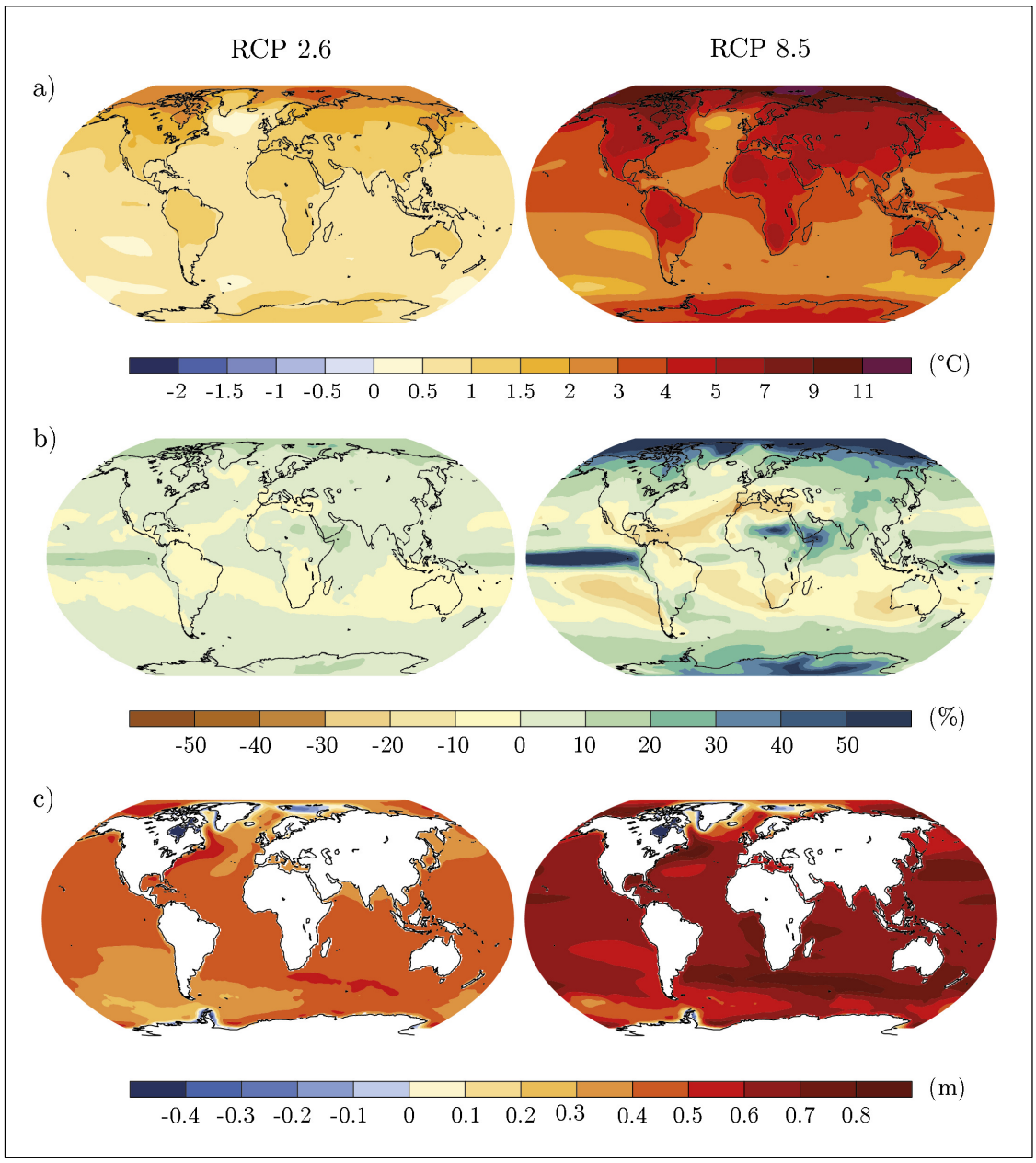

Figure 4 Ensemble modelled projections for the change in a) average surface temperature, b) average precipitation, and c) average sea level for 2081-2100 relative to 1986-2005 based on representative concentration pathways RCP 2.6 and RCP 8.5 (modified from IPCC, 2014). While the former scenario assumes prospectively mitigated greenhouse gas concentrations, which correspond with the goal to keep global warming likely below 2 °C above pre-industrial temperatures, the latter scenario expects very high concentrations as a result of sustained greenhouse gas emissions in the future. Following these projections, the Arctic will become a considerably warmer place with distinctly more precipitation and a variably risen/dropped sea level.

Permafrost thaw carries multiple ramifications such as active layer deepening, thermokarst activity, talik formation and coastal erosion (Schuur et al., 2008). These mechanisms may cause a substantial release of greenhouse gases by remobilising previously frozen soil organic matter (Oechel et al., 1993). The involved microbial decomposition is also prone to amplify by further rising soil temperatures (Davidson and Janssens, 2006). This temperature rise may be due to the downward transport of warmth from an increasingly heating surface, and it can be intensified by in situ heat production through metabolic activity (Heimann and Reichstein, 2008). At last, the growing emissions of methane and carbon dioxide are likely to lead to an enhanced rise in temperature forming a positive feedback, which even may accelerate (Koven et al., 2011).

Alternatively, rising temperatures also comprise the possibility of a negative feedback via an enhanced primary productivity. The underlying mechanisms include growing season prolongation, taller growth forms of the indigenous plant species, larger plants through the northern expansion of trees and shrubs and promoted plant growth through carbon dioxide fertilisation (Ciais et al., 2013; Hudson et al., 2011; Jia et al., 2009; Johnson et al., 2000; Pearson et al., 2013). A deeper active layer also enables deeper rooting depths and an elevated nutrient availability (Jorgenson et al., 2010; Salmon et al., 2016). Larger plants provide more shade, which mitigates permafrost thaw, but larger plants may also be accompanied by a lower albedo, which increases heat absorption (Loranty et al., 2011). Larger plants also accumulate more snow; the consequence being less soil freezing due to the decreased energy loss from the soil to the air, which is caused by the increased soil insulation (Zhang, 2005). The higher allocation of below-ground carbon as plant litter through both enhanced carbon fixation and deeper roots increases the soil organic carbon pool, but the grown availability of labile carbon may also increase decomposition rates (Kong et al., 2005; Kuzyakov, 2010). Another downside of a greater biomass in conjunction with higher temperatures is the risen likelihood of fires, which can release vast amounts of carbon and lead to further permafrost degradation (Allison and Treseder, 2011).

Both ground subsidence through permafrost thaw and the projected rise in precipitation facilitate the growth of wetland extent (in particular in continuous permafrost) with a hydrological setting, which is in favour of enhancing methane emissions (Christensen et al., 2004; Johnston et al., 2014; Jorgenson et al., 2006; Plug and West, 2009; Sachs et al., 2010). Besides the expansion of anaerobic soil layers, active layer thickening increasingly exposes potentially labile carbon to methanogens (Dorrepaal et al., 2009; Harden et al., 2012). The substrate availability can further be elevated by an augmented

photosynthesis increasingly allocating root exudates (Joabsson and Christensen, 2001). Its microbial decomposition under higher soil temperatures then proceeds in an accelerated manner. Besides terrestrial methane formation, substantial quantities of methane are stored within sub-marine hydrate deposits at continental margins and may be released by warming of the overlying waters (Ciais et al., 2013). Owing to its large global warming potential, rising methane emissions directly feed back to global warming.

Alternatively, the wetland area can also shrink (in particular in discontinuous permafrost) and, thus, reduce methane emissions by means of enhanced soil aeration (Merbold et al., 2009; Smith et al., 2005). The underlying processes involve the temperature-induced increase in evaporation as well as the decrease in soil moisture through deeper roots and geomorphological changes such as lake drainage (Godin et al., 2014; Koven et al., 2011). In addition to an altering environmental setting, non-saturated soils in high-latitudes ecosystems can absorb atmospheric methane (Jørgensen et al., 2015). Water-saturated sites may also display some methane uptake, when exposed to light; this process occurs through the link between microbial methane oxidation and moss-associated photosynthesis (Liebner et al., 2011).

Projected carbon release and associated problems

While there is high confidence that the permafrost extent will decline in response to climate change, there is medium confidence on its magnitude. Compared to 1986-2005, near-surface permafrost area (continuous and discontinuous) is anticipated to decline by between 37 % (RCP 2.6) and 81 % (RCP 8.5) until 2080-2099 (Collins et al., 2013). The amplitude of this projected reduction does not only depend on the emission scenario, but also very much on both the consideration and the accurate representation of permafrost-related soil processes in current models. Not least this uncertainty causes even low confidence on the projected magnitude of the mobilisation of currently frozen carbon through greenhouse gas emissions. Combining observed soil carbon profiles and modelled thaw rates yielded estimates of newly thawed carbon by 2100: 246 Gt for RCP 4.5 and 436 Gt for RCP 8.5 (Harden et al., 2012). Under RCP 8.5 warming, the resulting emission of both methane and carbon dioxide to the atmosphere is estimated to range between 50 and 250 Gt C between 2000 and 2100 (Ciais et al., 2013). It is also unclear, whether the permafrost areas maintain their long-term sink function or convert into a carbon source: some models indicate that the enhanced carbon uptake through plants offsets the rising carbon release for several decades, but the microbial release overwhelms the uptake capacity over longer

time scales with continued warming (Schuur et al., 2015). In general, the future trajectory of annual net carbon fluxes in response to climate change remains uncertain due to both ambiguous results and large confidence intervals (Heimann and Reichstein, 2008).

Going into detail, this uncertainty arises not only from limited knowledge on the physical thawing rates, the fraction of released carbon after thawing and the time scales of release, but also both the typical surface heterogeneity of terrestrial Arctic ecosystems and the general flux data shortage from these environments aggravate the estimation of robust carbon budgets (Ciais et al., 2013). The scarce data availability particularly applies to the extensive Russian tundra, which covers around 3 million km^2, i.e. more than half of northern high-latitude tundra ecosystems (Chapin III et al., 2005; Sachs et al., 2010). The low density of flux observation sites is due to both challenging logistics in these remote and sparsely inhabited areas without line power as well as the harsh environmental conditions (McGuire et al., 2012). Providing both carbon budgets from the Siberian tundra as well as a better understanding of the effects of surface heterogeneity on these budgets is essential concerning the potentially tremendous carbon loss from thawing permafrost, which can impact the global climate for centuries.

1.2.2. Surface heterogeneity in tundra ecosystems

The Arctic tundra was estimated to have acted as a source for methane of 19 ± 10.5 Tg C yr^{-1} and as a sink for carbon dioxide of 110 ± 186 Tg C yr^{-1} during the period 1990-2009 (McGuire et al., 2012). A great deal of these large uncertainties can be ascribed to the small number of observations in comparison to the vast area considered. Aggravating this research gap, carbon fluxes in tundra ecosystems are very variable in both time and space.

Spatial variability in carbon fluxes

Arctic landscapes are characterised by extreme vegetation patchiness, often with sharply defined boundaries between largely differing vegetation classes (Shaver et al., 2007). On the pan-Arctic scale, the largest differences occur along the latitudinal gradient from Low Arctic to High Arctic ecosystems, while the sparsely vegetated Arctic deserts in the far north exhibit typical mosaics of plant functional groups to a lesser extent (Gould et al., 2003). In this way, Arctic ecosystems vary by three orders of magnitude in productivity (Callaghan et al., 2005). However, moving to smaller scales, differences in vegetation distribution nearly as large also occur along local and regional gradients of topography, snow cover and exposure to sun and wind (Shaver et al., 1996a, 1996b).

Besides carbon dioxide, methane is also emitted in a frequently uneven distribution as a result of varying environmental characteristics such as topography, hydrology, plant cover and soil physics/chemistry (Heikkinen et al., 2004; Marushchak et al., 2016; McGuire et al., 2012). While there are elevated, well-aerated patches displaying zero methane emissions, there also hotspots, e.g. along thawing lake margins releasing large volumes through ebullition (Walter et al., 2006). An illustrative example for clarifying the varying factors that govern carbon flux dynamics is the polygonal tundra, which both is typical for the extensive areas of the circumpolar lowland tundras and forms a mosaic of substantially differing microsites (Kutzbach, 2005). In this ecosystem, considerable variation in methane fluxes has been observed even over distances of just a few meters (Kutzbach et al., 2004). However, when shifting from the microscale (10^{-2}-10^{2} m^2) up to the mesoscale (10^{4}-10^{6} m^2), the spatial heterogeneity homogenises due to the regular alternation of polygon rims and centres. Therefore, the extent of surface heterogeneity depends on the aimed scale, which in turn requires correspondingly appropriate measurement techniques to capture the carbon fluxes of interest.

Temporal variability in carbon fluxes

Apart from the spatial variability of carbon fluxes, their temporal variability is also pronounced throughout the year (Kwon et al., 2006). While the carbon dioxide fluxes typically oscillate on the diurnal scale, a daily cycle is mostly absent for methane fluxes apart from few studies reporting such behaviour during certain periods of the year (Gazovic et al., 2010; Long et al., 2010).

Both exchange fluxes are subject to seasonal trends, which are determined by (i) meteorological conditions such as cloudiness, precipitation, pronounced changes in air temperature, and by (ii) sub-surface conditions such as soil temperature, thaw depth, water table position, and by (iii) biotic conditions such plant phenology, microbial abundance, composition and activity (Kutzbach et al., 2007b; Long et al., 2010).

The bulk of the annual carbon dynamics occurs during the growing season, when plants sequester atmospheric carbon and microorganisms produce carbonaceous trace gases, while winter activity has been anticipated negligible due extremely low temperatures. However, evidence is accumulating that emissions in winter may account for a considerable fraction of the annual carbon balance (van der Molen et al., 2007). Three examples of increasingly available studies on non-growing season fluxes: (i) early winter methane emission bursts, whose integral is roughly equal to the sum of methane emissions in summer (Mastepanov et al., 2008); (ii) sustained methane effluxes during

the entire cold season while the major fraction was released during the zero curtain period, when soil temperatures are poised near 0 °C (Zona et al., 2016); (iii) large spring emission pulses of methane and carbon dioxide prior to snowmelt (Raz-Yaseef et al., 2017). Accordingly, year-round measurements are essential for reliable annual budgets (Kittler et al., 2017).

The interannual variability of carbon flux balances largely originates from variations in snow melt timing and air temperature expressed as growing degree days (Aurela et al., 2004; Groendahl et al., 2007). These determinants define the growing season length, which is particularly critical to the sink/source strength of a tundra ecosystem (van der Molen et al., 2007). The pattern that a longer growing season corresponds to a greater net carbon uptake, which has been demonstrated at multiple Arctic sites, is, however, not uniform around the Arctic (Gamon et al., 2013; Parmentier et al., 2011a). Furthermore, depending on the environmental setting, wildfire occurrence might also be an important factor (McGuire et al., 2009). Hydrometeorological conditions such as the frequency and intensity of rain events are relevant for the year-to-year variation in methane fluxes, but these variables play a rather tangential role for carbon dioxide fluxes (Aurela et al., 2004; Whalen and Reeburgh, 1992). Findings in some studies indicate that the interannual fluctuations are mostly greater for both photosynthesis and methane efflux and smaller for respiration (McGuire et al., 2009; van der Molen et al., 2007; Parmentier et al., 2011a).

1.2.3. Estimating robust carbon budgets

The pronounced spatiotemporal variability of carbon fluxes in Arctic landscapes distinctly complicates the estimation of robust carbon budgets that are accurate and precise (Shaver et al., 2007). The development of eligible approaches to address this problem requires more research. Facing this challenge is important, not least in a broader micrometeorological context as footprints are often not entirely homogeneous and methodologies, which are applied in the Arctic tundra, could also be adopted in other ecosystems.

Necessity and approach

Robust budgets of various Arctic ecosystems form an important foundation for estimating regional budgets, which in turn support gauging pan-Arctic carbon dynamics through large-scale modelling. An improved balancing of the Arctic carbon exchange can be achieved by a better characterisation of the spatial variability in carbon fluxes and associated environmental controls, e.g. the influence of vegetation composition and structure (Kade et al., 2012; Kwon et al., 2006). Enhanced present-day budgets also support the estimation of future budgets, which is particularly critical against the background

of a changing climate. On account of the surface heterogeneity in tundra ecosystems, the effects of climate change will vary strongly according to the land cover type, and the probable changes in their areal extent will further impact on regional carbon budgets (Marushchak et al., 2013).

The estimation of regional budgets is generally based on the upscaling of carbon fluxes by means of spatial information in the form of remote sensing scenes. These scenes are frequently utilised for a land cover classification to determine the areal extent of predefined surface types, which are assumed to constitute relatively uniform flux dynamics (Marushchak et al., 2013). Remote sensing products that contain multiple bands can also form the basis for creating maps of vegetation-specific parameters such as the normalised difference vegetation index or the leaf area index (Belshe et al., 2012; Shaver et al., 2007). Based on ascertained relationships between carbon fluxes on one side and surface types or vegetation indices on the other side, the budget of the examined area is then calculated as the area-weighted sum of the cumulative fluxes obtained for every surface type or by weighting the cumulative fluxes according to a specific vegetation index (Fox et al., 2008).

Available methods

As a prerequisite for estimating robust budgets with this procedure, fine-scale information on fluxes are necessary. Due to the typical surface heterogeneity in tundra landscapes, chamber measurements are normally employed to differentiate the carbon exchange of individual microforms with the atmosphere (McGuire et al., 2012). This method captures the microscale variability in fluxes very well. However, there are several generally associated downsides: a possible bias through the subjectivity of chamber location, a potential disturbance to the studied system, a low spatial representativeness not least due to a great workload, a usually lacking temporal resolution due to a confinement to discrete sampling, a probable inaccuracy due to the decoupling from atmospheric parameters that may govern the carbon exchange (Fox et al., 2008; Kade et al., 2012; Kutzbach et al., 2007a; Sachs et al., 2008).

Alternatively, the eddy covariance method as a non-intrusive, continuous and high-frequency measurement technique that operates on the mesoscale, yields turbulent fluxes, which integrate across multiple microforms (Aubinet et al., 2012; Foken, 2008). The size and location of the sampled surface (upwind from the setup) constantly shifts according to, among other factors, wind direction, wind speed, atmospheric stability, crosswind and surface roughness (Detto et al., 2006). In this dynamic process, the temporal variability in the observed fluxes is not only a result of the varying uptake/release rates of the individual microforms, but

also a consequence of the varying fractions of the microforms in the sampled surface due to the spatial variability. After a period of time with changing wind field conditions, a certain area around the flux tower has been sampled defining the footprint, i.e. the source area, which contributes to the observed fluxes. In a homogeneous terrain with uniform fluxes, the resulting budgets of the source area are representative for the area of interest, i.e. the surrounding ecosystem whose carbon sink/source strength is under examination. In presence of a heterogeneous landscape, however, the footprint budgets lack representativeness, if the footprint is not representative of the mean microform distribution in the area of interest (Figure 5). In such an environment, budgets strongly depend on tower location, measurement height and wind field conditions, i.e. the budgets are likely to exhibit a sensor location bias (Schmid and Lloyd, 1999). Consequently, a representative

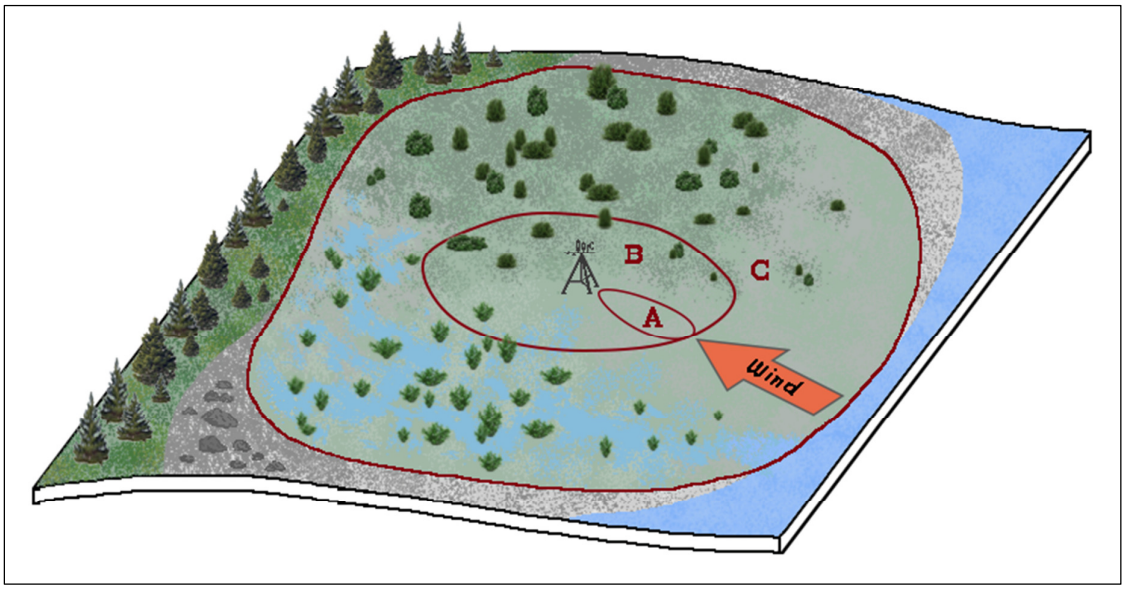

Figure 5 Schematic visualisation of the sensor location bias in an ecosystem that is composed of various units, which in turn may also exhibit a heterogeneous surface. At a given time, the flux tower samples a surface (A), whose size and location constantly shifts according to wind direction, wind speed, atmospheric stability, cross-wind and surface roughness. This surface, however, is potentially not representative of the entire source area around the flux tower (B). The budgets estimated for this footprint depend on tower location, measurement height and wind field conditions. Consequently, these budgets are likely not to represent the budget of the area of interest (C). The deviation between the respective budgets of source area and area of interest is characterised by the sensor location bias and needs to be considered for the upscaling of footprint budgets.

budget requires measurements in a footprint where the distribution of surface elements is the same as in the area of interest for all wind sectors (Leclerc and Foken, 2014). A heterogeneous surface, however, may also provide the opportunity to conduct a concurrent sampling of multiple microforms and the study of their carbon fluxes utilising only one eddy covariance instrumentation (Forbrich et al., 2011; Morin et al., 2017). This requires the partitioning of the integrated flux into its microform-specific fluxes. A successful flux decomposition routine yields microform-specific budgets that in conjunction with a precise determination of the microforms' spatial coverages in the area of interest enable the estimation of robust budgets for a heterogeneous surface.

Bridging the scales

The differing scales of the two measurement techniques have been repeatedly bridged in Arctic ecosystems, when chamber measurement-derived carbon budgets have been upscaled and partly successfully reconciled with budgets obtained with the eddy covariance method (Budishchev et al., 2014; Christensen et al., 2000; Eckhardt, 2017; Heikkinen et al., 2002; Oechel et al., 1998; Stoy et al., 2013; Zamolodchikov et al., 2003; Zhang et al., 2012). Reasons for a lacking coincidence of both budgets included general scaling problems such as scale-dependent flux dynamics and flux drivers, the incapability of the underlying surface classification to resolve small-scale heterogeneities as well as a mismatch of the sampled areas between both methods (i.e. chamber measurements are unrepresentative for the mosaic of land cover classes in the eddy covariance footprint), and not least the general drawbacks of chamber measurements (Fox et al., 2008; Sachs et al., 2010).

On the other hand, the eddy covariance technique has well-known limitations through the (greatest possible) fulfilment of the underlying theoretical assumptions: steady-state conditions, a well-developed turbulence as well as a horizontal and uniform terrain are the major assumptions that derive from a set of simplifications of the mathematical algorithm (Aubinet et al., 2012). Another important factor in this regard is the uncertainty of the footprint model, which identifies the source area of the observed fluxes (Leclerc and Foken, 2014). Periods, where these simplifications are not justified, can be detected with a quality control routine, and the consequently missing data can be substituted with a gap filling procedure (Foken, 2008). This procedure is also important for periods with data gaps due to severe meteorological conditions (heavy rain, lightning), blackouts, animal browsing and so forth. In summary, the eddy covariance technique is the reliable method on the mesoscale with the potential to resolve carbon flux dynamics on the microscale, and this downscaling has not yet been done for Arctic ecosystems.

1.3. Objectives

The major purpose of this work is to provide robust carbon budgets from a Siberian tundra ecosystem that has not yet been investigated. This ecosystem, the flood plain on Samoylov Island in the Lena River Delta, constitutes a landscape with a heterogeneous surface, which requires a careful consideration in the process of budget estimation. Accomplishing this aim is intended by achieving several sub-goals:

- Parsing the spatiotemporal variability of methane and carbon dioxide fluxes utilising the eddy covariance technique and footprint modelling.
- Elucidating the heterogeneity of the footprint and its impact on the flux dynamics.
- Linking the fluxes to flux drivers based on different modelling approaches.
- Estimating flux budgets that take the ecosystem's heterogeneity into account.

Attaining these objectives yields a method that may constitute a suitable approach for estimating robust carbon budgets at other Arctic sites. Moreover, this work aims at contributing to an improved understanding of biogeochemical processes between atmosphere and tundra vegetation, which may support the assessment of the effects of climate change on tundra ecosystems.

2. Material and Methodology

2.1. Site description

Situated within the zone of continuous permafrost on the fringe of the Laptev Sea in northern Siberia, the Lena River Delta is one of the largest deltas in the world (Figure 6a). It covers an area of about 32,000 km^2 and is formed by three major geomorphic terrace-like units (Grigoriev, 1993; Schwamborn et al., 2002). While the 2^{nd} and 3^{rd} terraces are mainly of pre-Holocene age, the 1^{st} terrace is of Holocene origin and is the largest terrace in terms of spatial extent and carbon stock (Figure 6b). The 1^{st} terrace also comprises the majority of the roughly 1,500 islands in the Lena River Delta. One of them, Samoylov Island (72°22' N, 126°28' E) has been hosting researchers in various scientific fields including micrometeorology, catchment hydrology, geomorphology, geophysics, microbiology, hydrobiology, soil science and many more since the late 1980s (Hubberten et al., 2006). It is located south of the central part of the delta, extends across an area of 4.8 km^2 and forms the investigation site of this study.

Samoylov Island consists of two geomorphological units: the late-Holocene river terrace in the eastern part and the active flood plain in the western part of the island where the flux tower was installed (Figure 6c). The river terrace spans approximately 2.8 km^2 and is characterised by ice-wedge polygonal tundra. This type of tundra encompasses a regular pattern of polygon centres and polygon rims whose methane emissions have been extensively studied (Kutzbach et al., 2004; Sachs et al., 2008; Wille et al., 2008).

In contrast to the polygonal tundra on the delta's river terraces, the flood plains have to date received scarce attention in terms of greenhouse gas fluxes although flood plains represent 40 % of the land area of the delta, with a mean soil carbon stock in the upper 1 m of 14 ± 7 kg m^{-2} (Zubrzycki et al., 2013). The flood plain on Samoylov Island stretches over an area of around 1-2 km^2 depending on the water level. During autumn, when water level of the Lena River is at its lowest, the area of the flood plain can double in size with an extensive sand area along the waterfront. Snowmelt triggers an an-

nual spring flood, which usually occurs within the first two weeks of June; this month contributes on average around 36 % to the total annual discharge and almost half of the annual suspended sediment (Fedorova et al., 2015; Yang, 2002). In the course of this event, massive ice floes often obstruct river flow in the maze of channels leading to a complex flow behaviour, which may cause a further rise in water table and reversed flow directions. During the

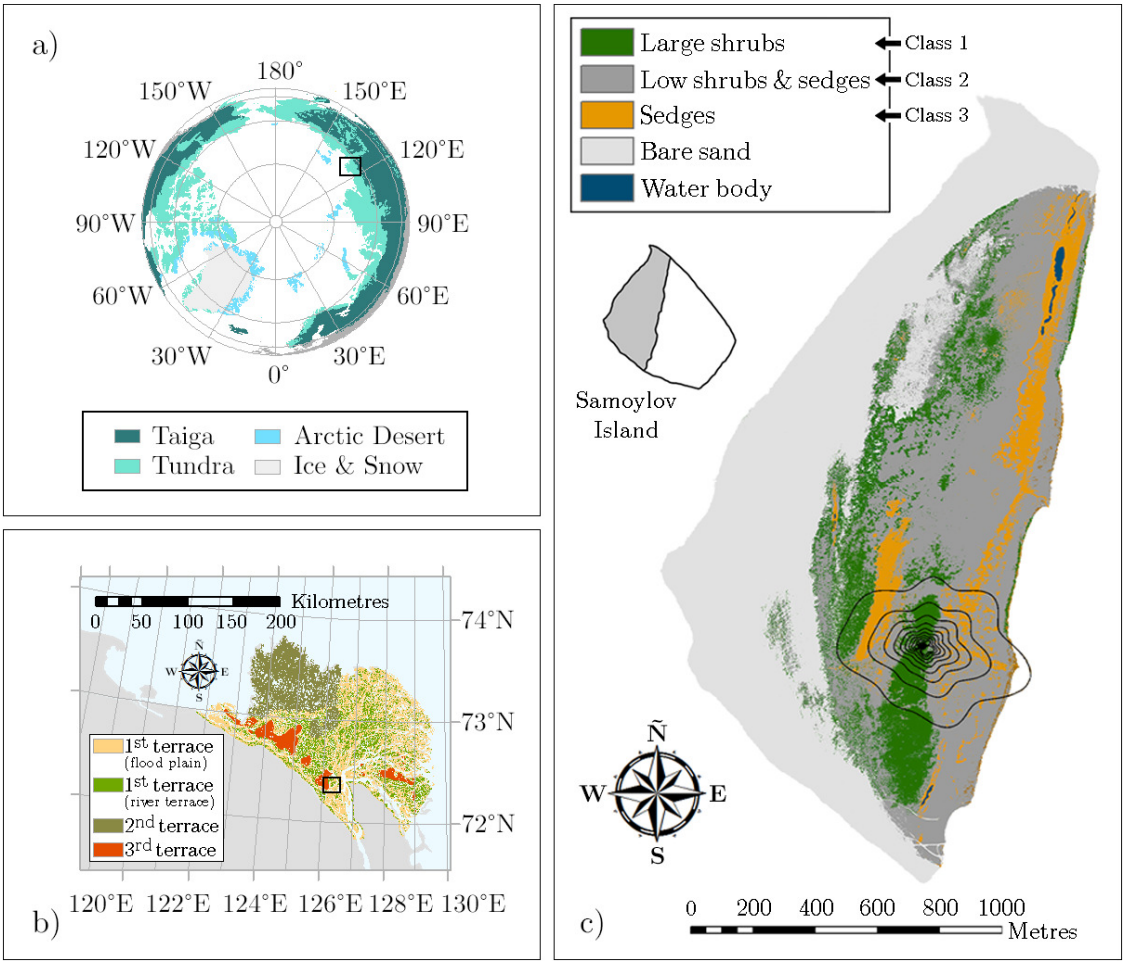

Figure 6 Geographical setting of the measurement site: a) location of Lena River Delta within high-latitude biomes (Fisher, 2016), b) position of Samoylov Island in the Lena River Delta, which is characterised by three geomorphic terrace-like units (Morgenstern et al., 2011; Zubrzycki et al., 2013), and c) vegetation map of flood plain on Samoylov Island. The flux tower was situated in the centre of the footprint isolines, which indicate the averaged area from which 10 - 90 % of the flux originated (increment of 10%) during both measurement periods 2014 and 2015 (footprint climatology). The small inset illustrates Samoylov Island being composed of flood plain (grey) and river terrace (white).

exceptional spring flood in 2014 the entire flood plain and lower parts of the river terrace were submerged for several days, whereas the 2015 spring flood was of minor magnitude in comparison, inundating roughly 80 % of the flood plain for only a few hours.

The climate is Arctic continental, which is characterised by very low temperatures and a low annual precipitation. For the remote town of Tiksi, situated 120 km to the south-east of Samoylov Island, a mean temperature and annual precipitation of -12.8 °C and 321 mm were respectively measured during the period 1981-2010 (Pogoda i Klimat, 2016). The weather during spring, summer and autumn is strongly dependent on the wind direction as the Lena River Delta is located at the interface between the Arctic Ocean and the continental land mass of Siberia. Northern winds tend to be associated with cold, moist air, whereas southern winds transport warm, dry air. The winter temperatures drop below -40 °C multiple times during polar night, which lasts from 15th November to 28th January. Snowmelt usually starts in late May, and air temperatures exceeding 0 °C usually dominate from early June onwards. The short growing season commences in late June and ceases in early September overlapping with polar day, which lasts from 7th May to 8th August. Refreezing occurs, when sub-zero temperatures begin to prevail again in late September.

2.2. Instrumental setup and data recording

An eddy covariance system was set up in the southern part of the flood plain of Samoylov Island to determine turbulent fluxes of momentum, sensible heat, latent heat, carbon dioxide and methane. Measurements, from which fluxes are utilised in this study, ran from 18th June to 2nd October 2014 (107 days) and from 9th June to 24th September 2015 (108 days). Winter measurements following both measurement periods were also conducted. However, the calculated flux time series were too fragmented for determining reliable flux budgets, which was mainly due to the harsh, Arctic conditions during the cold season. Further data gaps were caused by logger failures during both polar nights as well as the spring flood in early June, when the system was dismantled.

The flux tower was equipped with a sonic anemometer (CSAT3, Campbell Scientific, UK) measuring three wind components and sonic temperature with a frequency of 20 Hz installed at a height of 2.83 m. Open-path infrared gas analysers were mounted next to the anemometer measuring concentrations of H_2O and CO_2 (LI-7500A, LI-COR Biosciences, USA) as well as CH_4 (LI-7700, LI-COR Biosciences, USA). The records of these instruments were stored on a logger (LI-7550, LI-COR Biosciences, USA). In addition to this instrumental setup, another eddy co-

variance system with the same instrumentation has been installed at a central position on the adjacent river terrace (Wille et al., 2008).

Supplementary meteorological measurements on the flood plain were carried out to acquire quarter-hourly data on air temperature and humidity (HMP45, Campbell Scientific, UK), four components of radiation (NR01, Campbell Scientific, UK), photosynthetic photon flux density (SKP215, Skye Instruments, UK), snow depth (SR50A, Campbell Scientific, UK), precipitation (YTB52202, Young, USA) and soil temperatures (TH3, UMS, Germany), which were respectively gauged about 10 m north and 10 east of the flux tower at depths of 5, 10, 20, 30, 50, 100 cm. All supplementary data was recorded on a logger (CR1000, Campbell Scientific, UK) and stored for 15-min intervals. Furthermore, the water table depth was monitored with pressure probes (Mini-Diver, Schlumberger, Netherlands) in 11 wells evenly spread around the flux tower. Lastly, a camera (TLC200, Brinno, Taiwan) was mounted on the flux tower pointing towards north-east for monitoring the phenology in the footprint by taking pictures every 15 minutes during spring 2014.

2.3. Flux processing

Flux computation was conducted applying the software EddyPro version 6.0.0 (LI-COR Biosciences, 2016) for 30-min intervals. The initial raw data processing included the following procedures: (i) spike removal to detect and substitute short-term outranged data points, (ii) double rotation of coordinate system by rotating the raw wind components into the mean horizontal wind field in order to reduce the means of both lateral and vertical wind to zero, (iii) block averaging to obtain a mean for extracting turbulent fluctuations, (iv) automatic time lag optimisation by shifting time series to compensate for instrumental separation.

The subsequent correction scheme comprised the following proceedings: (v) WPL correction to account for density fluctuations due to thermal expansion and water vapour dilution of the air (Webb et al., 1980), (vi) spectral correction in the low frequency range due to a finite averaging interval (Moncrieff et al., 2004), and (vii) spectral corrections in the high frequency range due to the imperfection of the sensors and sensor separation (Horst and Lenschow, 2009; Ibrom et al., 2007). As a last step, the sampling errors of the calculated fluxes were estimated (Finkelstein and Sims, 2001).

The calculated fluxes underwent a comprehensive quality assessment routine to ensure that fluxes utilised for modelling complied with eddy covariance theory. This included (viii) the identification of flux intervals with non-steady-state conditions by means of the stationarity test (Foken and Wichura, 1996), (ix) the application of

the integral turbulence characteristics test to detect flux intervals where a well-developed turbulence was absent (Foken and Wichura, 1996). For the further recognition of a deficiently-developed turbulence as well as instrument malfunction, (x) the skewness and kurtosis of flux-specific scalars were examined (Tennekes and Lumley, 1972). Flux intervals were discarded where the skewness was either less than -2 or greater than 2, and/or kurtosis was greater than 8. Subsequently, (xi) methane and carbon dioxide flux intervals were removed, if the corresponding sensible and latent heat fluxes have failed the preceding quality assurance; this ensures that solely high-quality data was utilised in the WPL correction. Further filtering involved (xii) the extraction of methane and carbon dioxide fluxes, when the signal strengths of the gas analysers, i.e. the available optical power in their laser paths, were below 30 % and 60 %, respectively. Finally, (xiii) percentiles for the entire set of methane and carbon dioxide fluxes were respectively computed, and fluxes below the 1^{st} percentile and above the 99^{th} percentile were excluded. After executing the entire quality assessment routine, roughly 47 % of methane flux values and about 41 % of the carbon dioxide flux records were discarded (Figure 7). Only the remaining high-quality fluxes were utilised during the flux modelling. Furthermore, the determined carbon dioxide fluxes captured the growing season in both years as well as the observed methane fluxes in 2015, whereas the methane fluxes in 2014 began to be of noteworthy magnitude prior to the measurements.

Information on the source area of the fluxes were gathered with the aid of an analytical footprint model for non-neutral stratification (Kormann and Meixner, 2001). This model is based on the solution of the two-dimensional advection-diffusion equation for power law profiles of both mean wind velocity and eddy diffusivity (Leclerc and Foken, 2014). Depending on wind direction, wind field properties, atmospheric stability and roughness length, a source weight function was computed for each flux interval.

2.4. Surface structure

In addition to standard meteorological parameters, surface characteristics around the flux tower were also examined to account for the footprint's distinctive heterogeneity. This included surveys of topography, active layer depth, near-surface soil moisture, moss properties and vegetation around the flux tower conducted in early September 2015 (Figure 8). The topography was measured applying real time kinematic-based GPS navigation. Around the flux tower, the topography exhibited a slightly undulating relief ranging from 7.8 m to 10.7 m above sea level. This relief exerted a fundamental influence on the distribution of active layer

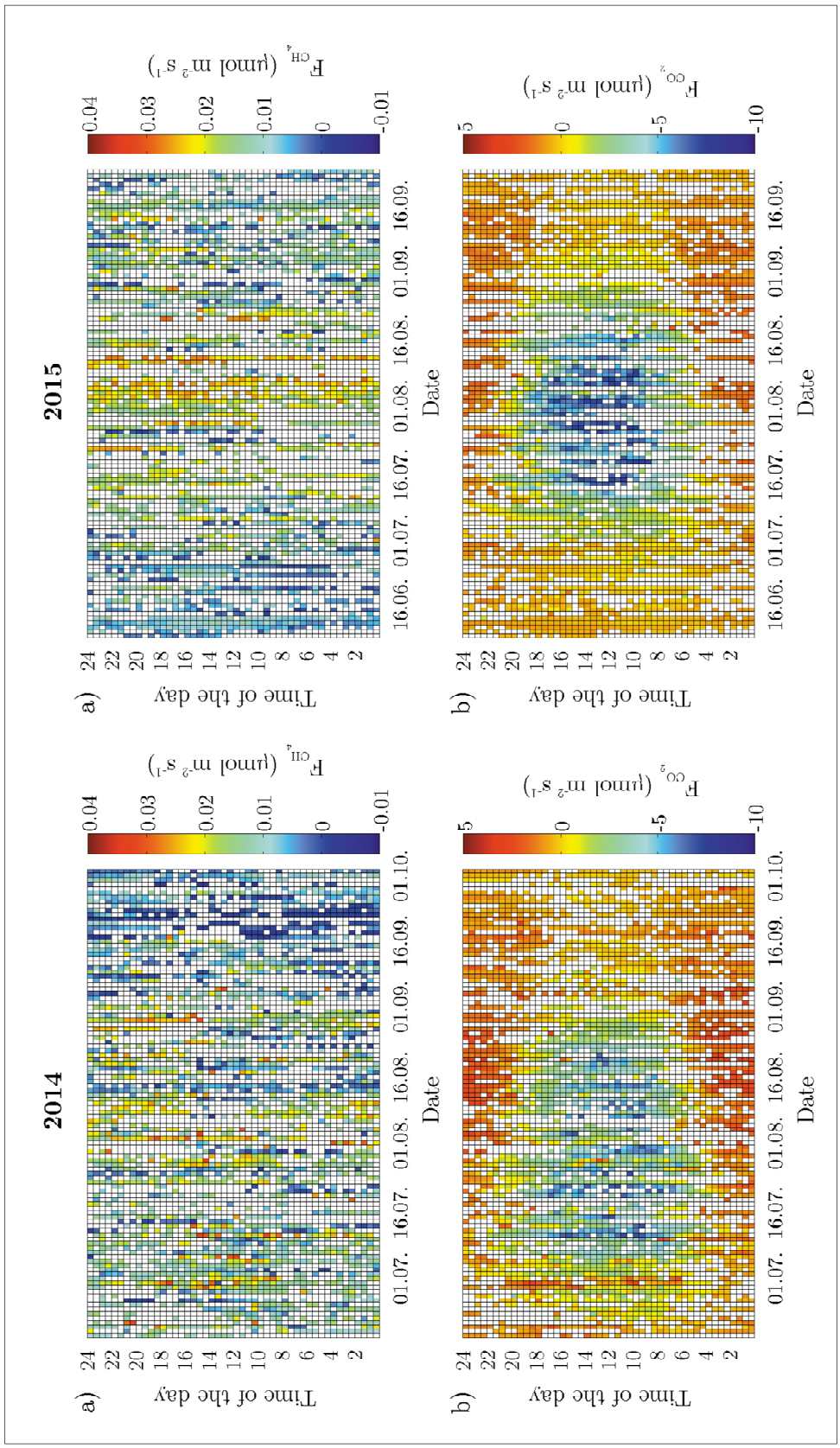

Figure 7 Fingerprints of observed carbon fluxes during the measurements periods 2014 and 2015 after conducting the quality assessment routine: a) methane flux, and b) carbon dioxide flux. It is evident that the measurement periods encompass the growing season. The white cells denote missing values, which results from either discarded flux records or original data gaps.

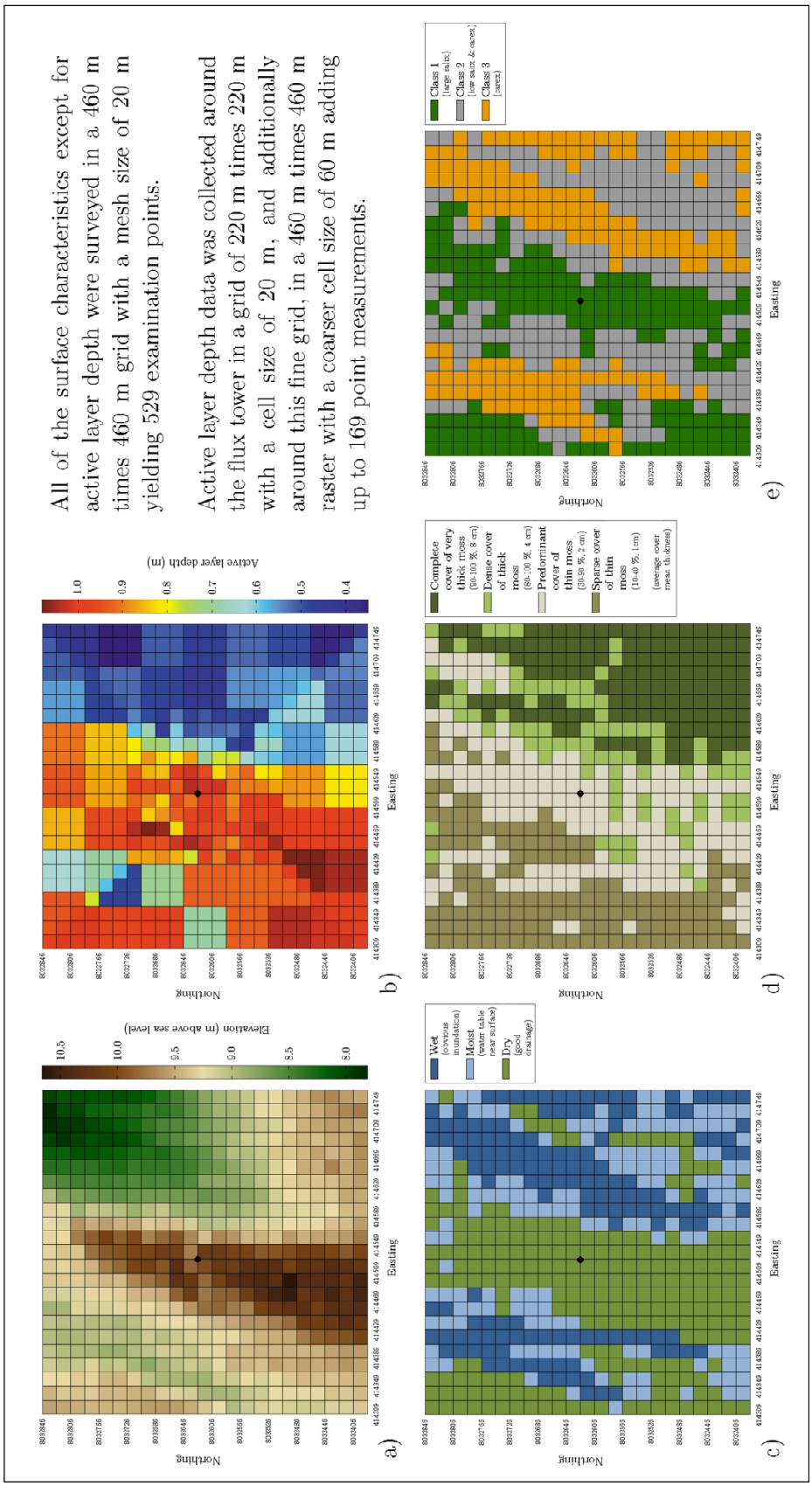

Figure 8 Footprint characteristics manually mapped around the flux tower (black dot): a) topography, b) active layer depth, c) near-surface moisture, d) moss properties, and e) vegetation. The topography as a fundamentally underlying factor outlined elevated and depressed patches and, thus, either drained or steeped patches, respectively. The moisture conditions then directly impacted on the distribution of active layer depth, moss properties and vegetation.

depth, near-surface moisture and moss properties. The active layer depth was determined in autumn, when the thaw depth was at its largest thickness by pushing a metal rod into the ground until reaching the permafrost table (interface between active layer and permafrost). The parameters near-surface moisture and moss properties were classified based on site-specific categories.

Classification of the vegetation in the footprint

All of these potential flux drivers were well coupled to each other. In addition, their distributions coincided well with the distribution of the indicative vegetation, which was categorised utilising three classes (Figure 9):

Vegetation class 1 ("large salix") refers to sites, which were densely vegetated by dwarf shrubs of the willow family such as S*alix pulchra*, *Salix lanata, Salix hastata*, *Salix glauca*, growing to a maximum height of around 1 m. This shrubby vegetation was located on an elevated sandy ridge aligned in the north-south-axis. Since the ground water table remained at depths between 30 cm and 70 cm, the surface was mostly dry, forming favourable growing conditions for willow shrubs and a sparse cover of thin moss. The active layer depth was large displaying depths in the range of 0.8 m to 1 m with a maximum depth of 1.08 m.

Vegetation class 3 ("carex") describes areas dominated by sedges including *Carex aquatilis*, *Carex chordorrhiza*,

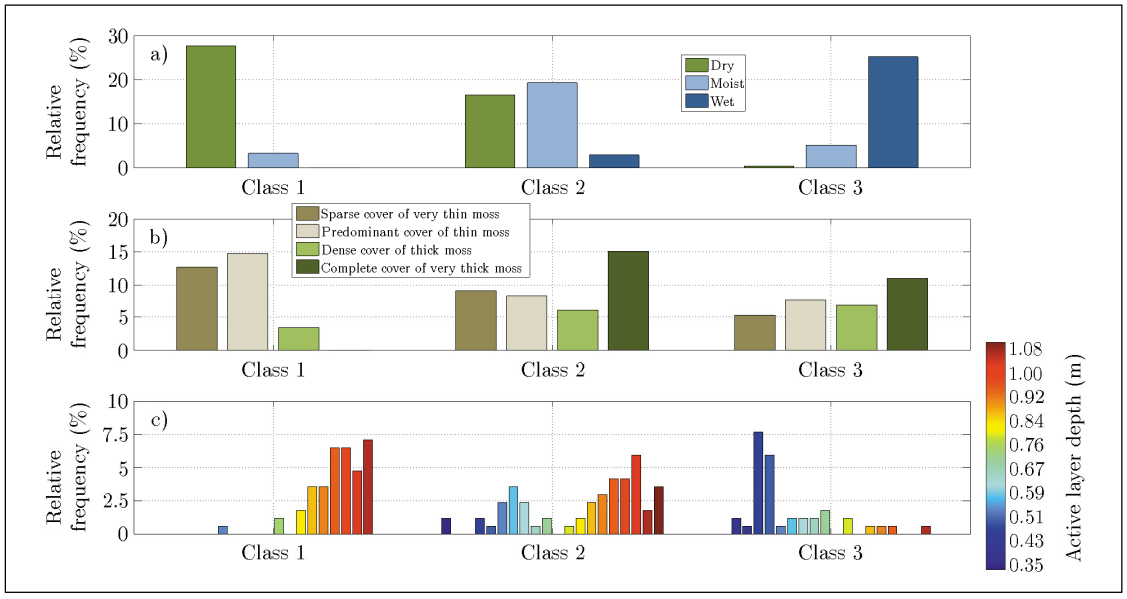

Figure 9 Distribution of potential flux drivers within three vegetation classes: a) near-surface soil, b) moss properties: cover and thickness; both properties scale well with each other, and c) active layer depth. In summary, the vegetation served as a reliable proxy for potential soil-related flux drivers.

Carex concolor as well as species of *Eriophorum* and *Equisetum*. This graminoid vegetation was located in the north-western and eastern depressions. The former was a large trench with standing water while the latter was a backswamp with wet patches of varying size, which were constantly fed by a draining lake on the river terrace. The water depths were in the range between 5 cm and 40 cm, and displayed minimal fluctuations apart from a few heavy precipitation events, which triggered sudden rises by a few centimetres. Following topographical gradients, the accumulating water attracted sedges and mosses, both preferring an ample moisture supply. Hence, patches with a complete cover of thick moss were abundant. When the water depth reached 30 cm or more, however, moss cover and thickness were rather minor. This particularly applies to the trench and the northern part of the backswamp where the water reached depths of half a metre. The active layer depth was low, typically ranging from 0.4 m to 0.7 m with a minimal depth of 0.35 m.

Vegetation class 2 ("low salix & carex") constitutes an intermediate class consisting of species typical for both previous classes with willows growing to a height of about 0.3 m. This mixed vegetation occurred in the moist transition zones between the dry elevated ridge and the water-logged depressions. Mosses of all cover and thickness classes were to be found, and the active layer depth varied widely.

Classification of the vegetation on the flood plain

In addition to the manual vegetation classification around the flux tower, another classification of the vegetation on the entire flood plain was conducted (Figure 6c). This procedure was based on a supervised classification routine of a geo-referenced orthomosaic, which was created employing visible aerial imagery from a helicopter circling around Samoylov Island in August 2014 (Figure 10). The resolution of the orthomosaic amounts to 8.5 cm, and hence provides a high spatial information density, sufficient to represent the high spatial heterogeneity of the surface. The set of three vegetation classes, utilised in the manual classification, was adopted in combination with two additional classes, which do not occur within the 90 % contribution footprint. These two classes denote the large area of bare sand along the waterfront and some small water bodies mainly situated in the northern part of the flood plain. The classification routine was based on maximum likelihood classification tools that assign each cell of the orthomosaic to one of the five predefined classes. The classes were characterised by their spectral signature, and the decision, which class a cell was allocated to, was dependent on its probability to match one of these signatures. The uncertainty associated with the supervised classification was determined by comparing it against the manual classification. This included the adaption of the coarse resolution of the

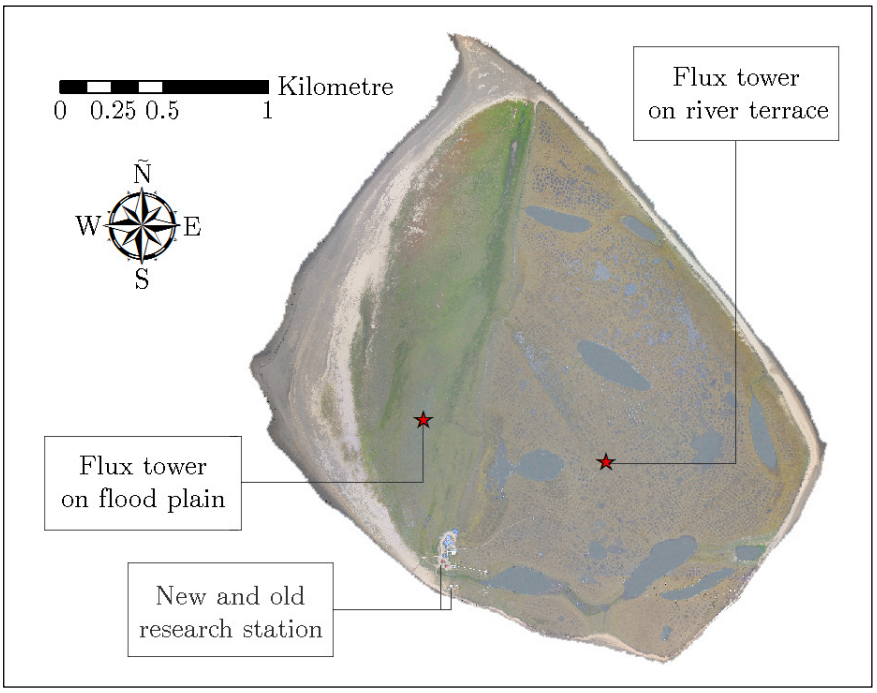

Figure 10 Orthomosaic of Samoylov Island displaying the locations of the two flux towers. The resolution of the orthomosaic amounted to 8.5 cm and was, thus, sufficiently high in order to consider the pronounced heterogeneity of the surface.

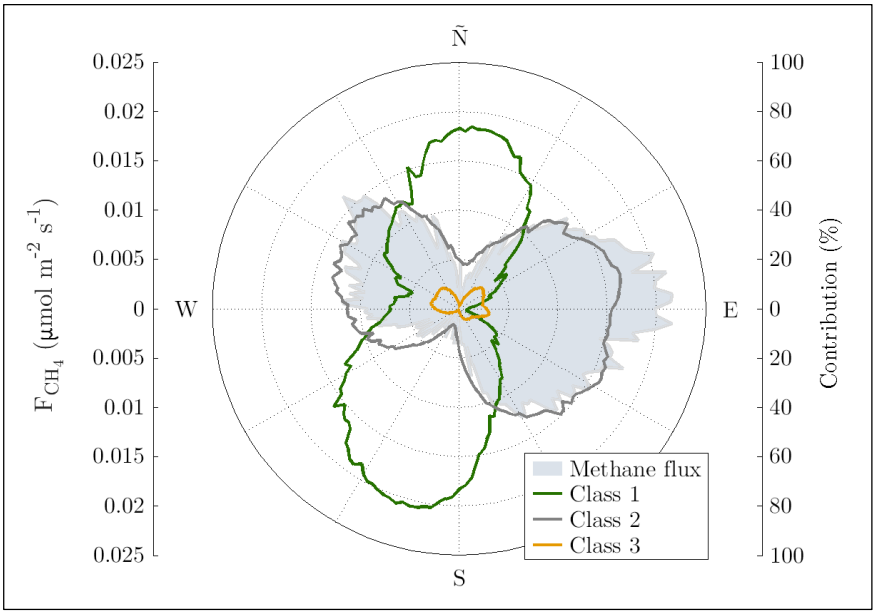

Figure 11 Wind direction dependencies of both methane flux and vegetation class contributions for both measurement periods 2014 and 2015. Elevated emissions scaled well with contributions from vegetation classes 2 and 3, whereas very little emissions were sampled, when vegetation class 1 largely contributed to the flux.

manually classified vegetation map for the fine-scale orthomosaic. Subsequently, the coincidence between both lowres maps was evaluated while the manually classified map was considered to constitute the true depiction of local vegetation classes.

Impact of the heterogeneity on the carbon fluxes

The spatial heterogeneity of the footprint exerted an impact on the distribution of methane sources and emission-free areas. Their approximate distribution around the flux tower became evident through the substantial variation in methane fluxes depending on wind direction (Figure 11). This variation coincided well with the contribution of the vegetation classes to the fetch. Very little methane emissions were captured during periods featuring northerly and southerly wind directions, when the fetch was characterised by vegetation class 1. In contrast, when the wind came from easterly and northwesterly directions, where vegetation classes 2 and 3 are situated, elevated methane emissions were ascertained. The strong coupling between the location of methane sources and the distribution of vegetation classes facilitated the modelling of fluxes. On the contrary, an evident wind direction dependency of carbon dioxide fluxes could not be detected, even when the dataset was separated into subsets with uniform irradiance and temperature classes in order to rule out discombobulating effects of the diurnal and seasonal cycle.

2.5. Flux modelling

In this work, the micrometeorological sign convention was adopted, i.e. negative fluxes indicate a downward gas transport from the atmosphere towards the ground, and accordingly, positive fluxes denote an upward gas transport from the ground into the atmosphere. Correspondingly, a negative budget constitutes a net uptake of carbon, whereas a positive budget identifies a net release of carbon.

2.5.1. Methane flux

The modelling of the observed methane flux time series was based on three models: a mechanistic model (MM), a stepwise regression (SR) and an artificial neural network (NN). All of these models have been found suitable for explaining the variability in observed methane fluxes (Dengel et al., 2013; Forbrich et al., 2011; Hanis et al., 2013). For the sake of comparability, all models were driven with the same half-hourly environmental input data.

Mechanistic model

The mechanistic model combines source area fraction weighted fluxes of the three vegetation classes in the footprint (Forbrich et al., 2011). Environmental variables utilised to drive the model were soil temperature and friction velocity. A relationship between soil temperature and methane flux has been found for Samoylov Island and

many other Arctic sites (Mastepanov et al., 2013; McEwing et al., 2015; Sachs et al., 2008; Wille et al., 2008). Furthermore, a link between ecosystem-scale methane flux and friction velocity has also been observed occasionally (Long et al., 2010; Matthes et al., 2014). The addition of further potential methane flux drivers such as water level, air pressure, active layer depth or gross primary productivity did not improve the performance of the initial model.

$$F_{CH_4} = \sum_{i=1}^{i=3} \Omega_i \cdot a_i \cdot exp^{(b_i \cdot T_{soil_i} + c_i \cdot u_i^*)} \quad (4)$$

F_{CH4} is the net methane flux observed at the flux tower, T_{soil} is soil temperature (Figure 12a), u* is friction velocity (Figure 12b), and a, b, c are vegetation class-specific fitting parameters, which were estimated employing non-linear ordinary least-squares regression. The parameter "a" can be interpreted as a base flux, and "b" as well as "c" denote the sensitivity of the methane flux towards soil temperature and friction velocity, respectively. Ω is the relative contribution of each vegetation class to the flux (Figure 12c), i.e. it acts as a weight, and was obtained through (i) computing the source weight function for a flux interval, (ii) discarding all values of this 2D-function outside an area of 1 km^2 with the flux tower in the middle, (iii) spatially discretising the source weight function with a resolution of 1 m^2 in the remaining area, (iv) assigning each value of the source weight function to a vegetation class, and (v) summing the values in each vegetation class. The vegetation map underlying the footprint model was the fine-scale orthomosaic (instead of the manually classified vegetation map). Modelling a flux in a spatially variable footprint requires modelling at a high temporal resolution in order to take the constantly changing source area composition into account. Hence, modelling in this study was - as opposed to various other methane emission-related studies utilising daily means - based on half-hourly flux data. In the process of model development, the initial model was adjusted to the characteristics of the flood plain whilst both complying with the principle of parsimony and preventing unwanted model artefacts. This adjustment included the differentiation of methane fluxes between the three vegetation classes: methane emissions close to zero (class 1) and distinct methane emissions (classes 2 and 3). Since the methane flux from class 1 was anticipated to be of very minor magnitude, a flux dependency on soil temperature or friction velocity did not persist; thus, only the parameter "a" representing a base flux was retained for class 1. Soil temperatures measured at different depths by the northern probe were utilised to model the methane fluxes of class 2 (30 cm depth) and class 3 (10 cm depth) by parametrising the two "b" parameters. For modelling the relationship between friction velocity and methane fluxes of classes 2 and 3, only one "c" parameter was applied since friction velocity was determined for only one height and

deemed to have the same implication on the methane fluxes of both classes. These adjustments yielded the final mechanistic model.

$$F_{CH_4} = \Omega_1 \cdot a_1 + \sum_{i=2}^{i=3} \Omega_i \cdot a_i \cdot exp^{(b_i \cdot T_{soil_i} + c \cdot u^*)} \quad (5)$$

This model constitutes the main methane flux model in this study. In order to put its ability to explain methane emissions in context with other models, two more models were applied.

Stepwise regression

The stepwise regression was employed to devise a multilinear model based on multiple terms, which account for the impact of environmental controls on the methane flux. This model is incrementally optimised by adding or removing these terms depending on their statistical significance ($P<0.05$). During the optimisation, each term's coefficient is examined whether it is significantly different from zero or not, and consequently included in or excluded from the model. In this course multiple variations of terms may be tested until the model stops improving (Draper and Smith, 1998).

Neural network

The artificial neural network is a two-layer feed forward network consisting of sigmoid neurons in the hidden layer as well as linear neurons in the output layer. Initially, the dataset is partitioned into training data (70 %) and validation data (30 %). The environmental controls of both subsets are then fed into the model and flow in a forward direction through both layers, which consist of a set of nodes with weights. The model produces an output by employing both initially random weights and activation functions. Based on these modelled fluxes and the observed fluxes in the respective two subsets, a training and a validation error is defined. The minimisation of these errors is achieved through the backpropagation algorithm, in which the training error propagates in a backward direction through the network optimising the weights of all nodes. While this sequence of executing and adjusting the network is repeated multiple times (training process), the training error continues to decrease, whereas the validation error typically starts to increase after a certain number of epochs, when overfitting arises. At this stage, the weight adjustments terminate (early stopping). Every model run generates different results due to different initial conditions (Haykin, 1999). In order to assess the overall performance, the model was run 100 times, and the outputs of all 100 networks were averaged (ensemble averaging).

Generalisability of the models

In order to assess the models' generalisability, i.e. its robustness towards a varying input whilst maintaining predictive power, all three models were evaluated by driving them with 2014 data while applying the calibration obtained with 2015 data and vice versa.

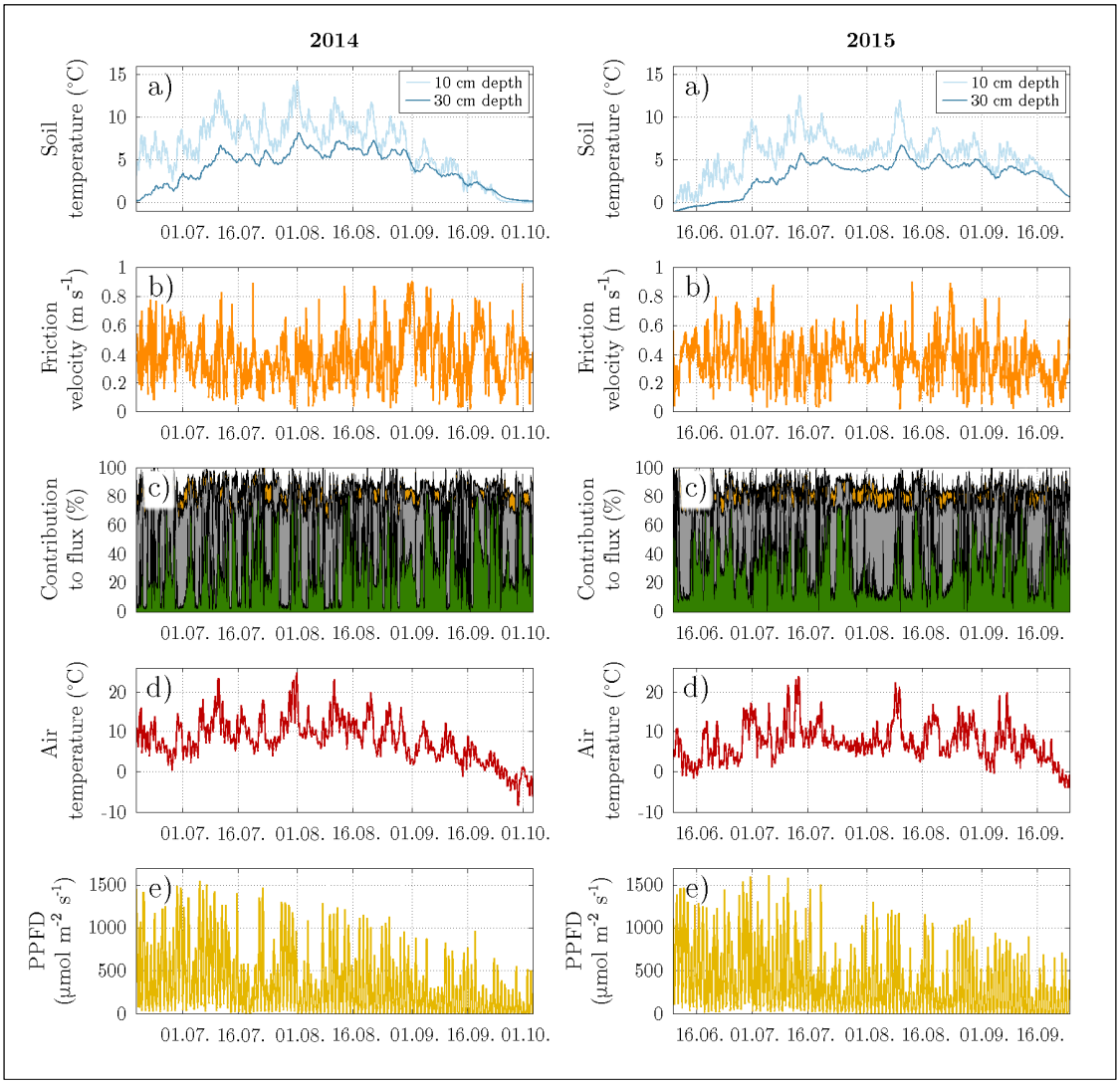

Figure 12 Temporal dynamics of environmental parameters applied for modelling methane and carbon dioxide fluxes in measurement periods 2014 and 2015. a) Soil temperatures at a depth of 10 cm and 30 cm. b) Friction velocity. c) Contribution of vegetation classes to flux signal (green=class 1, grey=class 2, yellow=class 3). For the modelling of F_{CH4}, all of the three Ω were applied, whereas for the modelling of F_{CO2}, both Ω of vegetation classes 2 and 3 were summed up. The vegetation map underlying the footprint model to output the contributions was the fine-scale orthomosaic. d) Air temperature. e) Photosynthetically active photon flux density.

These combinations of calibration and test data from different years were utilised for filling data gaps as well as the common approach where calibration and test data derive from the same year. The subsequent integration of the complete time series yielded footprint budgets that were compared with respect to the underlying model plus model calibration period.

Estimation of robust budgets with multiple scaling steps

The footprint budgets of the flood plain ought to be interpreted with caution; the reason being that the estimated budget of an ecosystem with a heterogeneous surface is dependent on location and height of the flux sensor, whose measurements in turn depend on wind direction, wind field properties and atmospheric stability (Schmid and Lloyd, 1999). This aspect applies to many Arctic ecosystems where small-scale heterogeneities in land cover are characteristically abundant (Muster et al., 2012). A robust budget requires measurements in a footprint that is considered representative, i.e. the footprint exhibits the same distribution of surface elements as the area of interest for all wind sectors. If this condition is not fulfilled, a budget suffers from a sensor location bias. Due to an insufficient number of high-resolution images of the Lena River Delta, the typical vegetation composition of flood plains in the delta remains unknown. Hence, the total area of the flood plain of Samoylov Island was designated as the area of interest.

The mechanistic model, which approximates the observed net methane flux by summing the three modelled methane fluxes of the three vegetation classes, also enables the estimation of the individual methane fluxes, which account for the three respective vegetation classes. The basis for this downscaling is a robust calibration, i.e. the model fit is acceptable and the fitting parameters have taken on reasonable values. Subsequently, integrating the three downscaled fluxes and projecting the budgets on the respective spatial extent of the vegetation classes on the flood plain forms the upscaling. The class designating the bare sand along the waterfront was not considered in the upscaling since its methane emissions were (in comparison to the other classes) assumed negligible (Figure 6c). The class denoting the water bodies, on the other hand, was appended to vegetation class 3 since the few small water bodies surrounded by sedges were presumed to have similar flux rates. Finally, summing the three upscaled budgets of the vegetation classes yields the methane emission of the total area of the flood plain. Taking advantage of the now absent sensor location bias, the flood plain budgets of 2014 and 2015 can be compared. For this purpose, the two budgets were computed for the comparison period 18th June to 24th September, where data is available in both years (98 days).

2.5.2. Carbon dioxide flux

The modelling of the observed carbon dioxide flux time series was based on one model, which required a comprehensive calibration in the course of multiple reparameterisations.

Model design

The model structure fundamentally rests on the estimation of the two components of the carbon dioxide flux.

$$F_{CO_2} = NEE = TER + GPP \quad (6)$$

F_{CO2} is the net carbon dioxide flux observed at the flux tower, and equals NEE, the net ecosystem exchange. Its two components TER and GPP denote, respectively, the total ecosystem respiration and the gross primary productivity. These components are antipodal: while the respiration has a positive sign, the primary productivity has a negative sign. Depending on their magnitudes, NEE possesses either a positive or a negative sign, i.e. dissimilation outweighs assimilation or vice versa.

Since respiration is related to the metabolism of organisms, it is a direct function of temperature. Therefore, different temperatures, e.g. air, surface or soil temperature, have been repeatedly successfully employed for modelling respiration fluxes (Kutzbach et al., 2007b; Lasslop et al., 2010). A useful description of this relationship is the Q_{10} model (van't Hoff, 1898).

$$TER = R_{base} \cdot Q_{10}^{\left(\frac{T_{air}-T_{ref}}{\gamma}\right)} \quad (7)$$

The variable R_{base} denotes the basal respiration at the reference temperature (T_{ref}), which was set to 15 °C, and γ was held constant at 10 °C (Mahecha et al., 2010). Q_{10} indicates the temperature sensitivity; i.e. this variable states a value by which respiration multiplies/divides, when the temperature rises/drops by 10 °C. Both parameters R_{base} and Q_{10} are best-fit parameters, which were estimated via non-linear ordinary least-squares regression utilising air temperature (T_{air}) as regressor (Figure 12d).

Since photosynthesis is strongly dependent on irradiance, the photosynthetically active photon flux density (PPFD) was employed as a regressor for modelling photosynthesis (Figure 12e). This modelling was based on a rectangular hyperbola function (Michalies and Menten, 1913).

$$GPP = -\frac{P_{max} \cdot \alpha \cdot PPFD}{P_{max} + \alpha \cdot PPFD} \quad (8)$$

The variable P_{max} is the maximum photosynthetic potential and quantifies the theoretical maximum of photosynthesis at infinite PPFD. α is the initial quantum efficiency, i.e. it states the slope of the function at PPFD being zero. Both parameters P_{max} and α are best-fit parameters, which were also found employing non-linear ordinary least-squares regression. This function assumes that the photosynthesis is not affected by temperature effects or limitation through a high vapour pressure deficit.

The net carbon flux can be computed by modelling respiration and photosynthesis simultaneously (Runkle et al., 2013; Wille, C., personal communication, 2017).

$$NEE = R_{base} \cdot Q_{10}^{\left(\frac{T_{air}-T_{ref}}{\gamma}\right)} - \frac{P_{max} \cdot \alpha \cdot PPFD}{P_{max}+\alpha \cdot PPFD} \quad (9)$$

In order to take the heterogeneity of the footprint into account, further modification involved the addition of the relative contributions of each vegetation class Ω (Figure 12c). In contrast to the methane flux modelling, where three vegetation classes were employed, the modelling of carbon dioxide fluxes was based on the application of only two vegetation classes. This reduction of classes was due to comparatively lower differences in carbon dioxide flux rates between the three classes, which was suggested by the absent wind direction dependency. Since the vegetation classes 2 and 3 resembled each other in terms of near-surface moisture, moss properties and vegetation, similar carbon dioxide flux rates could be anticipated, and, thus, both classes were merged for the modelling of carbon dioxide fluxes. This "new" vegetation class 2 & 3 was characterised by a moist to wet surface dominated by sedges with abundant moss. Vegetation class 1 did not change and remained characterised by a dry surface with bushes and somewhat moss. These modifications formed the final model employed for carbon dioxide flux modelling.

$$NEE = \sum_{i=1}^{i=2} \Omega_i \cdot \begin{pmatrix} R_{base,i} \cdot Q_{10,i}^{\left(\frac{T_{air}-T_{ref}}{\gamma}\right)} \\ - \frac{P_{max,i} \cdot \alpha_i \cdot PPFD}{P_{max,i}+\alpha_i \cdot PPFD} \end{pmatrix} \quad (10)$$

Model calibration

Fitting the final model to the observed flux data involved a gradual simplification of the model due to its potential overparameterisation. This risk resulted from the large number of fitting parameters (R_{base}, Q_{10}, P_{max}, α for each vegetation class) given the limited amount of observed flux values. The alterations in parametrisation were necessary to obtain (i) reasonable seasonal courses of the fitting parameters, i.e. the courses displayed a predominantly smooth evolution with elevated values during the growing season and low values before and after the growing season, and (ii) meaningful and significant values for the fitting parameters, i.e. the values were not negative as well as within an acceptable range and their 95 % confidence interval did not overlap zero. Achieving both objectives provided the opportunity to interpret the fitting parameters whilst precluding equifinality associated problems. Furthermore, the reason for interannual flux variabilities could be more specifically elucidated based on the fitting parameters. The fitting procedure included only quality-controlled fluxes, and comprised four steps (Figure 13).

Step №1: The procedure first fitted the final model to the observed fluxes of each day utilising a moving window with a fixed size of 14 days (Figure 14). The choice of a suitable window size was based on identifying an optimum between two conflicting demands: the window size ought to have been as

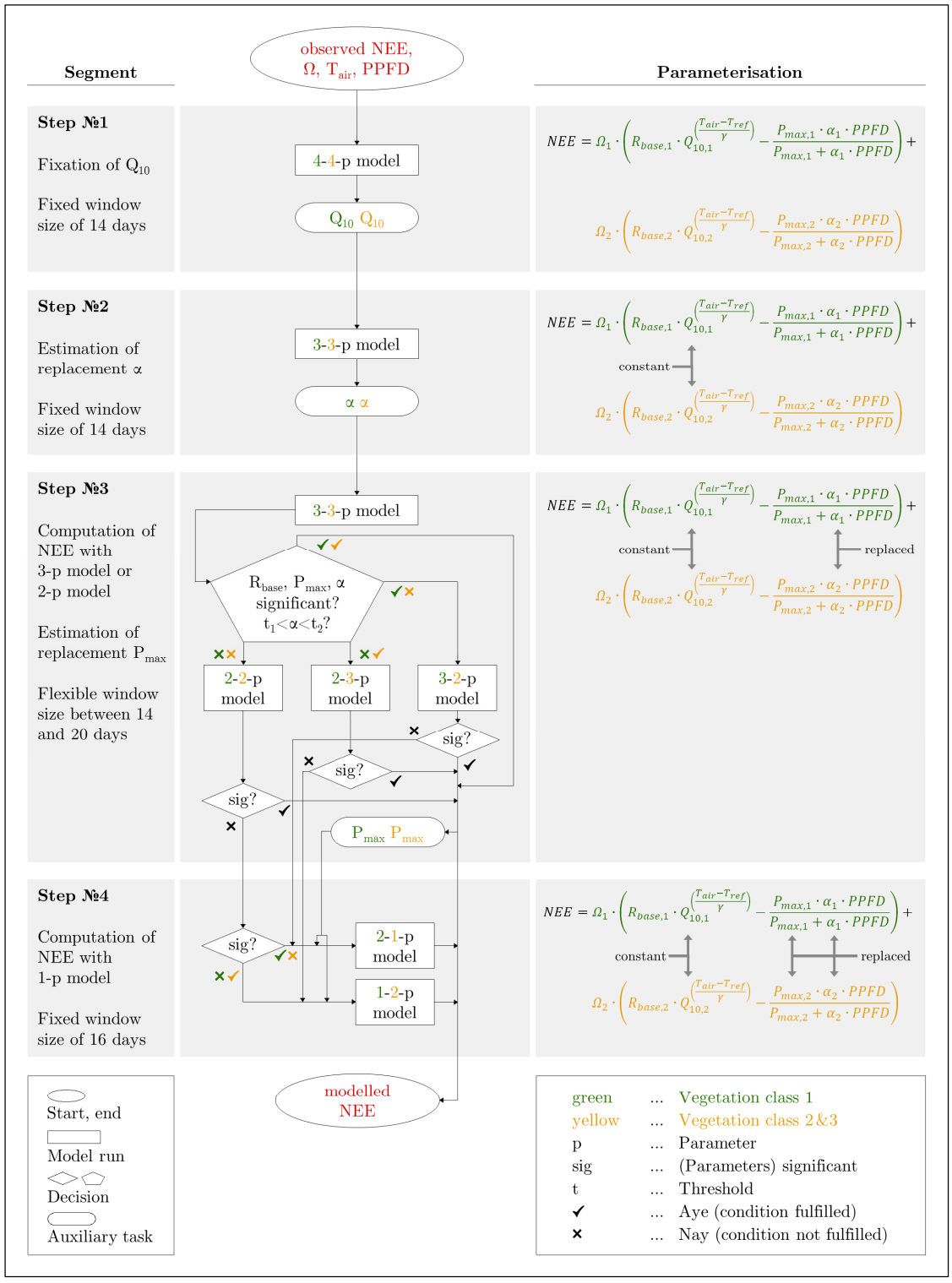

Figure 13 Schematic overview of the modelling of carbon dioxide fluxes. The algorithm contains four steps within different parameterisations of the flux model were applied to obtain meaningful and significant fitting parameters (R_{base}, Q_{10}, P_{max}, α). The values (e.g. 3-2-p model) denote the number of parameters to be fitted.

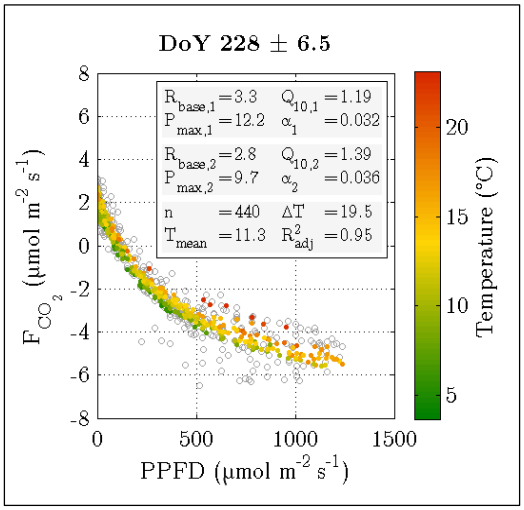

Figure 14 Example of the fitting process at the day of the year (DoY) 228 (16th August) in 2014. The grey and coloured circles denote the observed and modelled fluxes, respectively. The textbox displays the four estimated fitting parameters R_{base} and P_{max}, both in (µmol m^{-2} s^{-1}) as well as Q_{10} and α for vegetation class 1 and vegetation class 2 & 3. The textbox further depicts the number of flux samples (n), the mean air temperature (T_{mean}) in (°C), the temperature spread (ΔT) in (°C) and the adjusted coefficient of determination (R^2_{adj}). It is evident, that the model captured the variability of the observed data.

small as possible to capture most of the variability in fluxes, whereas the window size ought to have been as large as possible to obtain less noisy time series of preferably significant values of the eight fitting parameters. Running the model with varying window sizes and counting the number of significant values for each model run revealed the following: increasing the window size caused the number of significant values to rise, soon to level off, and eventually at a window size of 14 days, to remain at similar values. Prior to calibrating the model, the following requirements needed to be satisfied for every window: sufficient flux samples were available (at least 80 % data coverage), the air temperature spread did not fall below 12 °C, and the mean air temperature did not drop below -10 °C. Imposing these requirements was meant to ensure robust and representative fits.

The purpose of this step involved the fixation of Q_{10} in order to prevent overparameterisation, and further, alterations in temperature sensitivity were thought to be less plausible and hence expected to be negligible. This assumption was confirmed by the time series of estimated Q_{10} values displaying an implausible variability, whereas the other fitting parameters presented a rather seasonal course. Based on the deliberation of negligible alterations in temperature sensitivity during both years, the model was run for 2014 and 2015 together during this step, whereas the model was respectively run for the measurement periods 2014 and 2015 during the next steps. The application of a larger period provided more data points, with the aid of which Q_{10} could be fixed at a more representative value. Two final Q_{10} values were determined for each vegetation class by calculating the median out of all estimated best-fit Q_{10} values, which both were significant and possessed an adjusted coefficient of determination (R^2_{adj}) of 0.75 or greater.

Step №2: The model was run with Q_{10} being fixed throughout the measurement periods 2014 and 2015 applying a moving window with a fixed size of 14 days and a step size of 1 day again. The requirements laid down in the previous step prior to fitting had to be met again except the requirement of a sufficient air temperature spread.

The aim of this step comprised the creation of two replacement functions for α after six best-fit parameters were estimated. The necessity for replacement functions arose through large peaks in the time series of α. These peaks tended to occur at the onset of the growing season and were, thus, deemed spurious. Large α values would have promoted photosynthesis, which was of rather minor magnitude at that time of the year. In order to reproduce the low observed NEE, the erroneously elevated GPP was counteracted by a mistakenly enhanced TER utilising a large R_{base}. The resulting problem of equifinality would, hence, hamper the interpretation of the fitting parameters.

To prevent this adverse circumstance, the two replacement functions, one for each vegetation class, were calculated by fitting a Gaussian bell curve to the time series of significant α values. In addition, two threshold functions were computed for each replacement function by adding/subtracting 30 % of the function values to/from the replacement function. Hence, the threshold functions formed an interval around the replacement function within the estimated α values were accepted during the further procedure. The threshold of 30 % was visually selected since this value generated an interval outside of which only the peaks were situated, i.e. spurious and meaningful α values could be reliably separated.

Step №3: The model was initially run with the same parameterisation as in the previous run, but employing a moving window with a flexible size for every day. The application of a flexible window allowed a closer reproduction of the variability in the observed data through adjusting its size. However, since small windows were in conjunction with a small amount of flux samples, which increased the risk of estimating insignificant parameters, every fit required a minimum of 240 flux samples, which equals 5 days with 48 fluxes per day. Based on this setting, the model was run and the estimated parameters were checked for significance. If one best-fit parameter was insignificant, the window size was increased by one day and the model was run again. This procedure was repeated until a maximum window size of 20 days, if all fitting parameters were not significantly estimated before utilising a preferably smaller window size.

The objective of this step included the bulk of model calibration within the fitting procedure. Hence, after the initial model run of this step, its output was inspected in two respects: the significance of the remaining fitting pa-

rameters (R_{base}, P_{max}, α) and the location of α (inside or outside the acceptance interval). In case of all six fitting parameters being significant and the two fitted α were situated between the respective thresholds, the estimated NEE was accepted and appended to the modelled time series. If one criterion/both criteria was/were not fulfilled, another model with less best-fit parameters was run employing, again, a moving window with a flexible size for every day. This simplification comprised the application of α values adopted from the previously defined replacement function. The model choice depended on the vegetation class, where the criterion/criteria was/were not satisfied. Hence, α values from the replacement function were employed for either one or both vegetation classes. For instance, if the fitting parameters of only one vegetation class were insignificant, only this vegetation class was refitted applying a replacement α whilst reutilising the retained significant fitting parameters of the other vegetation class. Subsequently, the significance of the re-fitted parameters was examined. If all parameters were significant, the correspondingly estimated NEE was added to the modelled time series. Any remaining insignificances were otherwise dealt with in the next step.

In preparation for the next step, the last task of this step involved the creation of two replacement functions for P_{max}. This fitting parameter was chosen over R_{base} since P_{max} featured more insignificant values than R_{base}. Once again, a Gaussian bell curve was fitted to the time series of significant P_{max} values of each vegetation class.

Step №4: Towards the end of the procedure, a greatly simplified model was run for each day deploying a moving window with a fixed size. This size corresponded to the average of all window sizes found during the previous step.

The goal of this step encompassed the remaining model calibrations for a complete time series of modelled NEE. To achieve such a target, the model included only three best-fit parameters: R_{base} twice and P_{max} once. The second P_{max} for the other vegetation class was adopted from its previously calculated replacement function. This confined parameterisation was, given a constant amount of observed flux samples, associated with an elevated number of degrees of freedom, which in turn allowed a more precise estimation of the remaining fitting parameters, i.e. their confidence intervals were smaller. In this way, all best-fit parameters were significant and could be utilised for a reliable modelling of NEE.

Interpretation of the model parameters

A major benefit of the four fitting parameters lies in the possibility that they are physiologically interpretable and, thus, allow both drawing inferences about intrinsic ecosystem features such as the capacity of carbon

uptake/release or the sensitivity to changes in environmental conditions. This interpretation is aided by considering the functional relationship with NEE, which becomes apparent through plotting a family of curves (Figure 15):

- R_{base}, as the basal metabolic rate of an ecosystem, indicates both the respiring canopy and the microbial activity in the soil, which largely depends on the availability of nutrients as well as oxygen and, hence, on the soil moisture content. R_{base} is subject to a seasonal course since both canopy metabolism and microbial activity are elevated during the warmer period, causing the curves to shift along the ordinate. During the cold period, R_{base} also forms an important parameter since it describes the ongoing release of carbon dioxide, which might largely affect the annual carbon balance.

- Q_{10}, as the respiration's strength of dependence on temperature, indicates the metabolic efficiency of respiring organisms in an ecosystem. This manifests in the slope of the curves. Large Q_{10} values might cause NEE to decline (less negative) at high PPFD, as the continuously rising TER prevails the constant GPP. This effect can also occur through stomatal closure or light stress. The point of intersection in the family of curves is set by $T_{ref;}$ altering T_{ref} causes the intersection to move along the abscissa.

- P_{max}, as the maximum photosynthetic capacity, indicates the amount of biomass in an ecosystem. On account of canopy growth and the development of foliage during the growing season, P_{max} is also subject to a seasonal course. Furthermore, P_{max} comes into effect at a high irradiance, which is expressed by shifting the curves along the ordinate at high PPFD levels.

- α, as the light sensitivity, indicates the efficiency of the photosynthetic apparatuses in an ecosystem's canopy. This parameter determines the shape of the curves, and is important since it takes effect at a low irradiance, which is more common than a large irradiance. This aspect is even more applicable during shoulder seasons, when α is low. Altering α in the lower range causes curves with a distinctly new shape.

Estimation of robust budgets with multiple scaling steps

The applied model offers multiple downscaling capabilities as it constitutes an additive model that sums several sub-fluxes, which account for flux components as well as vegetation classes. In the first place, the observed fluxes could be partitioned into TER and GPP, which account for the entire footprint. Furthermore, these component fluxes plus NEE could also be computed for each vegetation class in the footprint. A reliable estimation of these individual fluxes was fostered by

the restrictive acceptance of meaningful and significant values for the fitting parameters during the fitting process. Similarly to the methane fluxes, the downscaled carbon dioxide fluxes were subsequently upscaled by integrating and projecting them on the respective spatial extent of the vegetation classes on the flood plain. Again the vegetation class of bare sand was neglected and the vegetation class of water bodies was appended to vegetation class 2 & 3. The final summation of the two upscaled budgets yielded the carbon dioxide budget of the flood plain, which does not lack a sensor location bias. For the sake of comparability between the years and with methane budgets, the carbon dioxide budgets were calculated for the period of 18th June to 24th September.

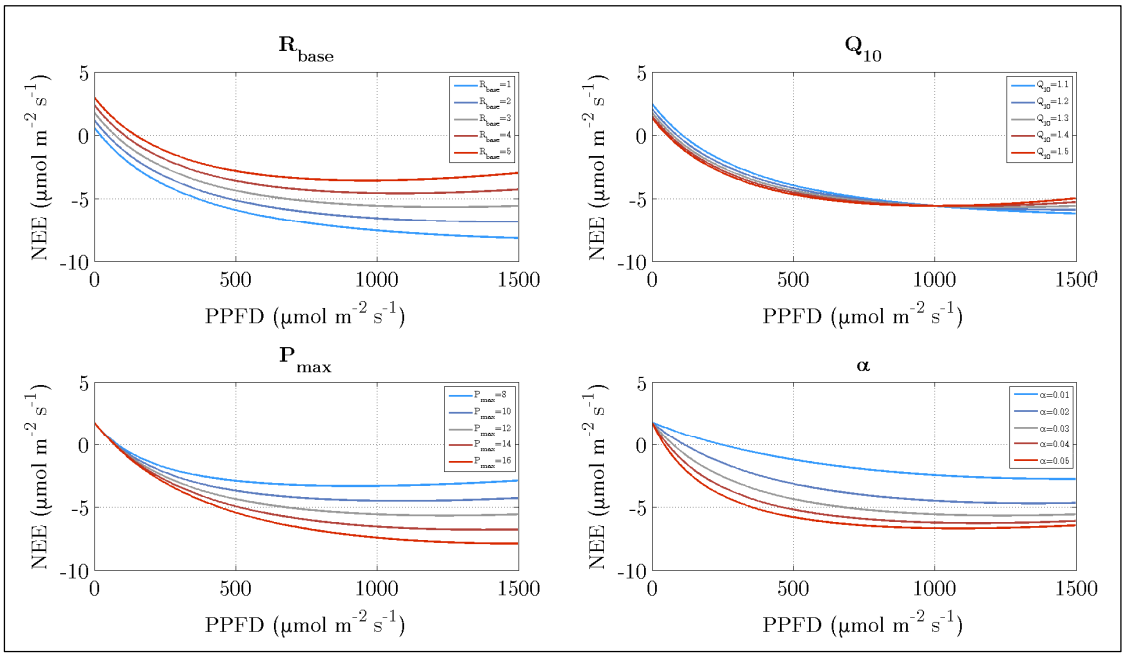

Figure 15 Implications of the four fitting parameters on the modelled carbon dioxide flux. The values of the fitting parameters, plugged into equation 9, varied in a typical magnitude and are displayed in the legends. During this variation, the respectively remaining three parameters were held constant at R_{base}=3 µmol m^{-2} s^{-1}, Q_{10}=1.3, P_{max}=12 µmol m^{-2} s^{-1}, α=0.03. In order to aid visual clarity, the units were omitted in the legends. Besides the applied PPFD range between 0 and 1500 µmol m^{-2} s^{-1}, a temperature range between -5 to 25 °C was utilised. The most influential fitting parameters are R_{base} and α due to their implications on NEE in the entire PPFD spectrum. In particular α matters on account of its sensitivity at commonly low PPFD rates.

2.5.3. Greenhouse gas flux

For balancing the overall carbon flux dynamics of the flood plain, the flood plain budgets of both methane and carbon dioxide were compiled. In order to allow a quantitative comparison between both greenhouse gases, the methane budget (given as a mass flux instead of a molar flux) was converted to a carbon dioxide equivalent budget. Subsequently, this equivalent and the carbon dioxide budget were summed up yielding the greenhouse gas budget. The conversion of the methane budget was conducted utilising two different concepts: global warming potential (GWP) and global temperature change potential (GTP). Both metrics are being applied in the current assessment report of the intergovernmental panel on climate change (IPCC).

GWP is defined as the radiative forcing of a greenhouse gas other than carbon dioxide integrated over a certain time horizon compared to the release of an equal mass of carbon dioxide over the same period (Myhre et al., 2013). Hence, GWP can be interpreted as a measure of energy added to the climate system by the greenhouse gas in question relative to carbon dioxide, i.e. how much heat is trapped in the atmosphere by a greenhouse gas compared to the reference gas carbon dioxide. Consequently, GWP incorporates the properties of the considered greenhouse gas such as lifetime and radiative efficiency. On account of the short lifetime of methane in the atmosphere, its GWP is almost entirely determined by carbon dioxide roughly five decades after a pulse emission.

GTP goes one step down the cause-and-effect-relationship and is defined as the ratio of change in global mean surface temperature that is caused by a greenhouse gas other than carbon dioxide at a certain point in time, compared to the changed temperature caused by carbon dioxide at the same point (Myhre et al., 2013). Since GTP describes the effect of an altered radiative forcing, it considers, in contrast to GWP, physical processes in the climate system such as the (slow) response of the (deep) ocean to elevated greenhouse gas concentrations in the atmosphere.

GWP and GTP are expressed as factors, which weigh emissions of greenhouse gases other than carbon dioxide. In this study, the applied factors for methane amounted to 34 and 11, respectively, and were based on a time horizon of 100 years including climate carbon feedbacks; i.e. changes in carbon storage due to changes in climate were considered (Myhre et al., 2013). Finally, GWP has become the default metric for scaling emissions of various greenhouse gases to a common base, but there is currently no universally accepted methodology that considers all the relevant effects of greenhouse gases as a single metric.

3. Results

3.1. Environmental conditions

The mean air temperatures over the measurement periods in 2014 and 2015 were 7.7 °C and 7.1 °C, respectively (Figure 12d). The following maximum air temperatures were reached: 24.8 °C (31^{rst} July 2014) and 23.9 °C (13th July 2015). Furthermore, the gauged precipitation sums amounted to 92.3 mm and 130.4 mm for the measurement periods 2014 and 2015, respectively. For evaluating these values, long-term averages of air temperature and precipitation were determined for the same periods in the year as both measurement periods. Based on records for Samoylov Island gathered during the period 1998-2016, the average temperature and precipitation sum amount to 6.5 °C and 97.7 mm (2014) as well as 7.1 °C and 100.4 mm (2015), respectively. Consequently, the measurement period of 2014 was distinctly warmer and slightly drier than the baseline while the measurement period 2015 featured the same mean temperature as the baseline, but considerably more rain (Figure 16).

The respective mean soil temperatures in a depth of 10 cm and 30 cm amounted to 6.4 °C and 4.1 °C in the measurement period of 2014 as well as 5.4 °C and 3.1 °C in 2015 (Figure 12a). By analogy with air temperatures, soil temperatures in 2014 were greater than in 2015; hence, the active layer has reached a larger thickness. Depending on snow cover, the soil started warming in May and thawing in June. In 2015, when the soil was still deep-frozen at the time, at which the spring flood deluged the flood plain, the water delivered sufficient heat to warm the soil surface in the range around 0 °C. Soil temperatures at 10 cm and 30 cm depth exceeded 0 °C in first half and second half of June respectively. During the warm season the highest soil temperatures were gathered at 10 cm during July and at 30 cm during August. In late September, they dropped down to 0 °C again forming the onset of the zero curtain period, which lasted until early November at 10 cm depth and late November at 30 cm depth. At 100 cm depth, the zero curtain period extended into late January, when the soil was entirely refrozen.

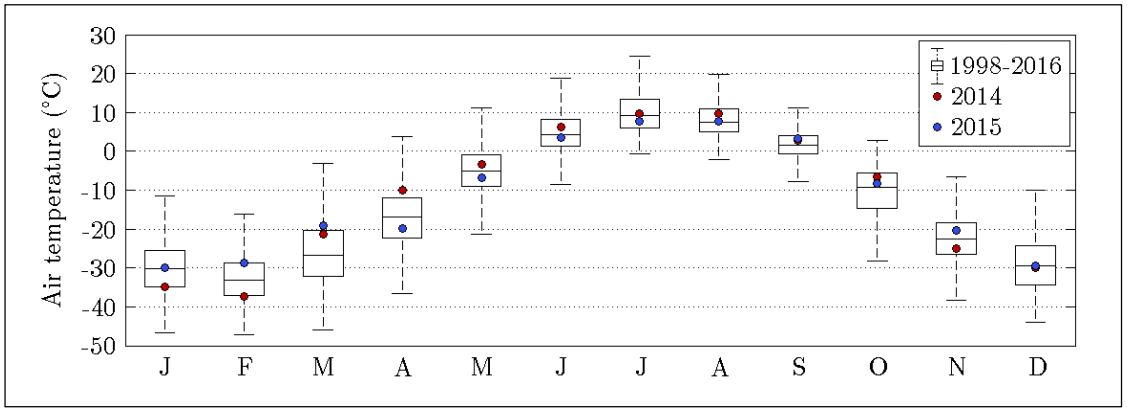

Figure 16 Monthly medians of air temperature on Samoylov Island for the years 2014 and 2015 as well as boxplots of the 1998-2016 baseline. In each box, the central mark denotes the median, and the bottom and top edges of the box indicate the 25th and 75th percentiles, respectively. The whiskers extend to the most extreme data points excluding outliers. During the warm season, when flux data was available (June to September), 2014 was mostly warmer than 2015.

The photosynthetically active photon flux density followed long-term statistics with the following exceptions: slightly more was recorded in July 2014, distinctly less in July 2015 and somewhat less in August 2015. In general, the largest radiative input occurs in May and June from which it gradually drops to zero during polar night. Throughout the short growing season, the radiation was, hence, on the decline (Figure 12e).

The mean friction velocities and standard deviations for 2014 and 2015 amounted to 0.36 ± 0.16 m s^{-1} and 0.35 ± 0.15 m s^{-1} respectively (Figure 12b). The turbulence test by means of integral turbulence characteristics revealed that turbulent conditions were well-developed during roughly 92 % of the time. In this context a critical friction velocity of 0.18 m s^{-1} was determined.

Prevailing wind directions for the measurement period were easterly and north-westerly for both years. This similarity results in mean contributions of vegetation classes to the methane flux being similar for both years: classes 1, 2 and 3 were sampled at 33.9 %, 46.2 % and 6.6 % in 2014 and at 37.2 %, 41.9 % and 7.1 % in 2015 (Figure 12c). Summing the respective contributions yields the total contribution of the three vegetation classes of interest, which averages at 86.5 %. The majority of the remaining contribution can be attributed to the sandy waterfront west of the tower and surface units of the easterly river terrace including polygon centres and rims as well as thermokarst lakes. Furthermore, 90 % of the observed fluxes were generated within a mean radius of approximately 250 m around the flux tower.

3.2. Dynamics of observed fluxes

3.2.1. Methane flux

The methane fluxes exhibited a seasonal course during the vegetation period with the following fluxes averaging 2014 and 2015 data (Figure 17): rising in June and July (0.011 µmol m^{-2} s^{-1}), peaking in August (0.014 µmol m^{-2} s^{-1}) and declining in September (0.008 µmol m^{-2} s^{-1}). The mean methane emission, averaged over both measurement periods, amounted to roughly 0.012 µmol m^{-2} s^{-1} (Figure 19a). Furthermore, the largest emission of both periods amounted to 0.034 µmol m^{-2} s^{-1} (11^{th} July 2014) and 0.029 µmol m^{-2} s^{-1} (6^{th} August 2015).

While the temporal variability on the seasonal scale was rather low, the temporal variability on the daily scale was considerably higher. However, this was not due to a diurnal cycle, which could not be detected, even when the dataset was partitioned into subsets that comprised only wind directions with methane sources in the fetch. The considerable variability was a result of varying wind directions and associated alterations in the fetch (Figure 11).

These alterations plus differing air temperatures also caused a minor interannual variability. The pronounced seasonal course in 2015 with large emissions in summer and low emissions in spring was due to prolonged easterly wind directions in late July and early August as well as a comparatively cold June (Figure 16). In 2014, the spring was on average warmer triggering higher methane emissions at the onset of the emission period, which led to a less conspicuous seasonal course. In autumn, the similar mean source area composition as well as the similar mean air temperatures caused methane emissions being alike in magnitude at that time of the year 2014 and 2015.

3.2.2. Carbon dioxide flux

The carbon dioxide fluxes expectedly exhibited both a seasonal and a diurnal course with the following fluxes averaging 2014 and 2015 data (Figure 20). Between the snowmelt and the growing season, the carbon dioxide fluxes remained slightly positive (0.26 µmol m^{-2} s^{-1}). With the onset of the vegetative phase in late June, stalks and foliage began to grow and the uptake of carbon dioxide during daytime outweighed the release of carbon dioxide during nighttime (-1.06 µmol m^{-2} s^{-1}). The intensity of this oscillation increased towards the onset of the reproduction phase in mid-July, where flowers and seeds were developed. During this phase, the most negative fluxes occurred featuring a relatively constant magnitude (-1.77 µmol m^{-2} s^{-1}). With the onset of the ripening phase in early August, bushes and sedges verged on full maturity, and the flux amplitude of the diurnal cycle began to be progres-

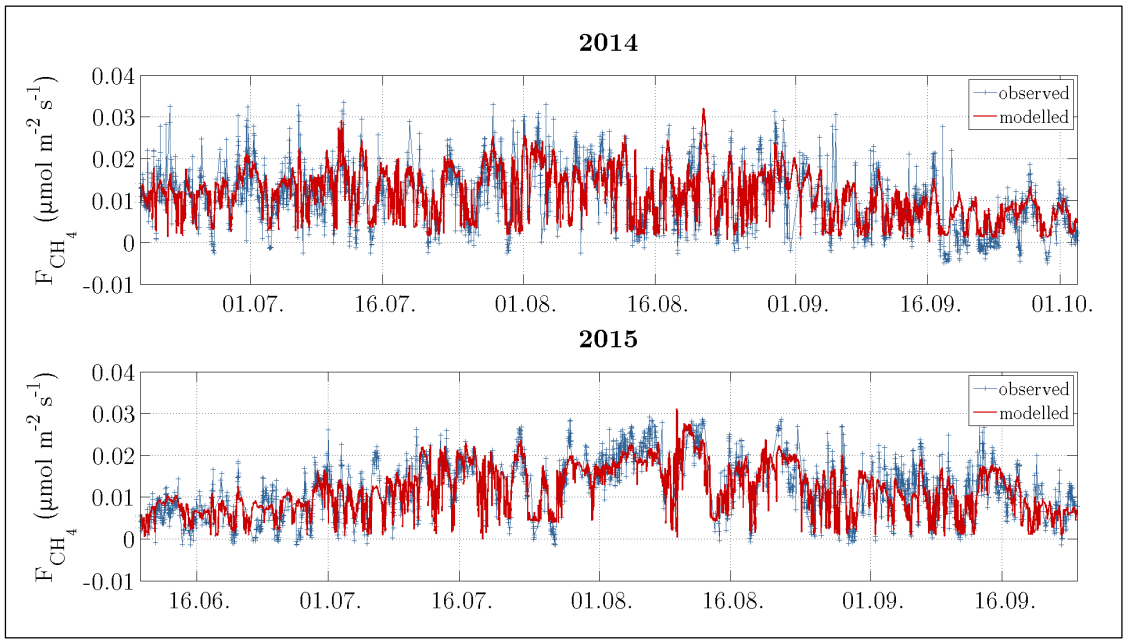

Figure 17 Time series of observed methane fluxes after conducting the quality assessment and modelled fluxes utilising the mechanistic model. While the seasonal course followed soil temperatures at shallow depths exhibiting low variability, the diurnal variability was substantially higher and governed by the varying fetch.

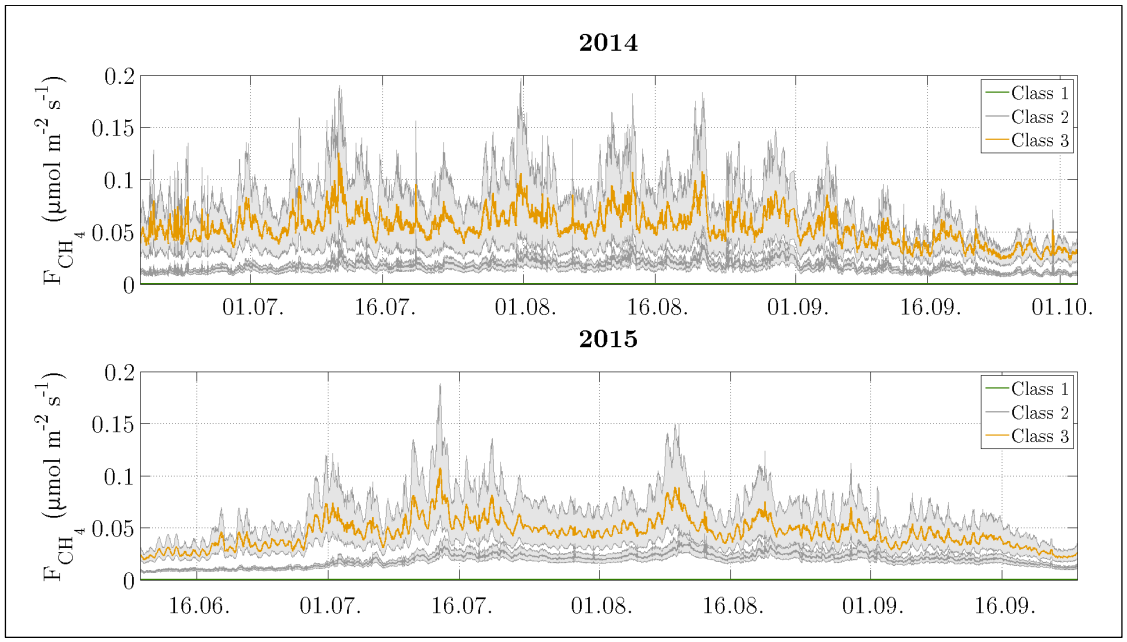

Figure 18 Time series of decomposed fluxes with 95 % confidence intervals accounting for the three vegetation classes of methane flux modelling. All three flux time series differed significantly, and the flux of vegetation class 1 remained close to zero.

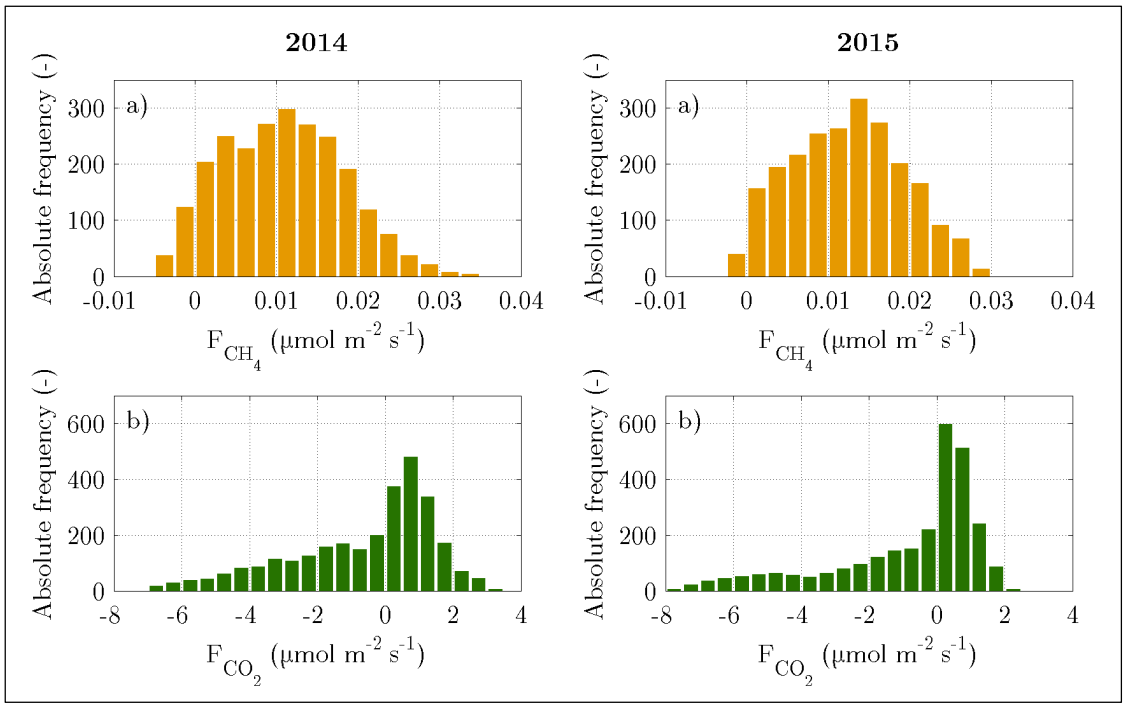

Figure 19 Histograms of the observed fluxes after the quality control: a) methane fluxes, b) carbon dioxide fluxes. The mean fluxes, averaged over both measurement periods, amounted to 0.012 µmol m^{-2} s^{-1} for methane and -0.61 µmol m^{-2} s^{-1} for carbon dioxide. Both fluxes exhibited a seasonal course with greater fluxes in summer and lower fluxes in the shoulder seasons. On the diurnal scale, their variability was more pronounced, however due to different reasons: the carbon dioxide fluxes varied mainly as a result of both the daily cycle of photosynthesis and meteorological conditions, while the larger temporal variability in methane fluxes was rather due to the spatial variability, i.e. the constantly varying source area composition in the fetch.

sively attenuated (-0.78 µmol m^{-2} s^{-1}). During the nights of this period, the most positive fluxes occurred. Towards late August, the respiration exceeded photosynthesis again indicating the onset of the senescence phase, which was associated with the colouration and shedding of leaves (0.39 µmol m^{-2} s^{-1}). After the end of the vegetation period in early September, when abscission was completed, the carbon dioxide fluxes continued to be positive again (0.55 µmol m^{-2} s^{-1}).

The mean net uptake, averaged over both measurement periods, amounted to -0.61 µmol m^{-2} s^{-1} (Figure 19b). During the growing season between late June and early September, when fluxes oscillated between net uptake and net release, the daytime fluxes ranged to -8 µmol m^{-2} s^{-1}, while the nighttime fluxes extended to 3 µmol m^{-2} s^{-1}.

The differing air temperatures of both years also caused a minor interannual variability during spring. Similar to the methane fluxes, the carbon dioxide

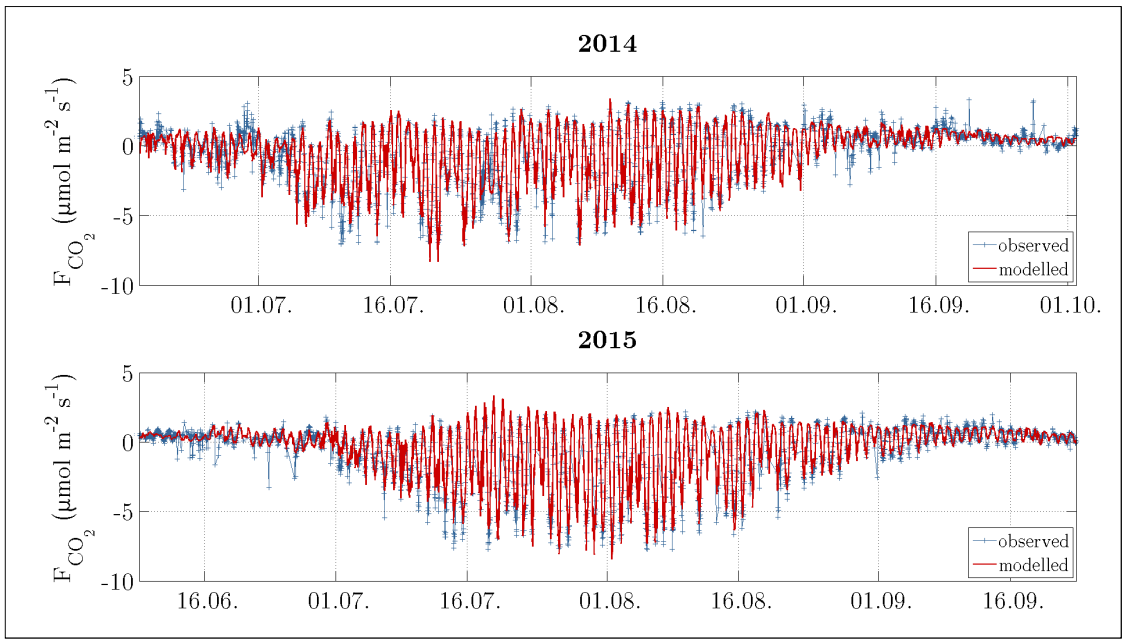

Figure 20 Time series of observed carbon dioxide fluxes after conducting the quality assessment and modelled fluxes (both NEE). During the growing season, which is indicated by elevated flux variability between late June and early September, the daytime uptake of carbon dioxide directly pursued the diurnal cycle of PPFD while the nighttime release of carbon dioxide was dependent on air temperature.

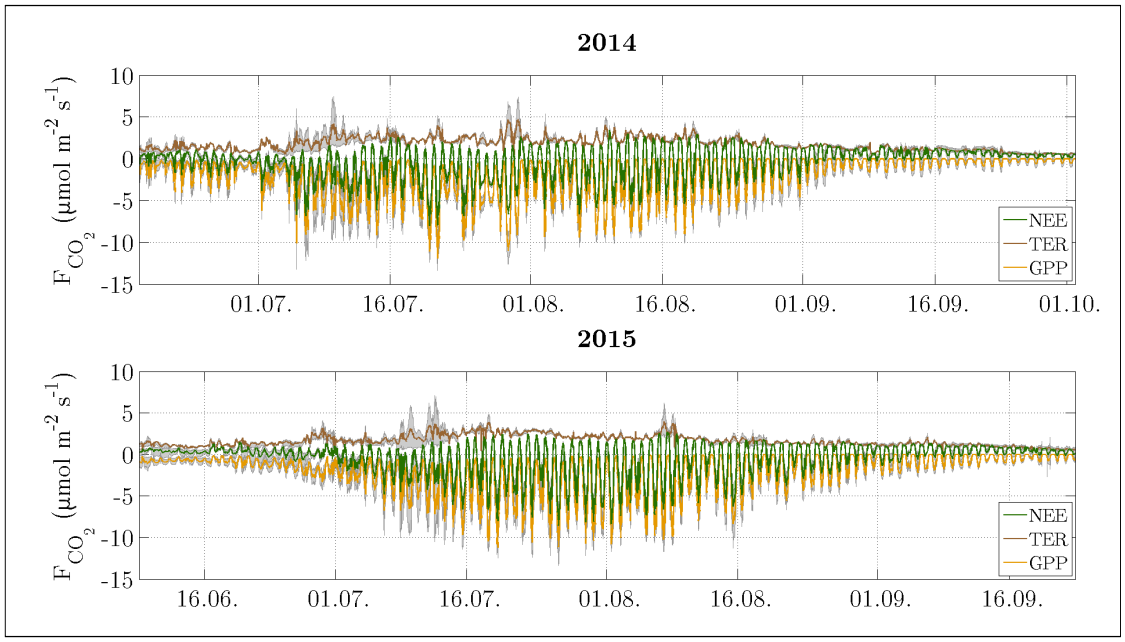

Figure 21 Time series of modelled NEE and its components TER and GPP with 95 % confidence intervals. This decomposition did not consider vegetation classes.

fluxes in 2014 began to display negative fluxes earlier than in 2015 indicating a sooner start of the growing season. However, the generally higher temperatures in 2014 caused on balance distinctly more positive fluxes than in 2015 suggesting differences in source strength between both years.

3.3. Model performances and budgets

3.3.1. Methane flux

The mechanistic model (MM) was able to reproduce the time series of the observed methane fluxes; although the extrema of the fluctuations were often missed, the general flux dynamics were captured (Figure 17). This manifests in an adjusted coefficient of determination (R^2_{adj}) of 0.63 for 2014 and 0.71 for 2015, if calibration and test data derive from the same year (Table 1). Invoking mean absolute errors (MAE) of 0.0033 µmol m^{-2} s^{-1} and 0.0029 µmol m^{-2} s^{-1} as well as mean fluxes of 0.011 µmol m^{-2} s^{-1} and 0.012 µmol m^{-2} s^{-1} yielded mean relative errors of 30.6 % and 23.4 % for 2014 and 2015, respectively. The root mean square errors (RMSE) amounted to 0.0045 µmol m^{-2} s^{-1} for 2014 and 0.0036 µmol m^{-2} s^{-1} for 2015.

The major success of this model was due to the application of vegetation class-specific weighting. Running a simple model without three Ω, but with one T_{soil} at a depth of 30 cm and one u* only yielded an R^2_{adj} of 0.12 for 2014 and 0.33 for 2015. Furthermore, friction velocity generated only little explanatory power; running the MM without the u* terms resulted in R^2_{adj} being 0.59 and 0.7 for 2014 and 2015, respectively.

The stepwise regression model (SR) performed as well as the MM in 2014, but slightly worse in 2015. Allocating coefficients to the input variables and testing their significance required 6 steps. The neural network (NN) performed considerably better than the MM and the SR in both years. The hidden layer size, i.e. the amount of neurons in the hidden layer, is adjustable and was found to yield a good R^2_{adj}, when set to 5. On average, adjusting the weights terminated after 25 epochs.

In the test for predictive power, all model performances expectedly dropped as a result of the discrepancy of the estimated fitting coefficients between 2014 and 2015 (Table 2). However, these declines varied in magnitude (Table 1). When running the models with both 2015 calibration data and 2014 test data (validation run 1), the R^2_{adj} values and the error metrics (MAE and RMSE) were of similar magnitude, but the extent of reduction in model performance was larger in NN than in MM and SR. While the R^2_{adj} of NN decreased three times more than the R^2_{adj} values of MM and SR, the error metrics of NN increased 1.5 times

Table 1 Model performances of mechanistic model (MM), stepwise regression (SR) and neural network (NN) for the measurement periods in 2014 and 2015. The light grey shaded cells refer to performances obtained, when the models were calibrated and driven with the same data. The cells with dark grey shading denote the two validation runs in the test for predictive power, where calibration and test data derived from different years (Figure 22). The units of mean error ME (average of residuals), mean absolute error MAE (average of absolute residuals) and root mean square error RMSE (standard deviation of residuals) are (µmol m^{-2} s^{-1}), and the adjusted coefficients of determination R^2_{adj} were significant ($P<0.001$) in all cases. While NN exhibited the best model performance, when calibration and test data derived from the same year, MM performed best in the test for predictive power.

Data & model	Calibrated with 2014 data			Calibrated with 2015 data		
	MM	SR	NN	MM	SR	NN
Tested with 2014 data	ME = 3.3E-4 MAE = 0.0033 RMSE = 0.0045 R^2_{adj} = 0.63	ME = -1E-17 MAE = 0.0034 RMSE = 0.0045 R^2_{adj} = 0.63	ME = -4.7E-5 MAE = 0.0029 RMSE = 0.0039 R^2_{adj} = 0.71	ME = 3.3E-3 MAE = 0.0043 RMSE = 0.0055 R^2_{adj} = 0.58	ME = 2.8E-3 MAE = 0.0045 RMSE = 0.0056 R^2_{adj} = 0.58	ME = 2.1E-3 MAE = 0.0044 RMSE = 0.0056 R^2_{adj} = 0.56
Tested with 2015 data	ME = -1.6E-3 MAE = 0.0036 RMSE = 0.0045 R^2_{adj} = 0.65	ME = -2.1E-3 MAE = 0.0038 RMSE = 0.0046 R^2_{adj} = 0.62	ME = -2.3E-3 MAE = 0.0039 RMSE = 0.0049 R^2_{adj} = 0.58	ME = 1.3E-5 MAE = 0.0029 RMSE = 0.0036 R^2_{adj} = 0.71	ME = 3E-18 MAE = 0.0031 RMSE = 0.0038 R^2_{adj} = 0.68	ME = 9.2E-6 MAE = 0.0023 RMSE = 0.0029 R^2_{adj} = 0.81

Table 2 Coefficients with 95 % confidence bounds that were plugged into equation 5 to compute methane fluxes with the mechanistic model for the measurement periods in 2014 and 2015. All estimates are significant except the "a_1" parameters ($P<0.05$).

Fitting parameters	2014	2015
a_1 (µmol m^{-2} s^{-1})	0.0005 ± 0.0005	0.0002 ± 0.0005
a_2 (µmol m^{-2} s^{-1})	0.0073 ± 0.0009	0.0088 ± 0.0009
a_3 (µmol m^{-2} s^{-1})	0.022 ± 0.006	0.019 ± 0.004
b_2 ($°C^{-1}$)	0.11 ± 0.02	0.18 ± 0.02
b_3 ($°C^{-1}$)	0.08 ± 0.03	0.12 ± 0.02
c ($m^{-1}s$)	0.98 ± 0.09	0.47 ± 0.09

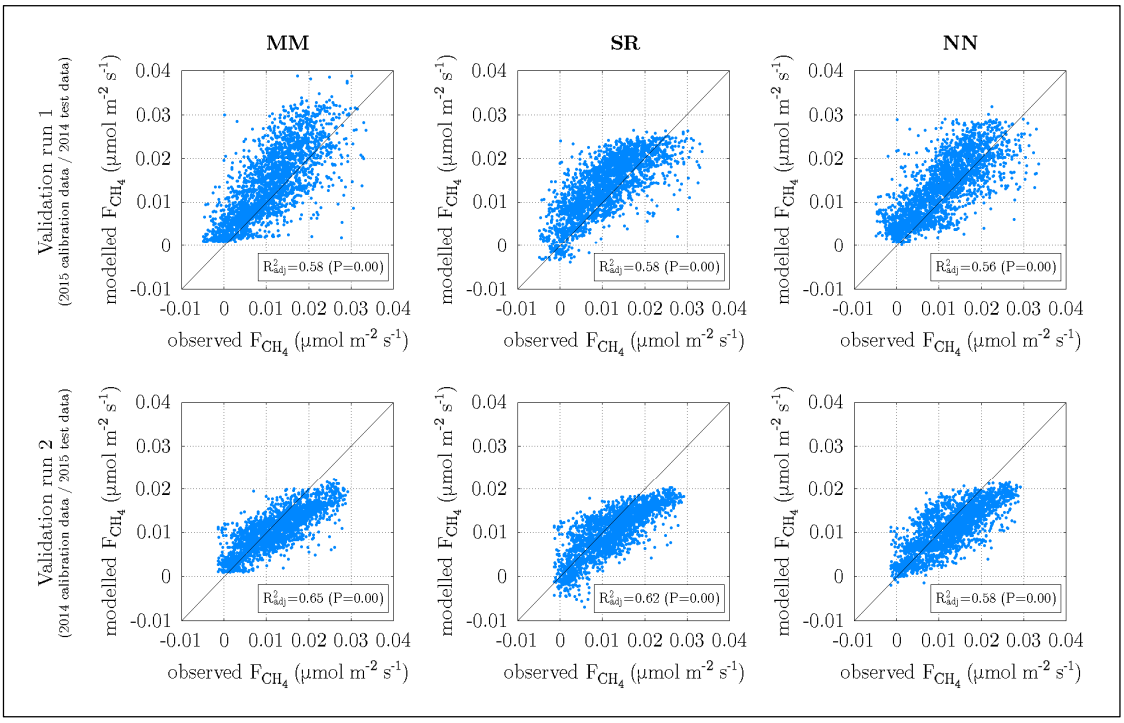

Figure 22 Outcome of the test for predictive power based on two validation runs for three different models: mechanistic model (MM), stepwise regression (SR) and neural network (NN). The adjusted coefficients of determination (R^2_{adj}) allow an objective evaluation (Table 1). In validation run 1, fluxes of the entire spectrum were distinctly overestimated, whereas large fluxes were underestimated in validation run 2. Furthermore, SR tended to produce smaller fluxes than MM and NN.

Table 3 Footprint budgets of methane emissions estimated with the mechanistic model (MM), stepwise regression (SR) and neural network (NN) for the measurement periods in 2014 and 2015. The budget estimation was carried out following two approaches: (i) standard filling of gaps in observed time series with modelled fluxes plus subsequent integration, and (ii) cumulating solely modelled time series (no gap-filling). For both approaches, the modelling of fluxes was carried out with calibration and test data from the same year (light grey shading) or from different years (dark grey shading), respectively. The error analysis was based on the root mean square error of the fit residuals for modelled fluxes while the errors of the observed fluxes were adopted from the initial flux computation. The subsequent error determination of the cumulative fluxes was conducted following standard error propagation techniques. All budgets are given in (mmol m^{-2}), and the gaps filled by the models constituted roughly half of the time series. Since all models yield similar budgets, when calibration and test data are derived from the same year, the true cumulative methane emission can be assumed to be in the given range for each year.

Budget estimation	Calibration and test data	2014			2015		
		MM	SR	NN	MM	SR	NN
Gap-filled data	Same year	96.1 ± 0.5	94.1 ± 0.5	95.3 ± 0.4	104.3 ± 0.4	104.2 ± 0.4	102.6 ± 0.3
	Different years	111.3 ± 1.2	107.2 ± 1.2	106.9 ± 1.2	94.7 ± 1.7	93.9 ± 1.7	92.1 ± 1.6
Only modelled data	Same year	97.6 ± 0.6	94.1 ± 0.6	95.2 ± 0.5	104.4 ± 0.5	104.2 ± 0.5	102.6 ± 0.4
	Different years	123.8 ± 1.6	117.7 ± 1.6	117.5 ± 1.6	87.3 ± 2.3	86.7 ± 2.2	84.2 ± 2.1

more than the error metrics of MM and SR. Running the models with both 2014 calibration data and 2015 test data (validation run 2) caused a performance reduction in both MM and SR, whose extent was slightly lower than in the previous validation run. Again, the reduction in R^2_{adj} was largest in NN, being almost four-fold greater than the reduction in R^2_{adj} values of MM and SR. Also, the growth in the error metrics of NN was more than two times the growth in the error metrics of MM and SR. For each validation run, the new model performances differed from each other inasmuch that MM exhibited the best performance, which was closely followed by SR, both performing distinctly better than NN. While all models overestimated the observed methane fluxes in validation run 1, they tended to underestimate the larger fluxes in validation run 2 (Figure 22). Also, the scatter in validation run 1 was larger than in validation run 2.

The footprint budgets, obtained through gap-filling observed time series with the three models, were similar, when calibration and test data originated from the same year (Table 3). Very similar budgets were obtained, when solely modelled fluxes were considered, i.e. no gap-filling was conducted, with a mean deviation of around 0.3 %. The mean error served as a direct indicator of the deviation between these fully modelled budgets and gap-filled budgets (Table 1). The budgets, obtained when calibration and test data derived from different years, exhibited a clear deviation from the budgets described above. The mean deviation amounted to roughly 11 %, when gap-filling was conducted, and about 21 %, when budget estimation was based on modelled fluxes only. Furthermore, these budgets were too large in 2014 and too little in 2015 compared to budgets, obtained when calibration and test data originated from the same year (Figure 22). Among the three models, there were no distinct divergences between the estimated budgets, when employing different calibrations and estimation approaches.

3.3.2. Carbon dioxide flux

The model, which fits a vegetation class-specific temperature response and light curve, was able to reproduce the observed fluxes very well (Figure 20). This is expressed by an R^2_{adj} of 0.88 for 2014 and 0.95 for 2015 (Figure 23).

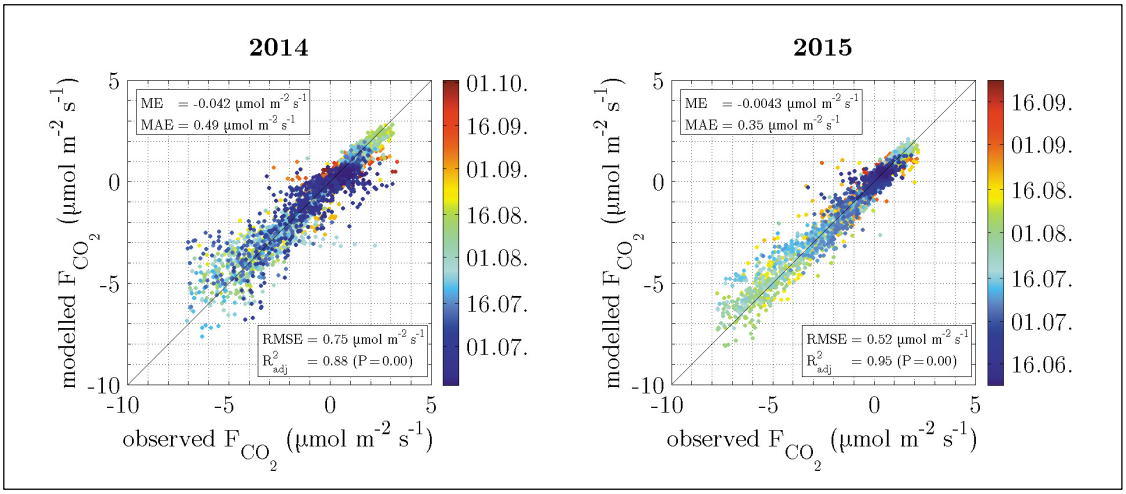

Figure 23 Model performances illustrated by scatter plots and the following error measures: mean error ME (average of residuals), mean absolute error MAE (average of absolute residuals), root mean square error RMSE (standard deviation of residuals) and the adjusted coefficient of determination R^2_{adj} (proportion of explained variability adjusted for the number of both predictor variables and data points). On account of the tight linking between the carbon dioxide flux and its governing variables PPFD and temperature, a very high model performance could be achieved.

Furthermore, the mean absolute error (MAE) amounted to 0.49 µmol m^{-2} s^{-1} and 0.35 µmol m^{-2} s^{-1} for 2014 and 2015, respectively. The model performed best during the growing season and less good during the shoulder seasons, where autumn displayed a slightly better performance than spring.

The consideration of the heterogeneous footprint, as conducted with the model given in equation 10, improved the model performance to only a little extent. Computing fluxes with the model given in equation 9, which does not include information on vegetation classes, yielded the following performance measures for 2014 and 2015, respectively: an R^2_{adj} of 0.82 and 0.93 as well as an MAE of 0.59 µmol m^{-2} s^{-1} and 0.39 µmol m^{-2} s^{-1}. This slightly inferior model performance was in conjunction with a shorter fitting procedure: all fitting parameters could be estimated significantly with 3 model steps.

The four model steps yielded the following interim results: the Q_{10} values were fixed at 1.42 for vegetation class 1 and at 1.48 for vegetation class 2 & 3 (Figure 24). The temporal evolution of α values could be well approximated with replacement functions (Figure 25). The interval, spanned around these functions by means of threshold functions, incorporated proper α values, whereas inappropriate α values were identified outside of the interval. In contrast to the replacement functions of α, which needed to be created for both vegetation classes in both years, a replacement function for P_{max} needed to be created only for vegetation class 1 in 2015 and for vegetation class 2 & 3 in 2014 (Figure 26). Similarly, there was more variability in vegetation class 2 & 3 than in vegetation class 1.

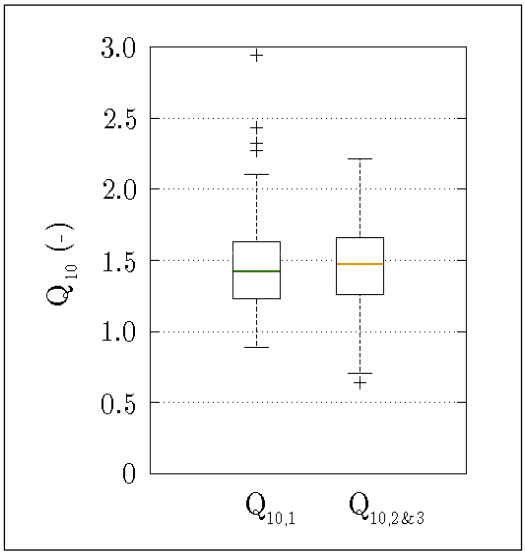

Figure 24 Outcome of the first model step: determining Q_{10} values for vegetation class 1 ($Q_{10,1}$) and vegetation class 2 & 3 ($Q_{10,2\&3}$), respectively. The values in consideration were associated with a minimum R^2_{adj} of 0.75 and significant ($P<0.05$). While the central mark in each box denotes the median that was utilised as a representative value for each vegetation class, the bottom and top edges indicate the 25th and 75th percentiles, respectively. The whiskers extend to the most extreme data points excluding outliers, which are illustrated outside the whiskers. Q_{10} of the bushy vegetation class was somewhat lower than the Q_{10} of the vegetation class dominated by sedges.

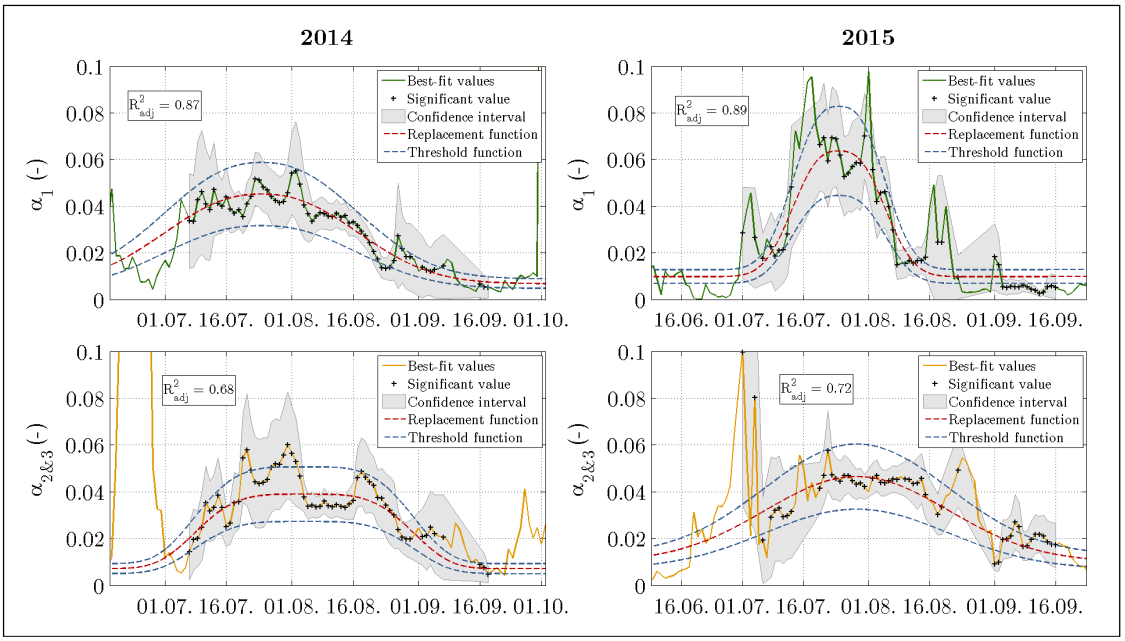

Figure 25 Outcome of the second model step: creating a replacement function for vegetation class 1 (α_1) and vegetation class 2 & 3 ($\alpha_{2\&3}$), respectively, by fitting a Gaussian curve to significant best-fit values. The R^2_{adj} displays the goodness of fit of the replacement functions. The interval spanned by two threshold functions separated meaningful α values from spurious α values such as the large springtime peaks with vegetation class 2 & 3.

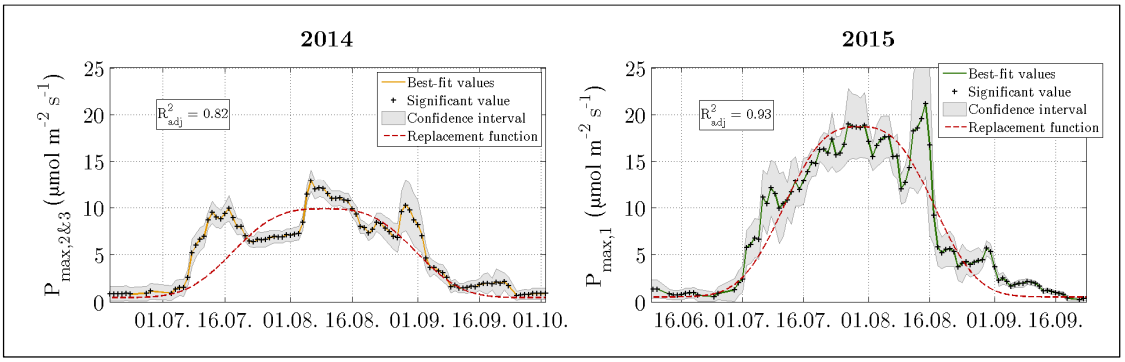

Figure 26 Outcome of the third model step: creating a replacement function for vegetation class 1 ($P_{max,1}$) and vegetation class 2 & 3 ($P_{max,2\&3}$), respectively, by fitting a Gaussian curve to significant best-fit values. The R^2_{adj} displays the goodness of fit of the replacement functions. In the measurement period 2014, a replacement function was necessary only for vegetation class 2 & 3, whereas a replacement function was necessary only for vegetation class 1 in the measurement period 2015. In the two remaining cases, all fitting parameters could be estimated significantly during the preceding model steps.

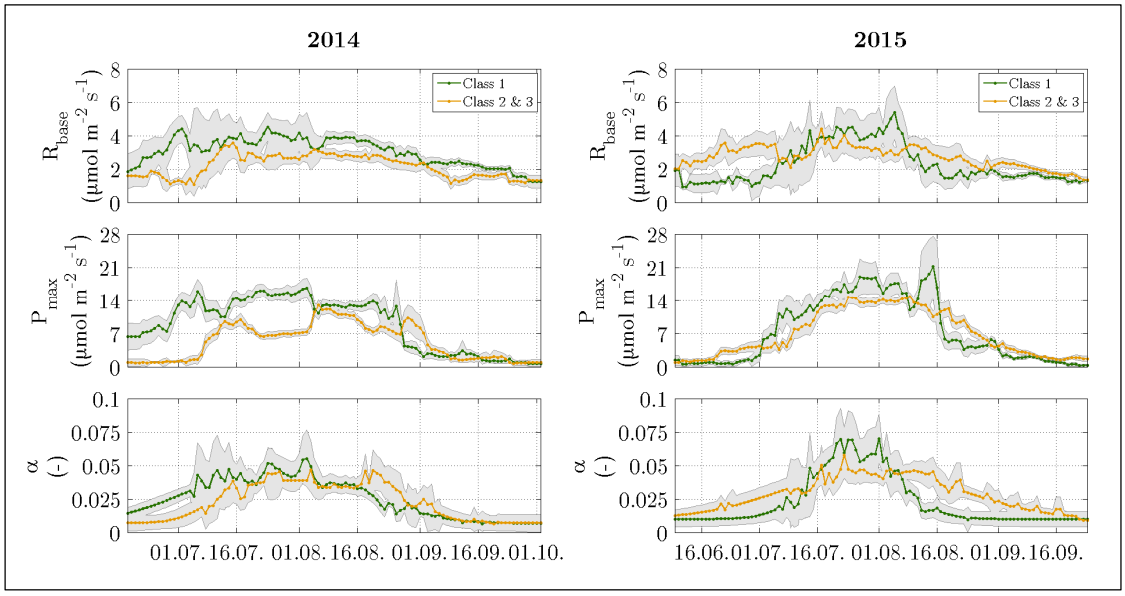

Figure 27 Comparison of fitting parameters of the two vegetation classes for each measurement period. P_{max} exhibited most of the significant differences, whereas α presented the fewest significant differences between both vegetation classes.

Besides Q_{10}, which was held constant during a measurement period, the fitting parameters R_{base}, P_{max} and α displayed a seasonal course for each vegetation class in 2014 and 2015 (Figure 28 and Figure 29). This course, characterised by larger values during the growing season and lower values during the shoulder seasons, was generally more pronounced in 2015 than in 2014. The application of replacement functions for α values obviously reduced the noise in the seasonal courses of α, but also in the seasonal courses of both R_{base} and P_{max}. In general, the 3-3-p model parameterisation was utilised at roughly 49 % of modelled days, the 3-2-p/2-3-p/2-2-p parameterisations at about 47 %, and the 2-1-p/1-2-p parameterisations at around 4 %. R_{base} was the fitting parameter that could be estimated most confidently as this parameter accounted for 19 % of the insignificances during the fitting procedure in 2014 and 2015. While P_{max} caused 31 % of the insignificances, α appeared to be the least certain fitting parameter representing the remaining 50 %.

The comparison of fitting parameter dynamics revealed that P_{max} displayed most of the significant differences while α exhibited the fewest significant differences between both vegetation classes (Figure 27). In 2014, the curves followed a rather flat course, and vegetation class 1 was mostly greater in magnitude as well as temporally ahead of vegetation class 2 & 3 so that the largest significant differences occurred in spring 2014. In 2015, the curves exhibited a bell-shaped course, where vegetation class 1 was greater in magnitude

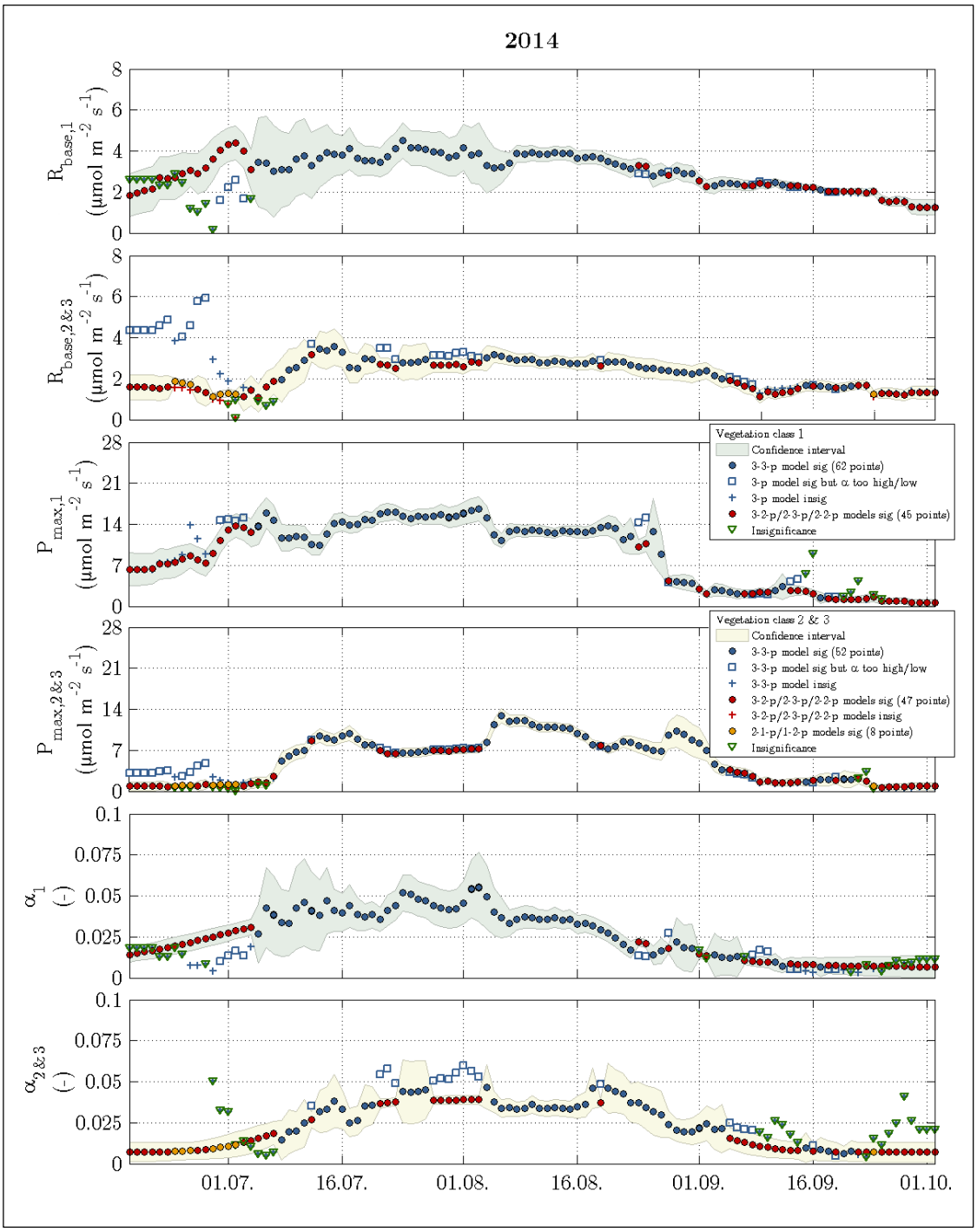

Figure 28 Time series of fitting parameters in 2014 for vegetation class 1 (index 1 and green confidence intervals) and vegetation class 2 & 3 (index 2 & 3 and yellow confidence intervals). The circles represent significant fits yielding 107 data points per parameter. The respective reasons for reparameterisation such as inappropriate values or insignificances are signified by squares and plus signs. The triangles denote the individual parameter, which caused a refit in the corresponding vegetation class.

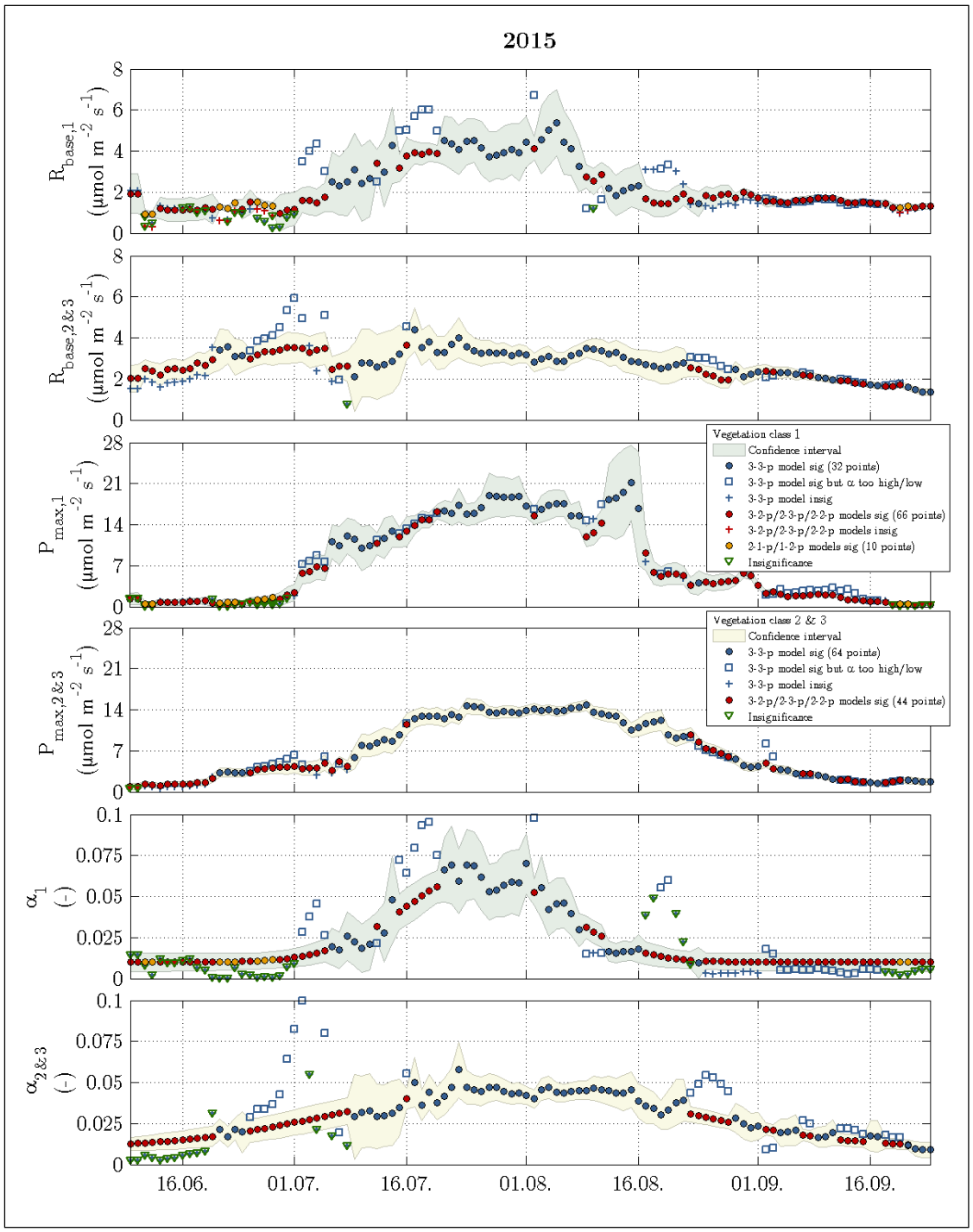

Figure 29 Time series of fitting parameters in 2015 for vegetation class 1 (index 1 and green confidence intervals) and vegetation class 2 & 3 (index 2 & 3 and yellow confidence intervals). The circles represent significant fits yielding 108 data points per parameter. The respective reasons for reparameterisation such as inappropriate values or insignificances are signified by squares and plus signs. The triangles denote the individual parameter, which caused a refit in the corresponding vegetation class.

during the summer and vegetation class 2 & 3 was greater in magnitude during spring and autumn while the peaks of both vegetation classes featured a similar timing.

The footprint budgets, obtained by gap-filling the observed flux time series (NEE) amounted to -3.81 ± 0.06 mol m^{-2} for the measurement period 2014 and -5.27 ± 0.06 mol m^{-2} for the measurement period 2015. When solely modelled fluxes were utilised, i.e. no gap-filling was carried out, the following budgets were estimated for the measurement periods: -4.02 ± 0.07 mol m^{-2} in 2014 and -5.29 ± 0.08 mol m^{-2} in 2015.

3.4. Downscaling and upscaling of fluxes

3.4.1. Methane flux

The downscaled methane fluxes were similar in magnitude for each vegetation class during both years (Table 4). Averaged over both years, the downscaled fluxes of vegetation class 1 ($F_{CH4,1}$), 2 ($F_{CH4,2}$) and 3 ($F_{CH4,3}$) amounted to 0.0004 µmol m^{-2} s^{-1}, 0.018 µmol m^{-2} s^{-1} and 0.052 µmol m^{-2} s^{-1}, respectively. While $F_{CH4,1}$ remained at a constant magnitude close to zero, $F_{CH4,2}$ and $F_{CH4,3}$ exhibited a

Table 4 Outcome of downscaling and upscaling of methane fluxes for the comparison period in both 2014 and 2015: the mean, downscaled fluxes (± standard deviation) refer to the individual methane fluxes (Figure 18); when gap-filled and summed up they yield the integrated, downscaled fluxes (± 95 % confidence bounds), and when projected on the respective areas they in turn return the upscaled fluxes (± combination of cumulative flux error and classification error).

Vegetation tion-class	Area on flood plain (m^2)	Classification uncertainty (%)	Mean downscaled F_{CH4} (µmol m^{-2} s^{-1})		Cumulative downscaled F_{CH4} (mmol m^{-2})		Upscaled F_{CH4} (kmol)	
			2014	2015	2014	2015	2014	2015
1	251891	19.1	0.0005	0.0002	4.2 ± 0.1	1.4 ± 0.1	1.1 ± 0.2	0.4 ± 0.1
2	611154	23.5	0.017 ± 0.004	0.019 ± 0.005	139.8 ± 0.6	167.2 ± 0.6	85.5 ± 20.1	102.2 ± 24.1
3	183911	31.5	0.056 ± 0.014	0.048 ± 0.012	455.1 ± 4.3	401.8 ± 2.9	83.7 ± 26.4	73.9 ± 23.3

seasonal course, where $F_{CH4,3}$ displayed more variability than $F_{CH4,2}$ (Figure 18). All of the three flux time series were significantly different from each other ($P<0.05$).

The upscaling revealed that on average $F_{CH4,2}$ accounted for slightly more than half of the flood plain's methane emission while this vegetation class covers roughly 58 % of the flood plain (Table 4). Nearly half of the flood plain's emissions were on average to be attributed to $F_{CH4,3}$, although this vegetation class stretches only over 18 %. The very low emissions of vegetation class 1 originate from 24 % of the flood plain's area.

The methane emission of the entire flood plain amounted to 0.171 ± 0.033 Mmol and 0.177 ± 0.034 Mmol for the comparison period 18th June to 24th September in 2014 and 2015, respectively (Table 5). The uncertainties associated with these estimates result

Table 5 Final carbon budgets of the entire flood plain estimated for the comparison period in both 2014 and 2015. The budgets were obtained by (i) downscaling the observed footprint fluxes into fluxes, which account for classes with uniform vegetation, (ii) upscaling these decomposed fluxes depending on the spatial extent of the respective vegetation class, (iii) superimposing these vegetation class-specific fluxes for F_{CH4} and F_{CO2}, respectively, and (iv) cumulating these net carbon fluxes (Figure 33). The errors of the budgets were computed following standard error propagation routines. For the comparison of F_{CH4} and F_{CO2}, the methane budgets were converted to CO_2 equivalents utilising two concepts: the global warming potential (GWP) and the global temperature change potential (GTP), both were based on a time horizon of 100 years including climate carbon feedbacks. At last, roughly 42 % (GWP) or 13 % (GTP) of the carbon dioxide budget was offset by the methane budget.

Conversion concept	F_{CH4} (Mmol CH_4)		CO_2 equivalent of F_{CH4} (Mmol CO_2 eq)		F_{CO2} (Mmol CO_2)		Total (Mmol CO_2 eq)	
	2014	2015	2014	2015	2014	2015	2014	2015
Global warming potential	0.171 ± 0.033	0.177 ± 0.034	2.11 ± 0.41	2.18 ± 0.41	-4.42 ± 0.49	-6.17 ± 0.66	-2.31 ± 0.64	-3.98 ± 0.78
Global temperature potential	0.171 ± 0.033	0.177 ± 0.034	0.68 ± 0.13	0.71 ± 0.13	-4.42 ± 0.49	-6.17 ± 0.66	-3.74 ± 0.51	-5.46 ± 0.67

from standard error propagation routines involving both cumulative flux error and classification error, the latter being one order of magnitude larger than the former (Table 4). Dividing these estimates by the area of the flood plain yielded mean flood plain budgets of 0.163 ± 0.032 mol m^{-2} and 0.169 ± 0.032 mol m^{-2} for the comparison period in 2014 and 2015, respectively (Table 6).

The methane budgets estimated by the eddy covariance system on the river terrace for the same comparison periods were as follows (Table 6): 0.096 ± 0.001 mol m^{-2} in 2014 and 0.099 ± 0.001 mol m^{-2} in 2015 (Wille, C., personal communication, 2018). The necessary gap-filling was carried out by means of linear interpolation, a routine that has also been applied for this purpose at other sites (Rinne et al., 2007; Tagesson et al., 2012). This simple

Table 6 Comparison between flood plain and river terrace in terms of their sink/source strength for the comparison period in both 2014 and 2015. For an appropriate comparison between both sites, the budgets of the flood plain possess an areal reference obtained by rescaling the robust budgets of the entire flood plain in Table 5 with the aid of the flood plain area size (1 046 956 m^2). The entire scaling procedure, which included the fairly large classification error, is the reason for the distinctly greater uncertainties of the flood plain budgets in comparison to the river terrace' footprint budgets, which did not undergo any scaling processes. For the consideration of the radiative efficiency of methane, GWP based on a time horizon of 100 years including climate carbon feedbacks was employed. In comparison to the flood plain, the polygonal tundra on the river terrace took up less carbon dioxide, but also released distinctly less methane resulting in a similar (2014) and weaker (2015) sink strength for greenhouse gases.

Geomorphological unit	F_{CH4} (mol CH_4 m^{-2})		CO_2 equivalent of F_{CH4} (mol CO_2 eq m^{-2})		F_{CO2} (mol CO_2 m^{-2})		Total (mol CO_2 eq m^{-2})	
	2014	2015	2014	2015	2014	2015	2014	2015
Flood plain	0.163 ± 0.032	0.169 ± 0.032	2.01 ± 0.39	2.08 ± 0.39	-4.22 ± 0.47	-5.89 ± 0.63	-2.21 ± 0.61	-3.81 ± 0.74
River terrace	0.096 ± 0.001	0.099 ± 0.001	1.18 ± 0.01	1.22 ± 0.01	-3.47 ± 0.03	-3.74 ± 0.03	-2.29 ± 0.03	-2.52 ± 0.03

type of gap-filling was assumed to be applicable due to favourable conditions such as, firstly, predominantly small gaps, secondly, the absence of a diurnal cycle and, thirdly and most importantly, the footprint's homogeneity on the mesoscale, i.e. the regular alternation of typical surface characteristics such as polygon centres and polygon rims.

Lastly, estimating flood plain budgets by simply projecting footprint budgets (calculated with MM) on the entire flood plain yielded budgets that are on average roughly 42 % lower than the adequately calculated flood plain budgets utilising the preceding flux decomposition (Table 7). This deviation was due to the sensor location bias: while the relative contribution of vegetation

Table 7 Deviation of greenhouse gas budgets estimated for the entire flood plain in the comparison period in both 2014 and 2015 by applying two different methods: (i) straightforward upscaling of the footprint budgets whilst ignoring their sensor location bias, and (ii) area-weighted upscaling of the beforehand downscaled footprint fluxes plus their subsequent summation in order to take the surface heterogeneity into account. The error calculation followed standard error propagation routines: in (i), a conservative error of 5 % was arbitrarily laid down for the determination of the flood plain area size with a geographic information system, and in (ii), the classification errors in Table 4 were adopted. Both estimation methods yielded different greenhouse gas balances, where their deviations were predominantly caused by a discrepancy in the methane budgets rather than in the carbon dioxide budgets. The conversion concept for the methane emissions was the global warming potential.

Estimation method	F_{CH4} (Mmol CH_4)		F_{CO2} (Mmol CO_2)		Total (Mmol CO_2 eq)	
	2014	2015	2014	2015	2014	2015
(i) Straightforward upscaling	0.096 ± 0.005	0.104 ± 0.005	-4.32 ± 0.22	-5.87 ± 0.29	-3.13 ± 0.23	-4.58 ± 0.29
(ii) Upscaling with preceding downscaling	0.171 ± 0.033	0.177 ± 0.034	-4.42 ± 0.49	-6.17 ± 0.66	-2.31 ± 0.64	-3.98 ± 0.78
Deviation between both methods	0.074 (43 %)	0.072 (41 %)	-0.11 (2 %)	-0.31 (5 %)	0.82 (35 %)	0.61 (15 %)

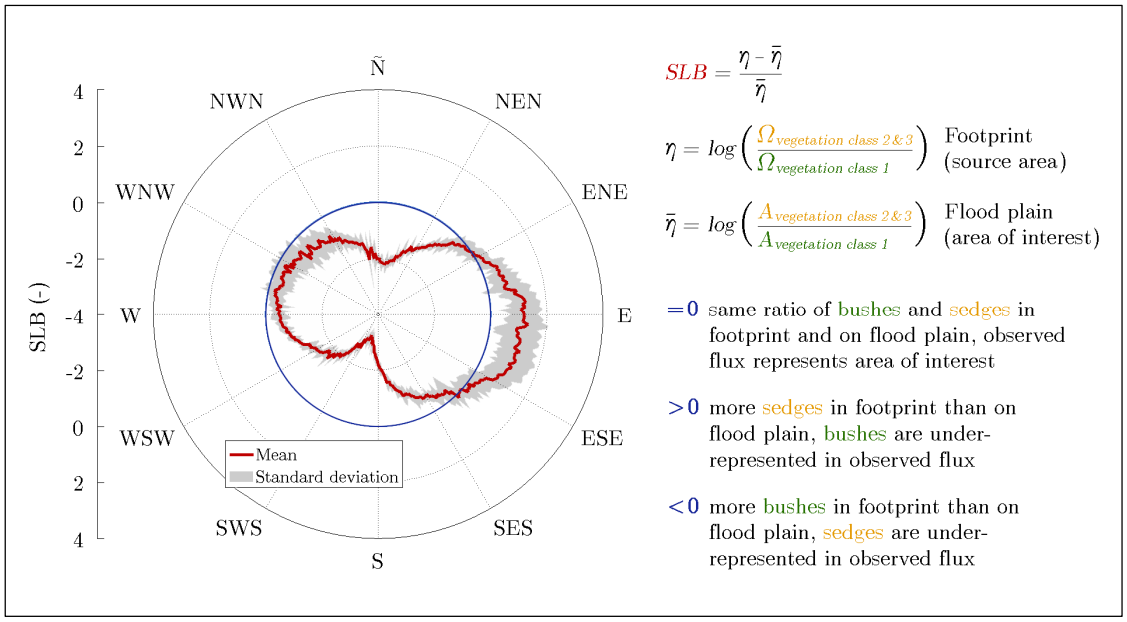

Figure 30 Wind direction dependency of the sensor location bias (SLB), a measure for the representativeness of observed fluxes in a footprint (modified from Schmid and Lloyd, 1999). The applied logarithms aided visual clarity, and data basis included both measurement periods 2014 and 2015. When the wind came from easterly directions, the flux tower sampled too much in vegetation class 2 & 3, whereas vegetation class 1 contributed too much to the flux signal during the other wind directions with two exceptions: with an upwind area to the north-east or south-west, the sensed source area in the footprint was representative for the vegetation composition in the area of interest, i.e. the entire flood plain. The implication of the SLB declines, the less pronounced the discrepancy between the vegetation class-specific flux magnitudes: the SLB was essential to consider for F_{CH4}, whereas for F_{CO2} it mostly played a tangential role.

class 1 in the footprint was generally larger than spread on the flood plain, vegetation classes 2 and 3 were proportionally more abundant on the flood plain than in the footprint (Figure 30).

3.4.2. Carbon dioxide flux

At first, the observed NEE was partitioned into its components TER and GPP (Figure 21). While NEE permanently alternated between uptake and release, TER was always positive, whereas GPP was always zero or negative except most spring nights, when GPP did not drop down to zero due to the bright nights of polar day. The budgets of NEE, TER, GPP account for the entire footprint and were as follows: -4.35 mol m^{-2}, 15.51 mol m^{-2}, -19.86 mol m^{-2} for the comparison period in 2014 and -5.61 mol m^{-2}, 14.38 mol m^{-2}, -19.99 mol m^{-2} for the comparison period in 2015, respectively.

In addition to the partitioned footprint fluxes, the observed NEE was downscaled into two NEE plus their respective component fluxes accounting for both vegetation classes (Table 8). In this process, hidden differences in sink strength between both vegetation classes could be unveiled (Figure 31). Most notably, NEE of vegetation class 1 was considerably greater in magnitude (more negative) in the first half of the growing season in 2014, whereas NEE of vegetation class 2 & 3 was slightly greater in the second half. This ratio was determined by GPP exhibiting the same dynamics while TER of vegetation class 1 was greater than TER of vegetation class 2 & 3 throughout the growing season. In 2015, NEE of vegetation class 1 was somewhat greater in the first half of summer (July), whereas NEE of vegetation class 2 & 3 was marginally greater in the second half of summer (August), while during spring and autumn, the NEE of both vegetation classes were similar in magnitude. The flux dynamics of GPP and TER followed the course predefined by their respective fitting parameters, i.e. they were greater for vegetation class 1 during the peak of the growing season (late July), whereas they were greater for vegetation class 2 & 3 at the start and end of the growing season (Figure 27).

Estimating budgets of the downscaled fluxes revealed that the sink strength of vegetation class 1 was substantially larger than the sink strength of vegetation class 2 & 3 in 2014, which was more due to differences in GPP between both vegetation classes than differences in TER (Table 8). In 2015, the sink strengths of both vegetation classes were similar. The cumulative curves indicate the cause for this interannual variability: higher temperatures, particularly in late July, in conjunction with higher PPFD in 2014 (Figure 32).

The carbon dioxide net uptake of the entire flood plain amounted to -4.42 ± 0.49 Mmol and -6.17 ± 0.66 Mmol for the comparison period 18th June to 24th September in 2014 and 2015, respectively (Table 5). The uncertainties associated with these estimates were obtained by means of standard error propagation techniques including both cumulative flux error and classification error, where the former was one magnitude lower than the latter (Table 4). Dividing these budgets by the total area of the flood plain yielded mean flood plain budgets of -4.22 ± 0.47 mol m^{-2} and -5.89 ± 0.63 mol m^{-2} for the comparison period in 2014 and 2015, respectively (Table 6).

The carbon dioxide budgets estimated by the eddy covariance system on the river terrace for the same comparison periods were as follows (Table 6): -3.47 ± 0.03 mol m^{-2} in 2014 and -3.74 ± 0.03 mol m^{-2} in 2015 (Wille, C., personal communication, 2018). The obligatory gap-filling was carried out utilising a model that resembles the model employed for the flood plain; differences include an absent flux decomposition and 3 instead of 4 model steps.

Table 8 Outcome of downscaling and upscaling of carbon dioxide fluxes for the comparison period in both 2014 and 2015: the mean, downscaled fluxes (± standard deviation) refer to the individual carbon dioxide fluxes (Figure 31); when gap-filled and summed up they yield the integrated, downscaled fluxes (± 95 % confidence bounds), and when projected on the respective areas they in turn return the upscaled fluxes (± combination of cumulative flux error and classification error).

Vegetation class	Mean downscaled F_{CO2} (μmol m^{-2} s^{-1})						Cumulative downscaled F_{CO2} (mol m^{-2})						Upscaled F_{CO2} (Mmol)					
	2014			2015			2014			2015			2014			2015		
	NEE	TER	GPP	NEE	TER	GPP	NEE	TER	GPP	NEE	TER	GPP	NEE	TER	GPP	NEE	TER	GPP
1	-0.89 ± 2.86	2.62 ± 0.84	-3.51 ± 3.32	-0.71 ± 2.51	1.87 ± 0.99	-2.58 ± 3.11	-7.51 ± 0.11	22.06 ± 0.08	-29.56 ± 0.15	-5.98 ± 0.11	15.73 ± 0.06	-21.71 ± 0.15	-1.89 ± 0.36	5.56 ± 1.06	-7.45 ± 1.42	-1.51 ± 0.29	3.96 ± 0.75	-5.47 ± 1.04
2 & 3	-0.38 ± 1.81	1.81 ± 0.71	-2.19 ± 2.21	-0.69 ± 2.32	2.11 ± 0.68	-2.81 ± 2.62	-3.19 ± 0.11	15.24 ± 0.08	-18.43 ± 0.15	-5.87 ± 0.11	17.74 ± 0.06	-23.61 ± 0.15	-2.53 ± 0.33	12.12 ± 1.55	-14.65 ± 1.87	-4.66 ± 0.59	14.11 ± 1.81	-18.77 ± 2.41

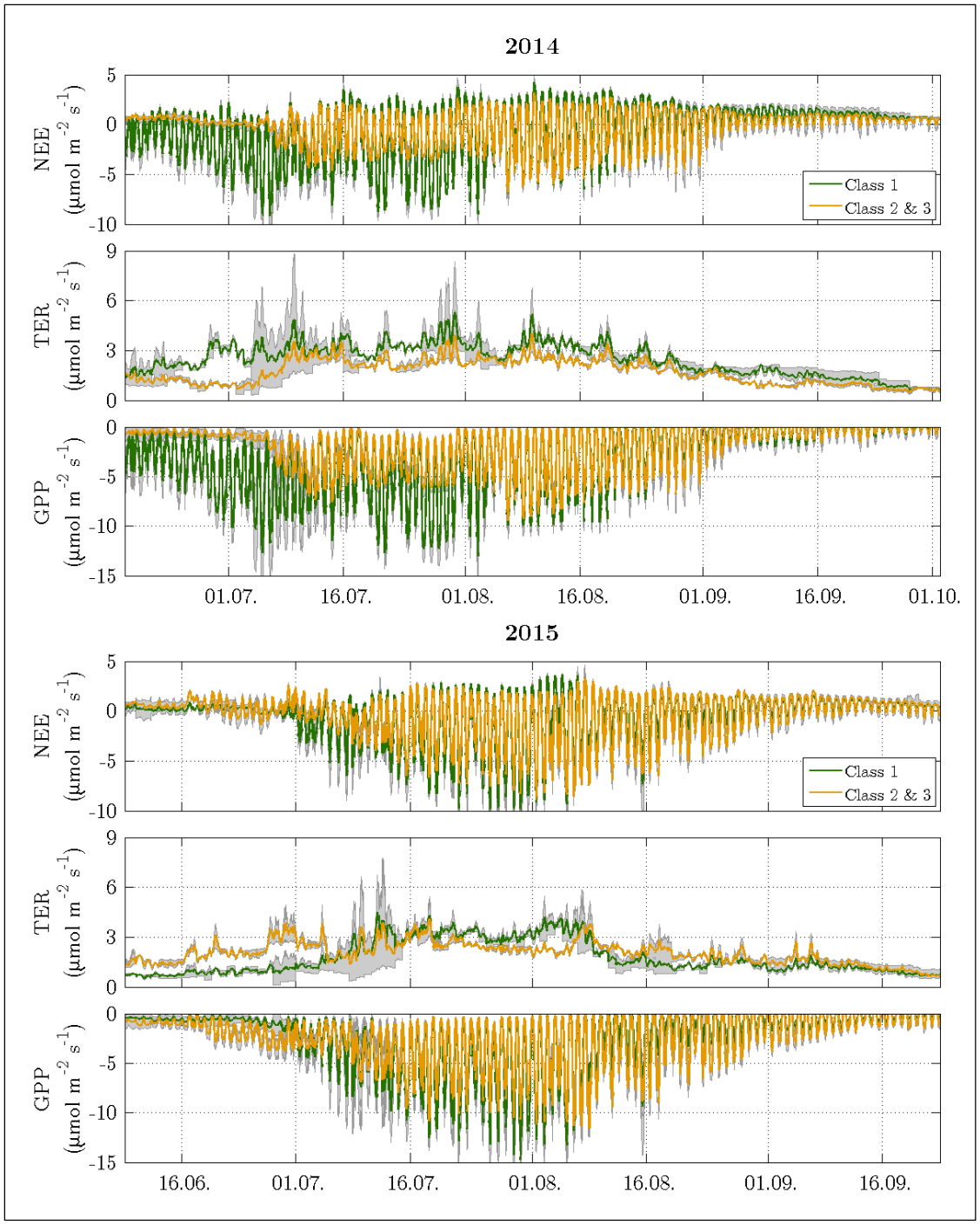

Figure 31 Time series of decomposed fluxes with 95 % confidence intervals accounting for the two vegetation classes of carbon dioxide flux modelling. The width of the confidence intervals varies depending on both the flux magnitude and the number of fitting parameters in the chosen model. The decomposition revealed a distinct difference in flux dynamics between both vegetation classes during the first half of the growing season in 2014.

At last, estimating flood plain budgets by simply upscaling the footprint budgets yielded budgets that were on average roughly 4 % lower (less negative) than the budgets obtained by upscaling the previously downscaled fluxes (Table 7). Consequently, the deviation between both carbon dioxide budgets estimated with the two different approaches was distinctly smaller than deviation between the likewise estimated methane budgets and, moreover, not significant. The reason was that the sink strengths of the individual vegetation classes were similar enough in order to form a representative footprint. This lacking sensor location bias for carbon dioxide fluxes was also indicated by the absent wind direction dependency.

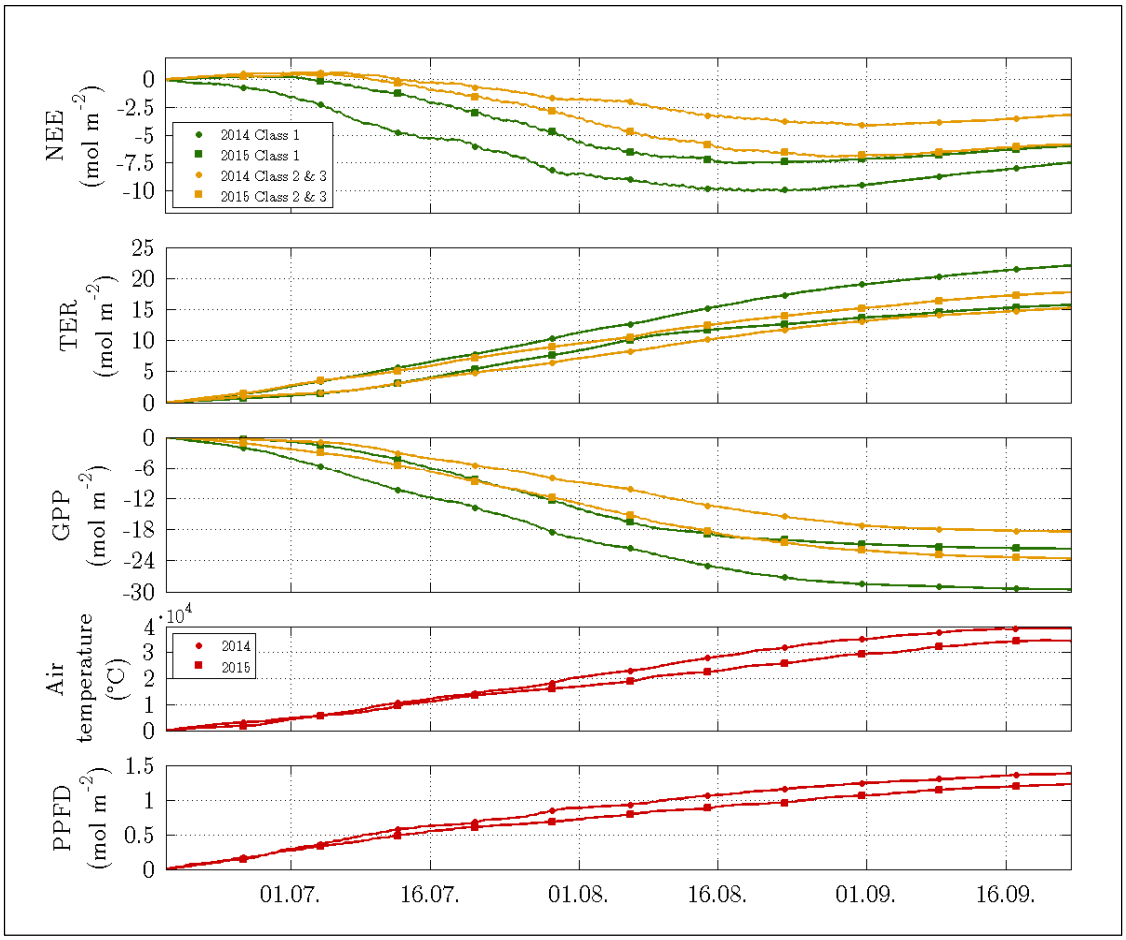

Figure 32 Cumulative curves for budget estimation of decomposed flux components (NEE, TER, GPP) and flux drivers (T_{air}, PPFD) for the comparison period in 2014 and 2015. While the carbon dioxide sink strengths of both vegetation classes did not differ during the climatologically usual year 2015, vegetation class 1 took substantially more carbon dioxide up than vegetation class 2 & 3 in the distinctively warmer year 2014.

3.4.3. Greenhouse gas flux

The evaluation of the flood plain's sink function depended on the chosen concept for converting methane budgets into carbon dioxide equivalents (Table 5). When GWP was applied, the methane emissions offset 47 % of the carbon dioxide net uptake in 2014 and 35 % in 2015. Accordingly, the greenhouse gas budgets specify that the flood plain formed a moderate sink in 2014 (-2.31 ± 0.64 Mmol CO_2 eq) and a stronger sink in 2015 (-3.98 ± 0.78 Mmol CO_2 eq). Alternatively, when GTP was utilised, the methane emissions cancelled out only 15 % and 12 % of the carbon dioxide net uptake in 2014 and 2015, respectively. Correspondingly, the flood plain constituted a stronger sink in 2014 (-3.74 ± 0.51 Mmol CO_2 eq) and a strong sink in 2015 (-5.46 ± 0.67 Mmol CO_2 eq).

Despite the minor percentage of the methane emission in the greenhouse gas exchange, the carbon dioxide net uptake was considerably compensated by the methane efflux due to its radiative efficiency, thereby lowering the sink strength of the flood plain substantially. The cause for the lower sink strength in 2014 could be attributed to the higher temperatures in 2014 adversely affecting the carbon dioxide uptake rather than the methane release (Figure 32). In the beginning of the comparison period, the cumulative carbon dioxide net uptake was larger in 2014 than in 2015, but after late July, the cumulative carbon dioxide net uptake in 2014 was distinctly lower (Figure 33). Judged by the steeper slopes of the cumulative carbon dioxide net uptake curves relative to the cumulative methane emission curves, F_{CO2} dominated the greenhouse gas exchange over F_{CH4} throughout the measurement period.

The comparison with the polygonal tundra on the nearby river terrace revealed that the flood plain was a weaker sink (Table 6). Even though the flood plain sequestered moderately more carbon dioxide, it also emitted distinctly more methane. On balance, the carbon in both gases methane and carbon dioxide respectively accounted on average for 8.5 % and 91.5 % of the total carbon in the greenhouse gas transport. On the river terrace, the corresponding percentages amounted to 6.9 % and 93.1 %. The underlying conversion concept in this comparison was the more conservative metric GWP. In order to enable an appropriate comparison despite the surface heterogeneity on the flood plain, their budgets were divided by the area of the flood plain yielding mean budgets with an areal reference. The footprint budgets obtained on the river terrace, however, were assumed representative. Due to the surface heterogeneity of the flood plain, i.e. the potentially unrepresentative vegetation class composition, the quantitative comparison of both sites' budgets remains restricted to Samoylov Island (and cannot be extended on the Lena River Delta).

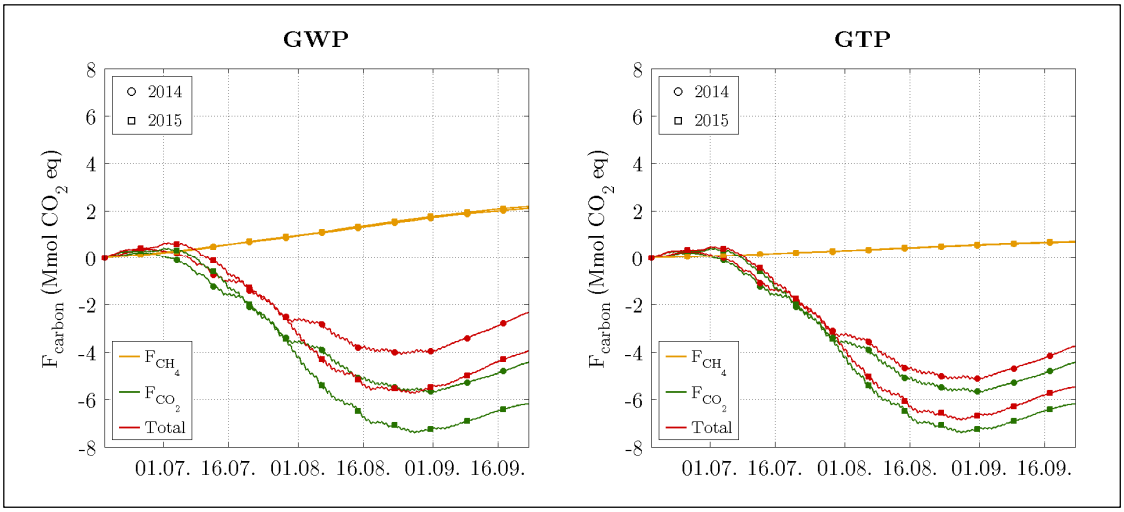

Figure 33 Cumulative curves of final carbon fluxes upscaled for the entire flood plain during the comparison period in 2014 and 2015. The conversion to CO_2 equivalents was based on both the global warming potential (GWP) and the global temperature change potential (GTP), both utilising a time horizon of 100 years including climate carbon feedbacks. Depending on the applied conversion concept, the flood plain was a moderate source of greenhouse gases in 2014 and weak sink in 2015 (GWP) or a strong sink in both years (GTP). Either way, the high temperatures in 2014 substantially mitigated the carbon sink function in comparison to the climatologically normal year 2015 (Table 5).

Finally, estimating budgets for the entire flood plain without the consideration of its surface heterogeneity led to substantially biased sink strengths (Table 7). When the footprint budgets of methane and carbon dioxide were simply projected on the entire flood plain, greenhouse gas budgets were obtained that overestimate the flood plain's sink strength by 0.82 Mmol CO_2 eq in 2014 and by 0.61 Mmol CO_2 eq in 2015 compared to the robust budgets obtained by the summed, area-weighted upscaling of the beforehand downscaled footprint fluxes. These substantial deviations were predominantly due to the divergence of the differently estimated methane budgets rather than the carbon dioxide budgets. This specification is substantiated by the budget's uncertainty intervals, which do not overlap for methane, but for carbon dioxide as well as for the final greenhouse gas balances.

4. Discussion

4.1. Interplay of flux and flux drivers

4.1.1. Methane flux

Identifying methane flux drivers has been an objective for many years and flux drivers are often site-specific. When it comes to wetlands, vegetation has been repeatedly demonstrated to be of major importance for methane emissions (Davidson et al., 2016; Grünfeld and Brix, 1999; Tsuyuzaki et al., 2001). Particularly vascular plants, such as sedges on the flood plain, provide a great deal of relevance since they form important pathways for methane transport by means of extensive air spaces (aerenchyma) in their vegetative organs (Schütz et al., 1991; Sebacher et al., 1985). Methane can diffuse through these cavities bypassing aerobic soil horizons without being oxidised. On the nearby river terrace, this plant plant-mediated methane transport was revealed to account for two thirds of the total methane flux at wet sites and somewhat less at moist sites (Kutzbach et al., 2004). Furthermore, vascular plants enhance the formation of methane by providing labile organic substances such as root exudates and root litter to the rhizosphere (Joabsson and Christensen, 2001).

Moist or wet patches, which provide favourable conditions for methane production, are often associated with abundant moss cover and thickness. However, mosses form a buffer for methane emissions by exhibiting a distinct oxidation potential (Liebner et al., 2011; Parmentier et al., 2011b). On the river terrace, up to 99 % of the produced methane was found to be oxidised through high methanotrophic activity in a layer of submerged moss (Knoblauch et al., 2015). Moreover, moss properties are strongly related to the active layer thickness. On account of their insolation capacity, they attenuate the heat input into the soil and, hence, diminish the thaw depth.

The active layer depth is also governed by the soil moisture via two counteracting thermal soil properties: thermal conductivity and heat capacity (Oke, 1987). The thermal conductivity is the

dominating property, when soil moisture is low, which enhances the downward transport of surface warmth leading to a greater thaw depth. When moisture is ample, the heat capacity is the dominating factor outweighing the thermal conductivity; therefore, the propagation of a temperature signal into the soil is increasingly mitigated resulting in a thin active layer, which offers a smaller soil volume where methanogenesis may occur. Since this relationship is dependent on soil texture, the thaw characteristics on the flood plain (mineral soil) and the river terrace (organic soil) are different (Zubrzycki et al., 2013). On the flood plain, an evident moisture dependency prevails, and the mean active layer depth can be estimated at 0.8 m, whereas on the river terrace, the soil thaws until roughly 0.5, and wet and dry sites exhibit similar active layer depths (Boike et al., 2013).

Capturing drivers such as moisture, moss properties and active layer depth in the heterogeneous footprint, the vegetation serves as an integrated proxy for the combined effect of these flux controls. The suitability of vegetation composition for predicting methane fluxes has also been reported for other ecosystem types such as riparian wetlands, temperate peatlands and boreal wetlands in in the zone of discontinuous permafrost (Audet et al., 2013; Bubier et al., 1995; Gray et al., 2013).

While the footprint information through vegetation class contributions provided crucial information on the (half-hourly) high-frequent portion of the flux signal, the soil temperatures held explanatory power to account for the (seasonal) low-frequent portion of the flux signal.

The utilised soil temperatures were measured in the top soil where the largest carbon turnover takes place due to both the highest organic matter quality and the greatest abundance of methanogenic communities in the soil profile (Wagner et al., 2007). In vegetation class 3, most of the methanogenic activity is likely to take place close to the surface (Liebner et al., 2008). Thus, the temperature at 10 cm depth was the most suitable temperature for capturing the temperature-induced variability in methane formation. In vegetation class 2 where oxic layers occurred, methanogens were located further down, and their emissions were on average more even due to the longer transport to the surface. Modelling their activity was hence best achieved utilising the soil temperature at 30 cm depth, whose variability is more attenuated.

4.1.2. Carbon dioxide flux

Air temperature and photosynthetically active photon flux density have numerously been employed for modelling carbon dioxide fluxes as both parameters dominate the set of determinants, which further include e.g. the availability of water, oxygen, nutrients.

In contrast to the large spatial variability of methane fluxes, the carbon dioxide fluxes did not exhibit a pronounced heterogeneity in the footprint. The reason lies in the fact that vegetation cover (biomass, physiology, productivity) and soil attributes (microbial community, organic substrate, nitrogen content) were not respectively disparate enough across the footprint to create distinctly diverse carbon dioxide flux dynamics. Hence, the reduction in the number of vegetation classes from 3 to 2 was necessary to capture the damped spatial variability.

4.2. Assessment of model performance

4.2.1. Methane flux

The better model performance in 2015 could be attributed to statistical reasons. Although both measurement periods were roughly the same length, there were distinctly more flux records in the 2014 dataset after the flux quality screening. Furthermore, there was significantly more variability in the high-frequent range of the flux time series in 2014 than in 2015 ($P<0.001$). Modelling more data points with more short-term variability is likely to be achieved at the expense of the model performance. Another site-related reason for the diverging model performances in 2014 and 2015 may have been the severe spring flood in 2014. The inundation of the entire flood plain for several days may have lastingly offset moisture and soil temperature-related differences between the three vegetation classes. Over the measurement period, when the footprint dried, pronounced methane emission-related characteristics then developed in each vegetation class. This temporal inconsistency in vegetation class characteristics has also likely compromised the model performance.

Comparing the model performances, the NN was superior to the other models. This result is in accordance with other studies reproducing half-hourly flux data (Aubinet et al., 1999; Moffat et al., 2007). This utility, however, was accomplished at the cost of generalisability as demonstrated in the test for predictive power. The SR and the NN are tools that are based on statistics and machine learning, respectively; they provide both a convenient handling and a widespread application. However, they may not find the theoretically best solution as the algorithm may settle in a local minimum instead of a global minimum on the error surface (Draper and Smith, 1998; Haykin, 1999). Another shortcoming of both SR and NN is the limited scope for changes in the algorithms, whereas the MM provides the possibility to elaborate and refine ecosystem-specific causal relationships. This advantage has decisively contributed to the result that the MM performed best in the test for predictive power. Hence, the MM is both less prone to overfitting, and reflects intrinsic ecosystem features, such as

the exponential soil temperature sensitivity, better than the other models. This result substantiates its applicability for flux decomposition.

Another advantage of the MM is the large range within it can be modified. This additive model provides a great deal of flexibility since the number of classes can be altered and class-specific flux drivers can be deployed. Furthermore, the classes do not necessarily need to be vegetation classes, when other surface characteristics appear to be dominating. However, driving the MM with moisture classes and thaw depth classes rather than vegetation classes did not yield better model fits. Moreover, the MM did not perform better by applying vegetation classes, whose contributions were obtained from the coarse, manually classified vegetation map instead of the classified orthomosaic. This emphasises both the utility of vegetation as a useful explanatory variable for methane fluxes and the importance of high-resolution information in a heterogeneous footprint.

4.2.2. Carbon dioxide flux

The high model performance can be attributed to the matching variabilities of both explanatory variables and explained variable, i.e. the diurnal cycle of PPFD, T_{air} and NEE. Another reason for the high model performance is the recalibration of the model for each day, which allowed a model adaption to the observed data that is much closer than e.g. calibrating the model only once for the entire measurement period as conducted for the methane fluxes. As with methane fluxes, the better model performance in 2015 was better than in 2014. This difference mainly originated through a reduced model performance in September 2014 while the performances of both years were similar during the remaining months. The reason for this difference is that the variability in observed fluxes was significantly greater in September 2014 than in September 2015 ($P<0.05$). Reproducing a greater variability with a given set of both flux samples and fitting parameters is likely to lead to a reduced model performance compared to explaining less variability with the same setting.

The minor deviation in performance, when modelling with either equation 9 or equation 10, is due to the predominantly absent wind direction dependency of carbon dioxide fluxes, i.e. the similar sink strengths of the individual fluxes. Furthermore, the shorter fitting procedure, which was associated with running the model given in equation 9, can be explained by a more favourable ratio of flux samples to fitting parameters.

The model procedure was outlined according to the features of the examined datasets. A further rearrangement of the model design could include a slower reduction of the applied fitting parameters; e.g. if a 2-3-p model fails to yield significant parameter estimates, then a

1-3-p model could be run next instead of 1-2-p model. Furthermore, similar to Q_{10}, a fixation of α for the growing season is conceivable as seasonal changes in α may be difficult to interpret.

4.3. Evaluation of flux decomposition

4.3.1. Methane flux

The downscaling of the eddy covariance (EC) flux yielded flux rates for each of the three vegetation classes (Figure 18). Their validation is based on unpublished closed chamber (CC) measurements, which were carried out in the respective vegetation classes east of the flux tower on the flood plain in autumn 2013 and spring 2014 (Runkle, B. and Sabrekov, A., personal communication, 2016). In the shrubby tundra of vegetation class 1, a mean methane flux with a standard deviation of -0.00005 ± 0.0002 μmol m^{-2} s^{-1} (n=10) was determined in early September and early June; n states the number of conducted measurements. This very low flux is likely to be under the noise limit and not relevant for estimating budgets; this assumption is justified by the modelled $F_{CH4,1}$ being negligible due to insignificant "a_1" parameters for both years (Table 2). CC measurements in the mixed vegetation class 2 yielded 0.011 ± 0.0091 μmol m^{-2} s^{-1} (n=11) in mid-June 2014. This period overlaps with EC measurements and the modelled $F_{CH4,2}$ was of the same magnitude at that time (Figure 18). In the graminoid tundra of vegetation class 3, CC measurements revealed a methane flux of 0.037 ± 0.0085 μmol m^{-2} s^{-1} (n=30) in mid-September 2013. This point in time is outside the EC measurement periods, but the modelled $F_{CH4,3}$ was also at this magnitude at that time of the year in 2014 and 2015. Also, fluxes around 0.02 μmol m^{-2} s^{-1} are considered to be at a plausible magnitude for $F_{CH4,2}$ as this vegetation class forms a combination of the two other vegetation classes, and $F_{CH4,2}$ lies well between the other two individual fluxes. Another indication of the plausibility of both $F_{CH4,2}$ and $F_{CH4,3}$ is the larger sensitivity to soil temperature changes of the latter, which confirms findings in a recent sensitivity study (Olefeldt et al., 2013); i.e. emissions of the wet vegetation class 3 were more sensitive to soil temperature variability than emissions of the drier vegetation class 2. This finding is based on "b" parameters that were obtained by running the model with soil temperatures at the same depth, once with 10 cm and once with 30 cm. These two additional model runs allowed a comparison, which revealed "b_3" being on average two times greater than "b_2". The accuracy of the decomposed fluxes can be assumed with confidence. However, the lack of regular CC measurements for a more comprehensive confirmation of the modelled vegetation class fluxes remains a weakness of this study.

The flux decomposition, as carried out in the present study for methane as

well as for carbon dioxide, has certain limitations. For example, uncertainty may be added by a potential inaccuracy in both surface classification and footprint model. While the former is deemed appropriate due to extensive ground truthing, the latter is difficult to assess. However, the employed footprint model is a widely applied tool within the flux community, and it constitutes a suitable model for this study site in a flat tundra landscape with low roughness lengths (Foken, T., personal communication, 2015). More importantly, the flux decomposition method may approach methodical limits, if the surface classes in the footprint are too uniformly distributed and/or their individual flux rates are too similar. Whether the assignment of flux rates from a mixed signal to individual surface classes is still possible under these circumstances may be an objective of further studies at other sites.

4.3.2. Carbon dioxide flux

The partitioning of carbon dioxide fluxes was conducted during the Arctic summer, when fully dark conditions during the nights are absent. Consequently, a partitioning approach that is based on fitting parameters to nighttime respiration followed by extrapolating these fits to daytime and subsequently subtracting the estimated daytime respiration flux from the observed net flux to obtain the photosynthesis flux is confronted with elevated uncertainties (Reichstein et al., 2005). The partitioning approach of the present study avoids this problem since the parameter fitting employs the entire dataset. However, the model may have a shortcoming in the small number of environmental driving parameters, which may oversimplify the actual physics. While the entire temperature sensitivity of NEE is manifested through changes in TER, the effect of temperature on the biochemical reactions in GPP is neglected (Haraguchi and Yamada, 2011). At the same time, no correlation between air temperature and model residuals (between observed and modelled NEE) could be detected, which indicates that the temperature-induced variability was sufficiently considered. The confounding effect of a high vapour pressure deficit (VPD), which tends to take place in the afternoon leading to a limited photosynthetic activity, was not taken into account (Lasslop et al., 2010). However, only very few days with low humidity (VPD>10 hPa) occurred, and the typically asymmetric diurnal cycle of NEE could not be found on these days. A missing linkage of the model with potential flux limitations through a low soil moisture is deemed appropriate given the ample moisture availability in the permafrost-affected soil at the study site (Gao et al., 2017; Minkkinen et al., 2018). The diverse effect of direct and indirect radiation on photosynthetic efficiency was also not taken into consideration (Williams et al., 2014). This effect plays a tangential

role for the low sedges, but adds uncertainty to the light-response curves calculated for the larger shrubs.

The flux decomposition yielded interesting insights into the flux dynamics of the two investigated vegetation classes (Figure 31). The validity of these dynamics and, hence, the reliability of the employed model is examined utilising four approaches.

Firstly, it has been demonstrated that the photosynthetic cycle of a canopy during a growing season is linked to its seasonal changes in greenness (Peichl et al., 2014; Sonnentag et al., 2012). The evolution of canopy greenness can be examined by determining the green chromatic coordinates (g_{cc}) of a target area in images obtained by digital repeat photography (Richardson, 2012). Employing the images from the time lapse camera on the flux tower, this method yielded g_{cc} values for vegetation class 1 with a central tendency that is significantly greater than the one of the g_{cc} values for vegetation class 2 ($P<0.05$). These differences in greenness substantiate the most prominent result of the flux decomposition: the greater photosynthesis of vegetation class 1 at the onset of the growing season 2014 (Figure 34).

Secondly, during periods with a certain wind direction and atmospheric stability, the fetches of some observed fluxes were strongly dominated by only one vegetation class as opposed to the commonly mixed signals. Thus, observed fluxes that are accompanied with a large contribution of one vegetation class ($\Omega>0.7$) were compared to fluxes that were modelled for the same vegetation class (Figure 35). The choice of an Ω of 70 % rested in the desire to identify a trade-off between both applying many fluxes for a broad statistical basis (low Ω) and utilising many fluxes without a mixed fetch for an accurate evaluation (large Ω). Both observed and modelled fluxes match very well as indicated by a mean R^2 of 0.88 and a mean RMSE of 0.82 μmol m^{-2} s^{-1}. Putting these values in context, in a study, where NEE of shrubs and sedges in tundra landscapes was modelled with non-linear regression, a mean R^2 and mean RMSE of 0.69 and 2.15 μmol m^{-2} s^{-1} was respectively obtained (Shaver et al., 2007). The decomposed fluxes of the present study are, when MAE is applied as an intuitive error metric, associated with a mean error of roughly 0.56 μmol m^{-2} s^{-1}. The frequent similarity of the vegetation-class specific flux rates, however, reduces the effectivity of this validation test. Therefore, the observed fluxes governed by one vegetation class were also compared to fluxes modelled for the other class. This counter-check caused a rise in mean RMSE and MAE by 89 % and 99 %, respectively, thus lending further credibility to the modelled flux rates. It can be assumed that this rise would be far greater, if the flux rates of both vegetation classes were less similar.

Thirdly, CC measurements have been carried out with an opaque chamber east of the flux tower (Runkle, B. and

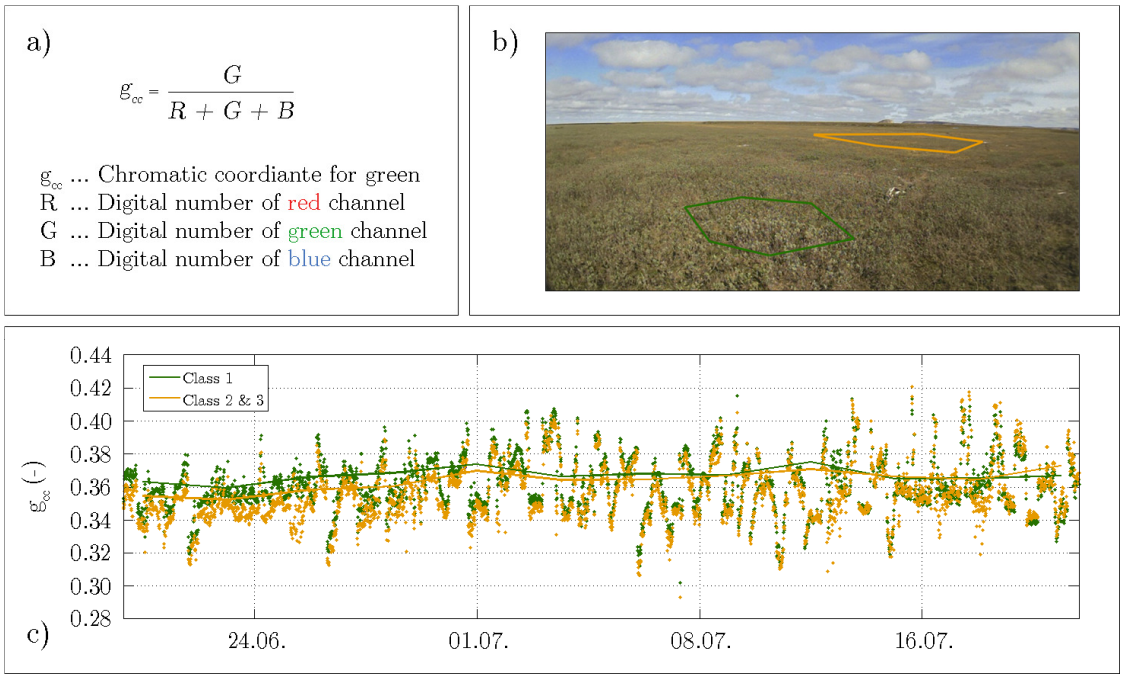

Figure 34 Differences in canopy greenness between vegetation class 1 (green) and vegetation class 2 & 3 (yellow). a) Approach for calculating green chromatic coordinates by means of the digital numbers of the three primary colours in the RGB colour space ($0 \leq$ R, G, B ≤ 255). b) Sample image taken on 25th June 2014 at 5.04 am illustrating both target areas, which green chromatic coordinates were computed for. c) Time series of the green chromatic coordinates of both vegetation classes. The dots represent 30-min values while the lines display their 90th percentiles utilising a moving 3-day window with a step size of 3 days in order to suppress the effects of changing scene illumination. In spring 2014, the vegetation class 1 was greener indicating a greater photosynthesis rate than vegetation class 2 & 3.

Sabrekov, A., personal communication, 2016). Similar to the modelled respiration of vegetation class 2 & 3, a mean carbon dioxide flux with a standard deviation of 2.1 $\pm$ 0.9 µmol m^{-2} s^{-1} (n=5) was determined in this class during mid-June 2014. This mean, however, is conclusive to only a limited extent due to the few underlying measurements. The CC measurements conducted in vegetation class 1 cannot be invoked as they did not incorporate the shrubs due to the small chamber size.

Fourthly, the discussion and comparison of the obtained fitting parameters with values estimated at other sites gives further confidence in the results of flux decomposition (Figure 27):

- R_{base}: The estimated basal respiration values follow a temperature-driven seasonal cycle, in which $R_{base,2\&3}$ is mostly lower than $R_{base,1}$. A smaller autotrophic respiration can be attributed to the smaller biomass of the sedges, and a

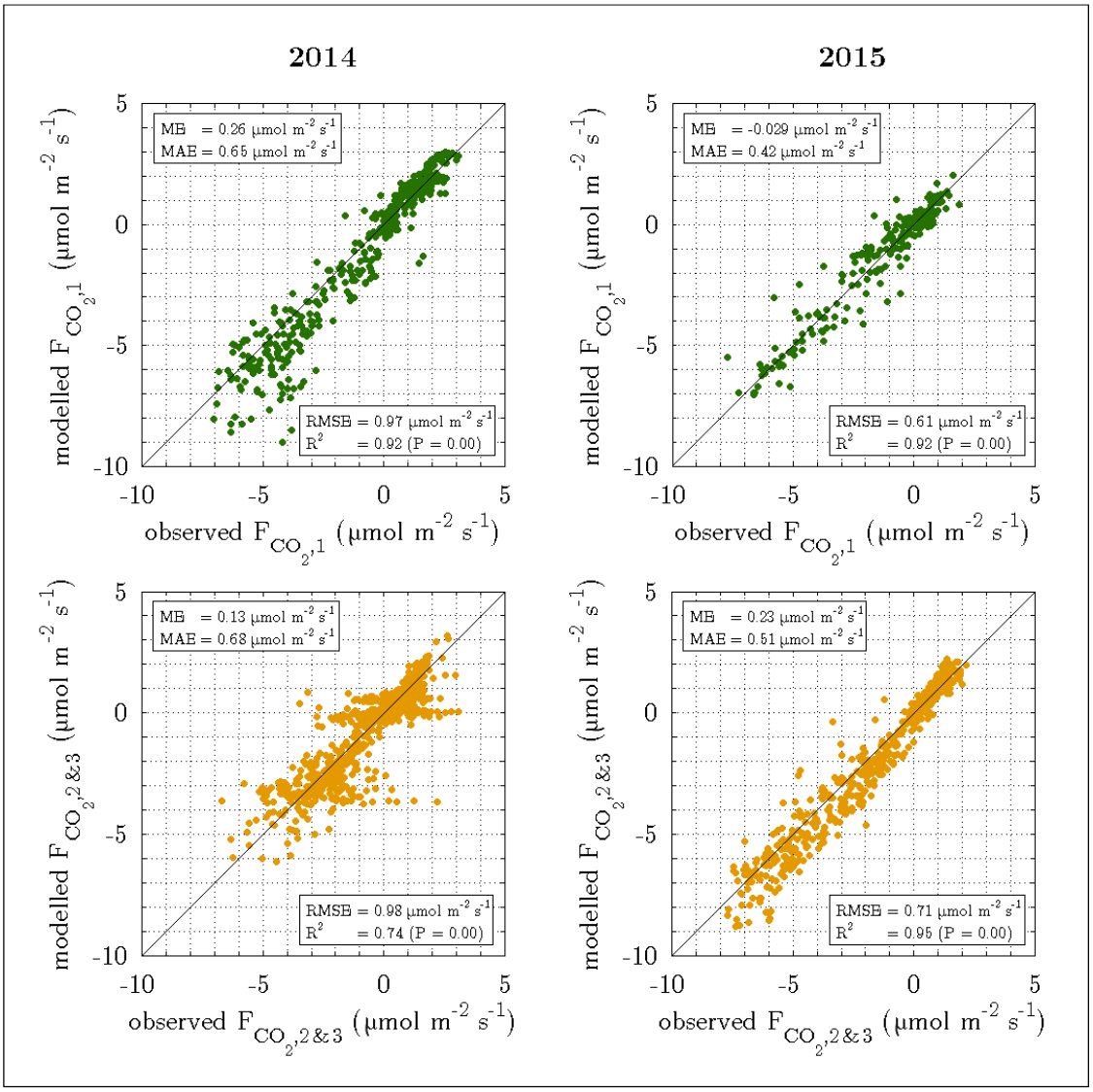

Figure 35 Evaluation of the flux decomposition by plotting observed and quality filtered carbon dioxide fluxes, which had at least 70 % of either vegetation class 1 (green) or vegetation class 2 & 3 (yellow) in their fetch (i.e. Ω>0.7), against modelled fluxes, which were computed for the respective vegetation classes. The assessment was based on the following error measures: mean error (ME), mean absolute error (MAE), root mean square error (RMSE) and coefficient of determination (R^2). The modelled fluxes well correspond to the observed fluxes, thereby appending confidence to the flux decomposition. Furthermore, the smaller residuals in 2015 imply a more reliable flux decomposition than in 2014.

smaller heterotrophic respiration can be ascribed to both increased soil moisture and decreased soil temperature, which in turn hampered microbial activity in the depressions (Hobbie et al., 2000; Walz et al., 2017). For comparison with values found at other sites, a mean peak season TER was computed for vegetation class 1 (2.8 μmol m^{-2} s^{-1}) and vegetation class 2 & 3 (2.3 μmol m^{-2} s^{-1}). While the latter respiratory rate corresponds to the mean mid-growing season respiration of 2.2 μmol m^{-2} s^{-1}, which was estimated for northern peatlands, the former rate is greater (Frolking et al., 1998; Laurila et al., 2001). The comparatively large respiration in vegetation class 1 is likely due to both the large willow shrubs growing up to 1 m (fostering autotrophic respiration) and the large active layer depth of 1 m (facilitating heterotrophic respiration). The contrasting soil characteristics between both vegetation classes prevent drawing conclusions from the computed respirations rates on their foliar respiration fraction (Patankar et al., 2013). However, a higher fraction of heterotrophic respiration in vegetation class 1, as found for the drier polygon rims on the nearby river terrace, can be assumed (Eckhardt, 2017). For ranking the tundra of this study among other ecosystem types from a carbon flux perspective, the following mean respiration rates are appended: 3.46 μmol m^{-2} s^{-1} in forests, 3.94 μmol m^{-2} s^{-1} in crops and 5.39 μmol m^{-2} s^{-1} in grasslands (Ruimy et al., 1995).

- Q_{10}: The estimated temperature sensitivities of 1.42 (vegetation class 1) and 1.48 (vegetation class 2 & 3) are well within the range of $1.3 \lesssim Q_{10} \lesssim 1.5$, which was retrieved across different ecosystems and climates (Mahecha et al., 2010). Furthermore, the fact that $Q_{10,1}$ is lower than $Q_{10,2\&3}$ is in accordance with a concept, which suggests a correlation between a lower/greater temperature sensitivity and a drier/wetter tundra (Olefeldt et al., 2013).

- P_{max}: The estimated maximum photosynthetic potential values also follow a seasonal course indicating the growth and senescence of the canopy. The ratio of $P_{max,1}$ being greater than $P_{max,2\&3}$ is due to the larger biomass of the bushes relative to the sedges. Their estimated P_{max} values agree well to maximum assimilation rates of approximately 15.9 μmol m^{-2} s^{-1} for *Salix pulchra* and 11.1 μmol m^{-2} s^{-1} for *Carex aquatilis* measured during the peak of the Arctic growing season (Oberbauer and Oechel, 1989; Tieszen, 1975). Given a mean mid-growing season P_{max} of 8.6 μmol m^{-2} s^{-1} for northern peatlands, $P_{max,2\&3}$ (8.9 μmol m^{-2} s^{-1}) constitutes a representative uptake capacity, whereas $P_{max,1}$ (12.3 μmol

- m^{-2} s^{-1}) suggests a comparatively large potential for sequestering carbon dioxide (Frolking et al., 1998; Laurila et al., 2001). For putting these values in context, the mean P_{max} of forests, crops and grasslands amount to roughly 35 µmol m^{-2} s^{-1}, 49 µmol m^{-2} s^{-1} and 83 µmol m^{-2} s^{-1}, respectively (Ruimy et al., 1995). Another aspect that indicates the reliability of the estimated P_{max} values is their correlation with the normalised difference vegetation index (NDVI) as seen at many other tundra ecosystems (Mbufong et al., 2014; Shaver et al., 2007). Regarding both growing seasons, NDVI was greater in 2015 suggesting a more active vegetation than in 2014 (ORNL, 2017). Similarly, the P_{max} values of both vegetation classes, in particular the values of the more abundant vegetation class 2, were greater during 2015. Satellite records for tundra landscapes are, however, often confounded by various effects that are particularly profound in high-latitude regions (Stow et al., 2004). Therefore, satellite-derived NDVI values of tundra ecosystems may need to be double-checked with optical sampling in the field, if they are applied to resolve interannual differences (Gamon et al., 2013).

- α: The estimated sensitivities to changes in irradiance α_1 and $\alpha_{2\&3}$ on average amount to 0.042 and 0.04, respectively, and are thus greater than the mean mid-growing season α of northern peatlands amounting to 0.023 (Frolking et al., 1998; Laurila et al., 2001). The high light sensitivity indicates an efficient physiology enabling a considerable photosynthetic activity at low irradiance levels. A similar ratio between both vegetation classes was found utilising numerous quantum yields in the Arctic obtained during the peak season: 0.038 for *Salix* spp. and 0.03 for *Carex* spp. (Shaver et al., 2007). In Seida (Siberia), larger α values around 0.057 were found as well as the relationship between α and the leaf area index (Mbufong et al., 2014). For classification reasons, mean α values for forests, crops and grasslands amount to 0.04, 0.056 and 0.025, respectively (Ruimy et al., 1995).

The fitting parameters are in the range of anticipated values confirming the validity of the decomposed fluxes. They are further lower than the ecophysiological parameters of ecosystems other than tundra. Despite the consequently low carbon turnover, massive quantities of carbon have been accumulated during the past millennia.

4.4. Comparison of budgets

4.4.1. Methane flux

The estimated budgets offer two options for their comparison: budgets of

different years at the same site, and budgets (of preferably the same years) at different sites.

Interannual variability

The footprint budget in 2015 was somewhat higher although soil temperatures were higher for the most part in 2014. However, in 2015, the fetch more often coincided with the location of methane sources in the footprint during the emission peak period in late July and early August. The interannual variability can thus be well explained by the source area composition, which indicates the footprint budget's sensor location bias. The flood plain budgets in 2014 and 2015 are similar in magnitude suggesting little interannual variability despite distinct differences in environmental conditions between both years.

Balances of other Arctic sites

For a general comparison with other tundra ecosystems, these budgets cannot be utilised due to their potentially lacking representativeness, which must be anticipated as long as the deviation of the vegetation class composition of the flood plain of Samoylov Island from the mean vegetation class composition of all flood plains in the Lena River Delta remains unknown. Nevertheless, the budgets of the individual vegetation classes can be compared to other sites since these budgets derive from uniform vegetation with representative flux rates.

On a flood plain of the Indigirka River (Siberia), methane fluxes were investigated employing CC measurements on vegetation classes, which closely resemble the classes of this study (van Huissteden et al., 2009). While their backswamp class exhibits the four-fold emission of vegetation class 3, emissions from vegetation classes 1 and 2 quantitatively match their corresponding levee and levee-backswamp transition classes, when late July as a coinciding period of the year is viewed. On another flood plain of the Kolyma River (Siberia), methane emissions were examined with the aid of CC measurements (Kwon et al., 2017). When considering the peak season period in 2014 at their (undrained) control site, their wet plot displays methane emissions being nearly four times the emission of vegetation class 3. At the same time, their dry plot exhibits a methane uptake in the range of values close to zero as vegetation class 1. Methane sinks have also been found on a flood plain in the taiga area of Alaska (Whalen et al., 1991). Summarising, the budgets from the individual vegetation classes of the flood plain on Samoylov Island are alike in magnitude to budgets of similar Siberian flood plain microforms except the distinctly larger emissions from wet sedge patches at the comparison sites.

The comparison with CC measurements on the river terrace of Samoylov Island revealed the following similarities, when the same summer periods in the years 2014 and 2015 were utilised

(Eckhardt, 2017). The budgets of polygon rims are slightly greater than the budgets of vegetation class 1, but both are in the same range of comparatively low emissions. The budgets of polygon centres are similar to the budgets of vegetation class 2. Thus, the emissions from vegetation class 3 are likely to constitute the largest methane fluxes rates on Samoylov Island, also exceeding the emissions from the margins of open water bodies within the polygonal tundra (Knoblauch et al., 2015).

Assuming representativeness for the footprint budgets of the other eddy covariance system, the flood plain releases per square metre roughly 70 % more methane than the polygonal tundra on the river terrace (Table 6). This comparison is feasible, if the quantitative inferences remain restricted to Samoylov Island (and are not expanded on the Lena River Delta). The larger source strength of the flood plain can be attributed to the annual spring flood and the associated fluvial deposition of both fresh organic matter and nutrients (van Huissteden et al., 2005). The organic matter enhances methane fluxes by providing additional substrate for methanogens. The nutrients constitute an extra supply for primary productivity, which is related to methanogenesis through root exudation (Joabsson and Christensen, 2001). The methane of this enhanced formation is likely to be predominantly emitted via the plant-mediated transport through the abundant sedges preventing methane oxidation.

4.4.2. Carbon dioxide flux

While the methane fluxes of the individual vegetation classes followed similar courses in both years, the carbon dioxide fluxes of the individual vegetation classes took turns at dominating the total carbon dioxide budget.

Interannual variability

The differing flux dynamics between both vegetation classes and years, in particular during the first half of the growing season in 2014, are a result of differences in local features between both vegetation classes (site location, canopy size, physiological traits) and synoptic conditions between both years (temperature progression, snow melt timing).

In 2015, the measurement period, which can be considered usual in terms of air temperatures and snow melt timing, displayed similar sink strengths for both vegetation classes (Figure 32). The snow melt was completed within a couple of days in early June coinciding with the spring flood, and thus enabling a mutual start of canopy development for both vegetation classes. The growing season was initialised by mosses, which are more abundant in vegetation class 2 & 3, in mid-June (Figure 31). Mosses are, in contrast to vascular plants, able to start assimilating right after snow melt since their photosynthetically active tissue can be maintained over winter (Oechel, 1976). From this point until late Septem-

ber/early October, mosses formed a basal uptake. Considerable moss activity until late autumn has also been observed on the nearby river terrace employing EC and CC measurements (Eckhardt, 2017; Kutzbach et al., 2007b). Furthermore, mosses can account for distinctly more than half of total photosynthesis as demonstrated for graminoid areas with high moss cover (Douma et al., 2007; Sommerkorn et al., 1999). However, it is possible that mosses did not fully photosynthesise throughout the growing season due to their tendency to lower their photosynthetic capacity under high irradiance (Murray et al., 1993). This light stress depends on cloudiness, sun angle, moss structure and shadowing by vascular plants, altogether promoting a late-season activity of mosses while other plants went already dormant (Zona et al., 2011). On top of the basal moss activity, the shrubs of vegetation class 1 exhibited a larger net uptake until the growing season peak around late July/early August, after which the sedges of vegetation class 2 & 3 dominated the carbon exchange. That fact that *Carex* spp. started growing earlier than *Salix* spp. has also been observed at other sites; however, considerable variation exists in the timing of phenological events both among and within species (Chapin III et al., 1992; Wielgolaski, 2012). The highest uptake and release of carbon dioxide exhibited vegetation class 1 in both years around the growing season peak, which can be attributed to both the large biomass of the bushes and the warmer, drier soil on the elevated ridge.

In 2014, air temperatures were distinctly higher than the long-term means throughout the measurement period (Figure 16). This deviation led to a prolonged slow snow melt in mid-May already. During this process, the low sedges and mosses remained buried in the depressions with accumulated snow longer than the large bushes on the elevated ridge with less snow. Thereby, the willow twigs were exposed to daytime temperatures above freezing leading to the development of catkins in late May. Hence, vegetation class 1 was more advanced in its phenology than vegetation class 2 & 3 at the onset of the growing season. The consequences were the substantially larger fluxes of vegetation class 1 until the seasonal peak in early August. Apparently, the bushes largely benefitted from increased early growing season temperatures, an effect that has also been found favourable for shrub encroachment in the Arctic (Myers-Smith et al., 2011). Incidentally, shrubs have been growing on Samoylov Island only since the 1960s (Pfeiffer, E.-M., personal communication, 2017). After the growing season peak, vegetation class 1 remained greater in TER while both class exhibited similar GPP rates, causing a greater net uptake of vegetation class 2 & 3. This greater net uptake towards the end of the growing, however, did not make up for the priorly higher sink strength of vegetation class

1 in terms of seasonal budgets. The lower sink strength of vegetation class 2 & 3 could be attributed to a temperature-induced decline in net assimilation of mosses as they are prone to desiccation due to both missing roots and the absent ability to actively regulate their internal water content (Turetsky et al., 2012). Furthermore, more photoinhibition as a consequence of light stress due to more PPFD in this year can be anticipated (Murray et al., 1993). Besides GPP, TER of vegetation class 2 & 3 was lower in magnitude during the warmer year compared to the cooler year. This apparent paradox can be explained by the larger contribution of autotrophic respiration to TER at wet sites than at dry sites as demonstrated on the adjacent river terrace (Eckhardt, 2017). Hence, the lower (less negative) GPP of sedges and mosses was in conjunction with a lower (less positive) TER. This coupling of GPP and TER is, on the other hand, less pronounced in vegetation class 1 since the bushes on the drier sites own a larger contribution of heterotrophic respiration to TER; hence, the higher temperatures probably caused a higher TER with less influence of GPP.

The weather-induced differences in flux rates of the individual vegetation classes during spring 2014 (while a deviation during the remaining measurement periods was absent) indicate a varying implication of the sensor location bias for carbon dioxide fluxes; i.e. climatologically unusual conditions adversely affected the representativeness of the footprint. This hidden aspect of differing sink strengths, which caused the interannual variability, was revealed with the flux decomposition routine further emphasising its utility. In general, the differing flux rates indicate the potential need to regularly examine the representativeness of apparently homogeneous footprints, in particular during prolonged unusual weather conditions as biased budgets may otherwise be estimated.

Lastly, the interannual variability of carbon dioxide fluxes is larger than for methane fluxes. However, the pronounced small-scale variability of methane fluxes is less prominent for carbon dioxide fluxes.

Balances of other Arctic sites

As the air temperatures in 2015 better correspond to long-term means than in 2014, the 2015 budgets are better suited for an inter-site comparison. Hence, the more representative 2015 budget was generally utilised except for the rare case that the budget of the comparison site derived from 2014; then, the biased 2014 budget was applied.

Across various Arctic flux sites, the flood plain of Samoylov Island exhibits a carbon dioxide sink strength being somewhat stronger than the average (Figure 36 and Table 9). While the flood plain sequesters per square metre roughly 20-60 % more carbon dioxide than the polygonal tundra on the adjacent river terrace, its net uptake is distinctly lower (less negative) compared

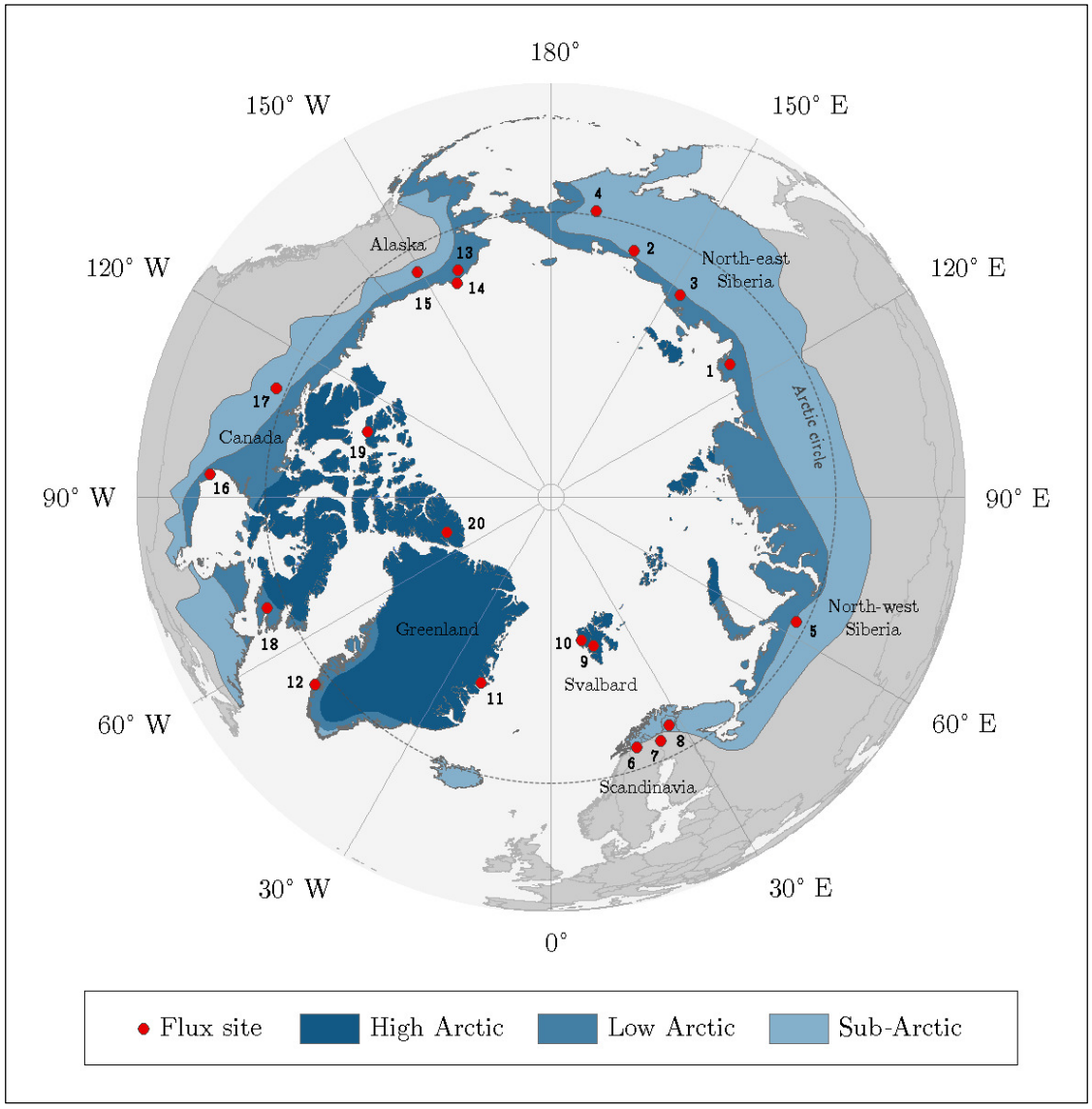

Figure 36 Location of sites utilised for comparison of carbon dioxide budgets with the budgets estimated on the flood plain (Table 9). The classification of the Arctic zones was based on vegetation occurrence (modified from AMAP, 1998). Accordingly, the treeline delimits the (terrestrial) Arctic, i.e. it corresponds with the boundary between sub-Arctic and low Arctic.

to flood plains of the Siberian rivers Kolyma and Indigirka (Kittler et al., 2017; Parmentier et al., 2011a). Other Siberian sites include Seida and Lavrentiya compared to which the flood plain of Samoylov Island displays a similar and stronger sink strength, respectively (Marushchak et al., 2013; Zamolodchikov et al., 2003). Furthermore, the flood plain's sink strength is considerable stronger than budgets of high Arctic sites in Svalbard, Green-

Table 9 Putting the carbon dioxide budgets of the flood plain in perspective with budgets estimated by means of the eddy covariance method at other Arctic sites. The budgets of the present study amount to -4.22 mol m^{-2} (2014) and -5.89 mol m^{-2} (2015) accounting for the period 169-267 (DoY). For an appropriate comparison, the budgets of this study's site were recomputed to match the data periods of the other sites. In this process, representative 2015 flux data was utilised. If the budget of the other site derived from 2014, however, 2014 flux data was only then utilised. If the budget period of the other site exceeded the period of this study's budget, the (few) missing days in the start/end were filled with the daily sum of the first/last day in the budget period. The footnotes behind the site names refer to the numbers in the circumpolar map (Figure 36). Compared to various Arctic sites, the flood plain on Samoylov Island exhibits a fairly strong carbon dioxide sink strength.

Location	Site	Geomorphology	Vegetation	Period	Σ NEE referenced study	Σ NEE present study	Reference
(-)	(-)	(-)	(-)	(DoY (year))	(mol m^{-2})	(mol m^{-2})	(-)
Siberia 72.4° N 126.5° E	Lena River Delta 1 (Samoylov)	river terrace with ice-wedge polygons	wet sedges, mosses	169-267 (2014) 169-267 (2015)	-3.47 -3.74	-4.22 -5.89	Wille, C., personal communication, 2018
Siberia 68.8° N 161.3° E	Chersky 2 (Kolyma River)	flood plain	tussocks, sedges, cotton grasses	169-267 (2014) 169-267 (2015)	-8.42 -7.59	-4.22 -5.89	Kittler et al., 2018
Siberia 70.8° N 147.5° E	Chokurdakh 3 (Indigirka River)	river terrace, flood plain	tussocks, sedges, dwarf shrubs	152-255 (2003-2010)	-6.83	-5.69	Parmentier et al., 2011a

Siberia 65.6° N 171.1° E	Lavrentiya [4]	gentle slope with hummocks and hollows	dwarf shrubs, wet sedges	205-240 (2000)	-2.68	-4.74	Zamolodchikov et al., 2003
Siberia 67.1° N 62.9° E	Seida [5]	hilly upland, bog, fen, lakes	shrubs, dry lichen, heath	168-246 (2008)	-6.59	-6.79	Marushchak et al., 2013
Sweden 68.3° N 18.9° E	Abisko [6]	broad terrace on hill flank	bare rock, dry heath, shrubs, mosses	195-234 (2004)	-3.19	-6.07	Fox et al., 2008
Finland 68.0° N 24.2° E	Lompolo-jänkkä [7]	eutrophic fen	shrubs, sedges	182-212 (2006-2008)	-7.29	-3.85	Aurela et al., 2009
Finland 69.1° N 27.3° E	Kaamanen [8]	mesotrophic fen	shrubs, sedges, mosses	182-212 (1997-2002)	-3.75	-3.85	Aurela et al., 2002
Svalbard 78.2° N 15.9° E	Longyearbyen [9] (Adventdalen)	river terrace with ice-wedge polygons	wet sedges, dry dwarf shrubs	169-267 (2015)	-9.68	-5.89	Pirk et al., 2017
Svalbard 78.9° N 12.0° E	Ny-Ålesund [10] (Bayelva)	gentle hill slope	bare rock, mud boils, grasses	169-267 (2008)	-0.61	-5.89	Lüers et al., 2014

Greenland 74.5° N 20.6° W	Zackenberg [11]	mountain valley	heath	160-236 (2000-2010)	-1.72	-5.62	Lund et al., 2012
Greenland 64.1° N 51.4° W	Kobbefjord [12]	lowland fen	sedges, heath, dwarf shrubs	177-243 (2008-2013, 2015)	-4.69	-7.25	López-Blanco et al., 2017
Alaska 70.5° N 157.4° W	Atqasuk [13]	flat patterned ground	moist tussocks, sedges	169-267 (2006)	-1.51	-5.89	Oechel et al., 2014
Alaska 71.3° N 156.6° W	Barrow [14]	ice-wedge polygons	sedges, mosses, lichens	160-270 (2014)	-1.25	-4.03	Raz-Yaseef et al., 2017
Alaska 68.6° N 149.3° W	Brooks Range [15] (Imnavait Creek)	foothills	heath	152-243 (2008-2015)	-5.61	-6.17	Euskirchen et al., 2016
			tussocks		-7.27	-6.17	
			wet sedges		-5.97	-6.17	
Canada 58.7° N 93.8° W	Churchill [16]	wetland	wet sedges	182-212 (2008)	-5.68	-3.85	Lafleur et al., 2012
Canada 64.9° N 111.6° W	Daring Lake Fen [17]	wetland	wet sedges		-3.63	-3.85	

Canada 64.9° N 111.6° W	Daring Lake Mixed [17]	mixed upland	low shrubs, sedges	182-212 (2008)	-2.84	-3.85	Lafleur et al., 2012
Canada 63.8° N 68.6° W	Iqaluit [18]	mixed upland	tussocks		-1.25	-3.85	
Canada 74.9° N 109.6° W	Cape Bounty [19]	polar semidesert	mosses, lichen		-0.53	-3.85	
Canada 81.8° N 71.4° W	Lake Hazen [20]	polar semidesert	lichen		-0.85	-3.85	

land and Canada (Lafleur et al., 2012; López-Blanco et al., 2017; Lüers et al., 2014; Lund et al., 2012); one exception is the site close to Longyearbyen, which surprisingly exhibits the largest net uptake among all compiled sites (Pirk et al., 2017). In comparison to sites in either low Arctic or sub-Arctic, no general conclusions can be drawn, which is likely due to the ubiquitously high spatiotemporal flux variability in the Arctic region. Also, no uniform picture emerges in the comparison with Scandinavian peatlands (Aurela et al., 2002, 2009; Fox et al., 2008). When comparing with sites in the northern part of the north slope of Alaska, the flood plain exhibits a substantially higher carbon dioxide sequestration (Oechel et al., 2014; Raz-Yaseef et al., 2017); in the southern part, however, similar sink strengths seem to prevail (Euskirchen et al., 2016). In summary, the flood plain possess a robust carbon dioxide sink strength, which appears particularly noteworthy, when local conditions are taken into consideration: the mean net radiation during the growing season is lower than for most Arctic sites and the underlying permafrost displays one of the lowest ground temperatures in the world (Boike et al., 2013; Obu et al., 2018; Romanovsky et al., 2010). These diminishing factors are counterbalanced by an annual deposition of nutrients in the course of spring flooding (van Huissteden et al., 2005).

4.4.3. Greenhouse gas flux

The two global warming potential concepts are associated with uncertainties, but the relative uncertainty range is wider for GTP compared to GWP (Myhre et al., 2013). For example, the GTP values can be considerably affected by assumptions about the climate sensitivity and the heat uptake by the ocean. Hence, the rather conservative greenhouse gas budgets obtained with GWP as a conversion metric appear to be a more reasonable. Applying a time horizon longer than the chosen 100 years reduces the impact of the methane budget on the greenhouse gas budget due to the limited atmospheric lifetime of methane. Thus, the sink strength becomes stronger.

The methane emissions largely counteracted the carbon dioxide net uptake during the comparison period, which is similar to the growing season. On the annual scale, the greenhouse gas sink strength is likely to be weaker. This assumption is based on the accumulating evidence that the release of methane and carbon dioxide is not negligible during the very cold winter – in contrast to the historic view of a wintertime inactivity in Arctic ecosystems (van der Molen et al., 2007). For instance, at multiple sites in Alaska, the non-summertime release of carbon was found to equal 1-2 times the summertime uptake (Euskirchen et al., 2012; Oechel et al., 2014; Zona et al., 2016).

For a complete carbon balance, lateral fluxes of both particulate and dissolved organic and inorganic carbon also need to be taken into account (Chapin III et al., 2006). However, their magnitude can, in comparison to the observed vertical fluxes, only be hypothesised due to missing measurements. The first out of two noteworthy lateral carbon fluxes constitutes the Lena River during spring flooding in June. Among the three great Siberian rivers draining into the Arctic Ocean (Ob, Yenisei, Lena), the Lena river ranks first in terms of both total suspended matter and total organic carbon export (Cauwet and Sidorov, 1996). A large portion of this discharge takes place in the course of the spring flood; however, the question on the quantity of the net import on the flood plain remains unanswered (Fedorova et al., 2015). The second noteworthy lateral carbon flux represents the backswamp in the eastern footprint, where water from a draining thermokarst lake on the river terrace is transferred to the outlet in the north of the flood plain. By way of contrast, the north-western trench in the footprint displays standing water, and lateral transport thus ought to be negligible. The lateral export of carbon, however, plays only a tangential role relative to the vertical fluxes as measurements have demonstrated: the water from a small catchment area on the river terrace draining onto the flood plain exported on average about 3.7 g m^{-2} of dissolved organic carbon during the growing season 2014 (Petersen, 2015). During the same period, the eddy covariance system on the river terrace, whose footprint overlaps with the small watershed, yielded a cumulative TER of 92.9 g C m^{-2} and a cumulative GPP of -138.6 g C m^{-2} (Wille, C., personal communication, 2018).

Finally, scaling and balancing carbon fluxes in an tundra ecosystem with a high spatial heterogeneity requires a high temporal resolution such as the 30-min flux interval; the application of daily flux means does not consider the whole spatial heterogeneity (Budishchev et al., 2014). Simultaneously, the application of fine-scale surface imagery is essential; Landsat scenes for instance are likely to be too coarse (Schneider et al., 2009). The necessity of considering the surface heterogeneity in the process of upscaling greenhouse gas fluxes, in particular methane fluxes, became clearly evident through the considerable overestimation of the sink strength, obtained through simply upscaling footprint budgets without the preceding downscaling procedure.

5. Synthesis

5.1. Conclusion

The flood plain on Samoylov Island constitutes an interesting tundra ecosystem that is characterised by both an annual spring flood that deposits flux-enhancing nutrients, and a heterogeneous surface that causes a distinctive variability in carbon fluxes. This variability could be well explained by invoking the distribution of vegetation classes. Although the eddy covariance method yielded fluxes that integrated across the heterogeneous surface, the partitioning of these mixed signals was successful in that individual fractions within the ecosystem could be viewed in isolation.

This flux decomposition allowed insights into the flux dynamics of individual vegetation classes. Shrubby vegetation was found to exhibit negligible methane emissions, while scattered patches of graminoid vegetation likely displayed the largest methane emissions on Samoylov Island. On account of these opposing source strengths distributed across the surface, the temporal variability was very high in the observed fluxes on the daily scale. By contrast, the lower temporal variability in the carbon dioxide fluxes was rather driven by the diurnal cycle of both photosynthesis and meteorological parameters. However, during an unusually warm spring period, the shrubs featured a considerably greater net uptake than the sedges. This concealed deviation, as both classes normally exhibited similar flux rates, could be revealed by means of the downscaling procedure. Accordingly, fluxes observed in a footprint, which is considered representative, may lack representativeness in response to climate anomalies. This aspect may gain importance against the projected rise in weather extremes in the course of climate change.

For investigating this small-scale flux variability, conducting a series of chamber measurements would be the typical approach. Chamber measurements are, however, associated with several drawbacks that bias the flux determination. Circumventing these problems with the eddy covariance method on the mesoscale (whilst resolving the pronounced variability on the microscale) enabled the extrapola-

tion of data from a point measurement beyond the footprint of the flux tower.

The subsequently estimated carbon budgets of the entire flood plain constitute robust balances that allow a reliable assessment of its carbon sink/source strength by evading sensor location bias-related issues. Ignoring the lacking footprint representativeness by a direct upscaling of the footprint budgets was demonstrated to cause a misjudgements in the form of a considerable overestimation of the greenhouse gas sink strength. In case of a further upscaling, such substantial biases would then propagate, e.g. into the regional scale, causing spurious carbon balances.

5.2. Outlook

The eddy covariance method will remain one of the most accurate and defensible approaches for determining carbon fluxes and budgets of ecosystems in the (near) future. Thus, the further investigation of the effects of a heterogeneous surface on fluxes and budgets is as essential as the compensation of this bias since most of the natural surfaces are not homogeneous (depending on the desired scale and the examined greenhouse gas). In this context, the transferability of the hereby demonstrated methodology of flux decomposition to other Arctic ecosystems is worth examining. It can be anticipated that the application of similar parameterisations, i.e. the recalibration of the proposed model functions with roughly the same flux drivers, is likely to yield satisfying results. Moreover, adopting the basics of this methodology, i.e. fitting a set of area-weighted, surface class-specific flux models to the observed flux, in ecosystems outside the Arctic is certainly conceivable. Following this broad applicability beyond micrometeorological issues in periglacial environments, this modelling approach may also be supportive in the fields of landscape ecology, experimental agronomy, catchment hydrology and biogeochemistry.

Based on the close coupling between carbon fluxes and vegetation cover, the demand for regional carbon budgets could be addressed through extensive vegetation mapping. The required remote sensing images therefore need to have a high resolution, preferably in the sub-metre range, in order to resolve small-scale changes in surface characteristics that are ubiquitous in the Arctic tundra. Such an approach would account for the sub-grid variability, which regional-scale models often neglect. Precise carbon budgets are particularly important against the background of growing concern about the implications of climate change in the Arctic. Furthermore, investigating the vegetation composition of other flood plains in the Lena River Delta would also enable the assessment of the representativeness of the vegetation composition, and thus the determined carbon fluxes, of the flood plain on Samoylov

Island. Another method to directly evaluate the representativeness of the flood plain fluxes regarding other flood plains in the delta could be airborne eddy covariance measurements.

Surface characteristics are also subject to a change, even in a rapid way in view of climate change. For instance, the northerly migrating shrubs own the potential to distinctly alter the sink strength of tundra ecosystems. Their interesting role became evident through the comparatively large net uptake during the high springtime temperatures, which possibly constituted a window into the future. Further research effort should also be devoted to both the link of the carbon turnover to nitrogen dynamics, and the qualitative and quantitative implications of the spring flood on the carbon fluxes of the flood plain on Samoylov Island in the Lena River Delta.

References

Allison, S. D. and Treseder, K. K.: Climate change feedbacks to microbial decomposition in boreal soils, Fungal Ecol., 4(6), 362–374, doi:10.1016/j.funeco.2011.01.003, 2011.

AMAP: Assessment report: Arctic pollution issues, Oslo. [online] available from: https://www.amap.no/documents/doc/amap-assessment-report-arctic-pollution-issues/68, 1998.

Aubinet, M., Grelle, A., Ibrom, A., Rannik, Ü., Moncrieff, J., Foken, T., Kowalski, A. S., Martin, P. H., Berbigier, P., Bernhofer, C., Clement, R., Elbers, J., Granier, A., Grünwald, T., Morgenstern, K., Pilegaard, K., Rebmann, C., Snijders, W., Valentini, R. and Vesala, T.: Estimates of the Annual Net Carbon and Water Exchange of Forests: The EUROFLUX Methodology, Adv. Ecol. Res., 30(C), 113–175, doi:10.1016/S0065-2504(08)60018-5, 1999.

Aubinet, M., Vesala, T. and Papale, D.: Eddy Covariance, a practical guide to measurement and data analysis, 1st ed., Springer., 2012.

Audet, J., Johansen, J. R., Andersen, P. M., Baattrup-Pedersen, A., Brask-Jensen, K. M., Elsgaard, L., Kjaergaard, C., Larsen, S. E. and Hoffmann, C. C.: Methane emissions in Danish riparian wetlands: Ecosystem comparison and pursuit of vegetation indexes as predictive tools, Ecol. Indic., 34, 548–559, doi:10.1016/j.ecolind.2013.06.016, 2013.

Aurela, M., Laurila, T. and Tuovinen, J. P.: Annual CO_2 balance of a subarctic fen in northern Europe: Importance of the wintertime efflux, J. Geophys. Res., 107(21), doi:10.1029/2002JD002055, 2002.

Aurela, M., Laurila, T. and Tuovinen, J.-P.: The timing of snow melt controls the annual CO_2 balance in a subarctic fen, Geophys. Res. Lett., 31(16), L16 119, doi:10.1029/2004GL020315, 2004.

Aurela, M., Lohila, A., Tuovinen, J.-P., Hatakka, J., Riutta, T. and Laurila, T.: Carbon dioxide exchange on a northern boreal fen, Boreal Environ. Res., 14(4), 699–710 [online] available from: http://www.borenv.net, 2009.

Belshe, E. F., Schuur, E. G., Bolker, B. M. and Bracho, R.: Incorporating spatial heterogeneity created by permafrost thaw into a landscape carbon estimate, J. Geophys. Res., 117(G1), G01026, doi:10.1029/2011JG001836, 2012.

Boike, J., Kattenstroth, B., Abramova, K., Bornemann, N., Chetverova, A., Fedorova, I., Fröb, K., Grigoriev, M., Grüber, M., Kutzbach, L., Langer, M., Minke, M., Muster, S., Piel, K., Pfeiffer, E. M., Stoof, G., Westermann, S., Wischnewski, K., Wille, C. and Hubberten, H. W.: Baseline characteristics of climate, permafrost and land cover from a new permafrost observatory in the Lena River Delta, Siberia (1998-2011), Biogeosciences, 10(3), 2105–2128, doi:10.5194/bg-10-2105-2013, 2013.

Bubier, J. L., Moore, T. R., Bellisario, L., Comer, N. T. and Crill, P. M.: Ecological controls on methane emissions from a Northern Peatland Complex in the zone of discontinuous permafrost, Manitoba, Canada, Global Biogeochem. Cycles, 9(4), 455–470, doi:10.1029/95GB02379, 1995.

Budishchev, A., Mi, Y., Van Huissteden, J., Belelli-Marchesini, L., Schaepman-Strub, G., Parmentier, F. J. W., Fratini, G. and Dolman, A. J.: Evaluation of a plot-scale methane emission model using eddy covariance observations and footprint modelling, Biogeosciences, 11(17), 4651–4664, doi:10.5194/bg-11-4651-2014, 2014.

Callaghan, T. V., Björn, L. O., Chapin, F. S. I., Chernov, Y., Christensen, T. R., Huntley, B., Ims, R., Johansson, M., Riedlinger, D. J., Jonasson, S., Matveyeva, N., Oechel, W. C., Panikov, N. and Shaver, G. R.: Arctic tundra and polar desert ecosystems, in Arctic Climate Impact Assessment, Cambridge University Press, 2005.

Cauwet, G. and Sidorov, I.: The biogeochemistry of Lena River: organic carbon and nutrients distribution, Mar. Chem., 53(3–4), 211–227, doi:10.1016/0304-4203(95)00090-9, 1996.

Chanton, J. P. and Whiting, G. J.: Trace gas exchange in freshwater and coastal marine environments: Ebullition and transport by plants, in Biogenic Trace Gases: Measuring Emissions from Soil and Water, edited by P. A. Matson and R. C. Harriss, pp. 98–125, Blackwell, Oxford., 1995.

Chapin III, F. S., Jefferies, R. L., Reynolds, J. F. and Svoboda, J.: Arctic ecosystems in a changing climate, Academic Press, San Diego, 1992.

Chapin III, F. S., Berman, M., Callaghan, T. V., Convey, P., Crepin, A.-S., Danell, K., Ducklow, H., Forbes, B., Kofinas, G., McGuire, A. D., Nuttall, M., Virginia, R. and Sergei, A. Z.: Polar Systems (Chapter 25). In: Ecosystems and Human Well-being: Current State and Trends, edited by B. Fitzharris, Island Press. [online] available from: https://www.millenniumassessment.org/documents/document.294.aspx.pdf, 2005.

Chapin III, F. S., Woodwell, G. M., Randerson, J. T., Rastetter, E. B., Lovett, G. M., Baldocchi, D. D., Clark, D. A., Harmon, M. E., Schimel, D. S., Valentini, R., Wirth, C., Aber, J. D., Cole, J. J., Goulden, M. L., Harden, J. W., Heimann, M., Howarth, R. W., Matson, P. A., McGuire, A. D., Melillo, J. M., Mooney, H. A., Neff, J. C., Houghton, R. A., Pace, M. L., Ryan, M. G., Running, S. W., Sala, O. E., Schlesinger, W. H. and Schulze, E. D.: Reconciling carbon-cycle concepts, terminology, and methods, Ecosystems, 9(7), 1041–1050, doi:10.1007/s10021-005-0105-7, 2006.

Christensen, T. R., Friborg, T., Sommerkorn, M., Kaplan, J., Illeris, L., Soegaard, H., Nordstroem, C. and Jonasson, S.: Trace gas exchange in a high-Arctic valley: 1. Variations in CO_2 and CH_4 Flux between tundra vegetation types, Glob. Biochem. Cycles, 14(3), 701–713, doi:10.1029/1999GB001134, 2000.

Christensen, T. R., Johansson, T., Åkerman, H. J. and Mastepanov, M.: Thawing sub-Arctic permafrost: effects on vegetation and methane emissions, Geophys. Res. Lett., 31(4), L04501, doi:10.1029/2003GL018680, 2004.

Ciais, P., Sabine, C., Bala, G., Bopp, L., Brovkin, V., Canadell, J., Chhabra, A., DeFries, R., Galloway, J., Heimann, M., Jones, C., Quéré, C. Le, Myneni, R. B., Piao, S. and Thornton, P.: Carbon and Other Biogeochemical Cycles (Chapter 6). In: Climate Change 2013: The Physical Science Basis. Contribution of Working Group I to the Fifth Assessment Report of the Intergovernmental Panel on Climate Change, Cambridge University Press. [online] available from: http://www.ipcc.ch/report/ar5/wg1, 2013.

Cicerone, R. J. and Oremland, R. S.: Biogeochemical aspects of atmospheric methane, Global Biogeochem. Cycles, 2(4), 299–327, doi:10.1029/GB002i004p00299, 1988.

Collins, M., Knutti, R., Arblaster, J., Dufresne, J. L., Fichefet, T., Friedlingstein, P., Gao, X., Gutowski, W. J., Johns, T., Krinner, G., Shongwe, M., Tebaldi, C., Weaver, A. J. and Wehner, M.: Long-term Climate Change: Projections, Commitments and Irreversibility (Chapter 12). In: Climate Change 2013: The Physical Science Basis. Contribution of Working Group I to the Fifth Assessment Report of the Intergovernmental Panel on Climate Change, Cambridge University Press. [online] available from: http://www.ipcc.ch/report/ar5/wg1, 2013.

Davidson, E. A. and Janssens, I. A.: Temperature sensitivity of soil carbon decomposition and feedbacks to climate change, Nature, 440(7081), 165–173, doi:10.1038/nature04514, 2006.

Davidson, S. J., Sloan, V. L., Phoenix, G. K., Wagner, R., Fisher, J. P., Oechel, W. C. and Zona, D.: Vegetation Type Dominates the Spatial Variability in CH_4 Emissions Across

Multiple Arctic Tundra Landscapes, Ecosystems, 19(6), 1116–1132, doi:10.1007/s10021-016-9991-0, 2016.

Dedysh, S. N.: Methanotrophic bacteria of acidic Sphagnum peat bogs, Microbiology, 71(6), 638–650, doi:10.1023/A:1021467520274, 2002.

Dengel, S., Zona, D., Sachs, T., Aurela, M., Jammet, M., Parmentier, F. J. W., Oechel, W. and Vesala, T.: Testing the applicability of neural networks as a gap-filling method using CH_4 flux data from high latitude wetlands, Biogeosciences, 10(12), 8185–8200, doi:10.5194/bg-10-8185-2013, 2013.

Detto, M., Montaldo, N., Albertson, J. D., Mancini, M. and Katul, G.: Soil moisture and vegetation controls on evapotranspiration in a heterogeneous Mediterranean ecosystem on Sardinia, Italy, Water Resour. Res., 42(8), 1–16, doi:10.1029/2005WR004693, 2006.

Dorrepaal, E., Toet, S., Van Logtestijn, R. S. P., Swart, E., Van De Weg, M. J., Callaghan, T. V. and Aerts, R.: Carbon respiration from subsurface peat accelerated by climate warming in the subarctic, Nature, 460(7255), 616–619, doi:10.1038/nature08216, 2009.

Douma, J. C., Van Wijk, M. T. and Shaver, G. R.: The contribution of mosses to the carbon and water exchange of arctic ecosystems: Quantification and relationships with system properties, Plant, Cell Environ., 30(10), 1205–1215, doi:10.1111/j.1365-3040.2007.01697.x, 2007.

Draper, N. R. and Smith, H.: Applied Regression Analysis, 3rd ed., Hoboken, NJ: Wiley-Interscience., 1998.

Eckhardt, T.: Partitioning carbon fluxes in a permafrost landscape, Doctoral thesis, University of Hamburg, [online] available from: http://ediss.sub.uni-hamburg.de/volltexte/2017/8716/, 2017.

Euskirchen, E. S., Bret-Harte, M. S., Scott, G. J., Edgar, C. and Shaver, G. R.: Seasonal patterns of carbon dioxide and water fluxes in three representative tundra ecosystems in northern Alaska, Ecosphere, 3(1), 1–19, doi:10.1890/ES11-00202.1, 2012.

Euskirchen, E. S., Bret-Harte, M. S., Shaver, G. R., Edgar, C. W. and Romanovsky, V. E.: Long-Term Release of Carbon Dioxide from Arctic Tundra Ecosystems in Alaska, Ecosystems, 20(5), 960–974, doi:10.1007/s10021-016-0085-9, 2016.

van Everdingen, R. O.: Multi-language Glossary of Permafrost and Related Ground-Ice Terms (International Permafrost Association), Calgary, Alberta, Canada., 2005.

Fedorova, I., Chetverova, A., Bolshiyanov, D., Makarov, A., Boike, J., Heim, B., Morgenstern, A., Overduin, P. P., Wegner, C., Kashina, V. and Sidorina, I.: Lena Delta hydrology and geochemistry: long-term hydrological data and recent field observations, Biogeosciences, 12(2), 345–363, doi:10.5194/bg-12-345-2015, 2015.

Finkelstein, P. L. and Sims, P. F.: Sampling error in eddy correlation flux measurements, J. Geophys. Res., 106(D4), 3503, doi:10.1029/2000JD900731, 2001.

Fisher, J.: Conservation GIS Data, accessed 12th August 2016, [online] available from: http://maps.tnc.org/gis_data.html, 2016.

Foken, T.: Micrometeorology, 1st ed., Springer., 2008.

Foken, T. and Wichura, B.: Tools for quality assessment of surface-based flux measurements, Agric. For. Meteorol., 78(1–2), 83–105, doi:10.1016/0168-1923(95)02248-1, 1996.

Forbrich, I., Kutzbach, L., Wille, C., Becker, T., Wu, J. and Wilmking, M.: Cross-evaluation of measurements of peatland methane emissions on microform and ecosystem scales using high-resolution landcover classification and source weight modelling, Agric. For. Meteorol., 151(7), 864–874, doi:10.1016/j.agrformet.2011.02.006, 2011.

Fox, A. M., Huntley, B., Lloyd, C. R., Williams, M. and Baxter, R.: Net ecosystem exchange over heterogeneous Arctic tundra: Scaling between chamber and eddy covariance measurements, Global Biogeochem. Cycles, 22(2), doi:10.1029/2007GB003027, 2008.

Frolking, S. S., Bubier, J. L., Moore, T. R., Bellisario, L. M., Bhardwaj, A., Carroll, P., Grill, P. M., Lafleur, P. M., McCaughey, J. H., Roulet, N. T., Suyker, A. E., Verma, S. B., Waddington, J. M. and Whiting, G. J.: Relationship between ecosystem productivity and photosynthetically active radiation from northern peatlands, Global Biogeochem. Cycles, 12(1), 115–126, doi:10.1029/97GB03367, 1998.

Gajewski, K., Viau, A., Sawada, M., Atkinson, L. J. and Wilson, S.: Sphagnum peatland distribution in North America and Eurasia during the past 21,000 years, Global Biogeochem. Cycles, 15(2), 297–310, doi:10.1029/2000GB001286, 2001.

Gamon, J. A., Huemmrich, K. F., Stone, R. S. and Tweedie, C. E.: Spatial and temporal variation in primary productivity (NDVI) of coastal Alaskan tundra: Decreased vegetation growth following earlier snowmelt, Remote Sens. Environ., 129, 144–153, doi:10.1016/j.rse.2012.10.030, 2013.

Gao, Y., Markkanen, T., Aurela, M., Mammarella, I., Thum, T., Tsuruta, A. and Aalto, T.: Response of water use efficiency to summer drought in a boreal Scots pine forest in Finland, Biogeosciences, 14(18), 4409–4422, doi:10.5194/bg-14-4409-2017, 2017.

Gazovic, M., Kutzbach, L., Schreiber, P., Wille, C. and Wilmking, M.: Diurnal dynamics of CH_4 from a boreal peatland during snowmelt, Tellus, 62(3), doi:10.1111/j.1600-0889.2010.00455.x, 2010.

Godin, E., Fortier, D. and Coulombe, S.: Effects of thermo-erosion gullying on hydrologic flow networks, discharge and soil loss, Env. Res. Lett., 9, doi: 10.1088/1748-9326/9/10/105010, 2014.

Gould, W. A., Raynolds, M. and Walker, D. A.: Vegetation, plant biomass, and net primary productivity patterns in the Canadian Arctic, J. Geophys. Res., 108(D2), 8167, doi:10. 1029/2001JD000948, 2003.

Gray, A., Levy, P. E., Cooper, M. D. a, Jones, T., Gaiawyn, J., Leeson, S. R., Ward, S. E., Dinsmore, K. J., Drewer, J., Sheppard, L. J., Ostle, N. J., Evans, C. D., Burden, A. and Zieliński, P.: Methane indicator values for peatlands: a comparison of species and functional groups., Glob. Chang. Biol., 19(4), 1141–50, doi:10.1111/gcb.12120, 2013.

Grigoriev, M.: Cryomorphogenesis in the Lena Delta, Permafr. Inst. Press. Yakutsk, 176 (in Russian), 1993.

Groendahl, L., Friborg, T. and Soegaard, H.: Temperature and snow-melt controls on interannual variability in carbon exchange in the high Arctic, Theor. Appl. Clim., 88(1–2), 111–125, doi:10.1007/s00704-005-0228-y, 2007.

Grünfeld, S. and Brix, H.: Methanogenesis and methane emissions: Effects of water table, substrate type and presence of Phragmites australis, Aquat. Bot., 64(1), 63–75, doi:10.1016/ S0304-3770(99)00010-8, 1999.

Hanis, K. L., Tenuta, M.. and Papakyriakou, T. N.: Seasonal dynamics of methane emissions from a subarctic fen in the Hudson Bay Lowlands, Biogeosciences, 10(7), 4465–4479, doi:10.5194/ bg-10-4465-2013, 2013.

Haraguchi, A. and Yamada, N.: Temperature Dependency of Photosynthesis of Sphagnum spp. Distributed in the Warm-Temperate and the Cool-Temperate Mires of Japan, Am. J. Plant Sci., 2(5), 716–725, doi:10.4236/ ajps.2011.25086, 2011.

Harden, J. W., Koven, C. D., Ping, C. L., Hugelius, G., David McGuire, A., Camill, P., Jorgenson, T., Kuhry, P., Michaelson, G. J., O'Donnell, J. A., Schuur, E. A. G., Tarnocai, C., Johnson, K. and Grosse, G.: Field information links permafrost carbon to physical vulnerabilities of thawing, Geophys. Res. Lett., 39(15), doi:10.10 29/2012GL051958, 2012.

Hartmann, D. L., Klein Tank, A. M. G., Rusticucci, M., Alexander, L. V., Brönnimann, S., Charabi, Y. A. R., Dentener, F. J., Dlugokencky, E. J., Easterling, D. R., Kaplan, A., Soden, B. J., Thorne, P. W., Wild, M. and Zhai, P.: Observations: Atmosphere and surface (Chapter 2). In: Climate Change 2013: The Physical Science Basis. Contribution of Working Group I to the Fifth Assessment Report of the Intergovernmental Panel on Climate Change, Cambridge University Press, 2013.

Haykin, S.: Neural networks, 2nd ed., Prentice Hall, Upper Saddle River, New Jersey, 1999.

Heikkinen, J. E. P., Maljanen, M., Aurela, M., Hargreaves, K. J. and Martikainen, P. J.: Carbon dioxide and methane dynamics in a sub-Arctic peatland in northern Finland, Polar Res., 21(1), 49–62, doi:10.3402/polar.v21i1.6473, 2002.

Heikkinen, J. E. P., Virtanen, T., Huttunen, J. T., Elsakov, V. and Martikainen, P. J.: Carbon balance in East European tundra, Global Biogeochem. Cycles, 18, doi:10.1029/2003GB002054, 2004.

Heimann, M. and Reichstein, M.: Terrestrial ecosystem carbon dynamics and climate feedbacks, Nature, 451(7176), 289–292, doi:10.1038/nature06591, 2008.

Hobbie, S. E., Schimel, J. P., Trumbore, S. E. and Randerson, J. R.: Controls over carbon storage and turnover in high-latitude soils, Glob. Chang. Biol., 6(S1), 196–210, doi:10.1046/j.1365-2486.2000.06021.x, 2000.

Horst, T. W. and Lenschow, D. H.: Attenuation of Scalar Fluxes Measured with Spatially-displaced Sensors, Boundary-Layer Meteorol., 130(2), 275–300, doi:10.1007/s10546-008-9348-0, 2009.

Hubberten, H. W., Wagner, D., Pfeiffer, E. M., Boike, J. and Gukov, A. Y.: The Russian-German research station Samoylov, Lena Delta - A key site for polar research in the Siberian Arctic, Polarforschung, 73(2/3), 111–116, 2006.

Hudson, J. M. G., Henry, G. H. R. and Cornwell, W. K.: Taller and larger: shifts in Arctic tundra leaf traits after 16 years of experimental warming, Glob. Ch. Biol., 17(2), 1013–1021, doi:10.1111/j.1365-2486.2010.02294.x, 2011.

Hugelius, G., Tarnocai, C., Broll, G., Canadell, J. G., Kuhry, P. and Swanson, D. K.: The northern circumpolar soil carbon database: Spatially distributed datasets of soil coverage and soil carbon storage in the northern permafrost regions, Earth Syst. Sci. Data, 5(1), 3–13, doi:10.5194/essd-5-3-2013, 2013.

Hugelius, G., Strauss, J., Zubrzycki, S., Harden, J. W., Schuur, E. A. G., Ping, C. L., Schirrmeister, L., Grosse, G., Michaelson, G. J., Koven, C. D., O'Donnell, J. A., Elberling, B., Mishra, U., Camill, P., Yu, Z., Palmtag, J. and Kuhry, P.: Estimated stocks of circumpolar permafrost carbon with quantified uncertainty ranges and identified data gaps, Biogeosciences, 11(23), 6573–6593, doi:10.5194/bg-11-6573-2014, 2014.

van Huissteden, J., Maximov, T. C. and Dolman, A. J.: High methane flux from an arctic floodplain (Indigirka lowlands, eastern Siberia), J. Geophys. Res. Biogeosciences, 110(G2), G02002, doi:10.1029/2005JG000010, 2005.

van Huissteden, J., Maximov, T. C. and Dolman, A. J.: Correction to "High

methane flux from an arctic floodplain (Indigirka lowlands, eastern Siberia)," J. Geophys. Res., 114, doi:10.1029/2009JG001040, 2009.

Ibrom, A., Dellwik, E., Flyvbjerg, H., Jensen, N. O. and Pilegaard, K.: Strong low-pass filtering effects on water vapour flux measurements with closed-path eddy correlation systems, Agric. For. Meteorol., 147(3–4), 140–156, doi:10.1016/j.agrformet.2007.07.007, 2007.

IPA: International Permafrost Association, Philippe Rekacewic (UNEP/GRID-Arendal), 1998.

IPCC: Climate Change 2014: Synthesis Report. Contribution of Working Groups I, II and III to the Fifth Assessment Report of the Intergovernmental Panel on Climate Change, edited by Core Writing Team, R. K. Pachauri, and L. A. Meyer, Cambridge University Press, Geneva., 2014.

Jia, G. J., Epstein, H. E. and Walker, D. A.: Vegetation greening in the canadian arctic related to decadal warming, J. Environ. Monit., 11(12), 2231, doi:10.1039/b911677j, 2009.

Joabsson, A. and Christensen, T. R.: Methane emissions from wetlands and their relationship with vascular plants: an Arctic example, Glob. Chang. Biol., 7(8), 919–932, doi:10.1046/j.1354-1013.2001.00044.x, 2001.

Joabsson, A., Christensen, T. R. and Wallen, B.: Vascular plant controls on methane emissions from northern peatforming wetlands, Trends Ecol. Evol., 14(10), 385–388, doi:10.1016/S0169-5347(99)01649-3, 1999.

Johnson, L. C., Shaver, G. R., Cades, D. H., Rastetter, E., Giblin, A., Laundre, J. and Stanley, A.: Plant Carbon-Nutrient Interactions Control CO_2 Exchange in Alaskan Wet Sedge Tundra Ecosystems, Ecology, 81(2), 453–469, doi:10.2307/177439, 2000.

Johnston, C. E., Ewing, S. A., Harden, J. W., Varner, R. K., Wickland, K. P., Koch, J. C., Fuller, C. C., Manies, K. and Jorgenson, M. T.: Effect of permafrost thaw on CO_2 and CH_4 exchange in a western Alaska peatland chronosequence, Env. Res. Lett., 9, doi:10.1088/1748-9326/9/10/109601, 2014.

Jørgensen, C., Johansen, K. M., Westergaard-Nielsen, A. and Elberling, B.: Net regional methane sink in High Arctic soils of northeast Greenland, Nat. Geosci., 8(1), 20–23, doi:10.1038/ngeo2305, 2015.

Jorgenson, M. T., Shur, Y. L. and Pullman, E. R.: Abrupt increase in permafrost degradation in Arctic Alaska, Geophys. Res. Lett., 33(2), doi:10.1029/2005GL024960, 2006.

Jorgenson, M. T., Romanovsky, V., Harden, J., Shur, Y., O'Donnell, J., Schuur, E. A. G., Kanevskiy, M. and Marchenko, S.: Resilience and vulnerability of permafrost to climate change, Can. J. For. Res., 40(7), 1219–1236, doi:10.1139/X10-060, 2010.

Kade, A., Bret-Harte, M. S., Euskirchen, E. S., Edgar, C. and Fulweber, R. A.: Upscaling of CO_2 fluxes from heterogeneous tundra plant communities in Arctic Alaska, J. Geophys. Res., 117(G4), G04007, doi:10.1029/2012JG002065, 2012.

Kirtman, B., Power, S. B., Adedoyin, J. A., Boer, G. J., Bojariu, R., Camilloni, I., Doblas-Reyes, F. J., Fiore, A. M., Kimoto, M., Meehl, G. A., Prather, M., Sarr, A., Schär, C., Sutton, R., van Oldenborgh, G. J., Vecchi, G. and Wang, H. J.: Near-term Climate Change: Projections and Predictability (Chapter 11). In: Climate Change 2013: The Physical Science Basis. Contribution of Working Group I to the Fifth Assessment Report of the Intergovernmental Panel on Climate Change, Cambridge University Press, 2013.

Kittler, F., Heimann, M., Kolle, O., Zimov, N., Zimov, S. and Göckede, M.: Long-Term Drainage Reduces CO_2 Uptake and CH_4 Emissions in a Siberian Permafrost Ecosystem, Global Biogeochem. Cycles, 31(12), 1704–1717, doi:10.1002/2017GB005774, 2017.

Knoblauch, C., Spott, O., Evgrafova, S., Kutzbach, L. and Pfeiffer, E. M.: Regulation of methane production, oxidation, and emission by vascular plants and bryophytes in ponds of the northeast Siberian polygonal tundra, J. Geophys. Res. G Biogeosciences, 120(12), 2525–2541, doi:10.1002/2015JG003053, 2015.

Kong, A. Y. Y., Six, J., Bryant, D. C., Denison, R. F. and van Kessel, C. .: The Relationship between Carbon Input, Aggregation, and Soil Organic Carbon Stabilization in Sustainable Cropping Systems, Soil Sci. Soc. Am. J., 69(4), 1078–1085, doi:10.2136/sssaj2004.0215, 2005.

Kormann, R. and Meixner, F. X.: An analytical footprint model for non-neutral stratification, Boundary-Layer Meteorol., 99(2), 207–224, doi:10.1023/A:1018991015119, 2001.

Koven, C. D., Ringeval, B., Friedlingstein, P., Ciais, P., Cadule, P., Khvorostyanov, D., Krinner, G. and Tarnocai, C.: Permafrost carbon-climate feedbacks accelerate global warming, Proc. Natl. Acad. Sci., 108(36), 14769–14774, doi:10.1073/pnas.1103910108, 2011.

Kutzbach, L.: The Exchange of Energy, Water and Carbon Dioxide between Wet Arctic Tundra and the Atmosphere at the Lena River Delta, Northern Siberia, Doctoral Thesis, University of Hamburg, 2005.

Kutzbach, L., Wagner, D. and Pfeiffer, E. M.: Effect of microrelief and vegetation on methane emission from wet polygonal tundra, Lena Delta, Northern Siberia, Biogeochemistry, 69(3), 341–362, doi:10.1023/B:BIOG.0000031053.81520.db, 2004.

Kutzbach, L., Schneider, J., Sachs, T., Giebels, M., Nykänen, H., Shurpali, N. J., Martikainen, P. J., Alm, J. and

Wilmking, M.: CO_2 flux determination by closed-chamber methods can be seriously biased by inappropriate application of linear regression, Biogeosciences, 4(6), 1005–1025, doi:10.5194/bg-4-1005-2007, 2007a.

Kutzbach, L., Wille, C. and Pfeiffer, E.-M.: The exchange of CO_2 between wet arctic tundra and the atmosphere at the Lena River Delta, Northern Siberia, Biogeosciences, 4(5), 869–890, doi:10.5194/bg-4-869-2007, 2007b.

Kuzyakov, Y.: Priming effects: Interactions between living and dead organic matter, Soil Biol. Biochem., 42(9), 1363–1371, doi:10.1016/j.soilbio.2010.04.003, 2010.

Kwon, H. J., Oechel, W. C., Zulueta, R. C. and Hastings, S. J.: Effects of climate variability on carbon sequestration among adjacent wet sedge tundra and moist tussock tundra ecosystems, J. Geophys. Res., 111(3), G03014, doi:10.1029/2005JG000036, 2006.

Kwon, M. J., Beulig, F., Ilie, I., Wildner, M., Küsel, K., Merbold, L., Mahecha, M. D., Zimov, N., Zimov, S. A., Heimann, M., Schuur, E. A. G., Kostka, J. E., Kolle, O., Hilke, I. and Göckede, M.: Plants, microorganisms, and soil temperatures contribute to a decrease in methane fluxes on a drained Arctic floodplain, Glob. Chang. Biol., 23(6), 2396–2412, doi:10.1111/gcb.13558, 2017.

Lafleur, P. M., Humphreys, E. R., St. Louis, V. L., Myklebust, M. C., Papakyriakou, T., Poissant, L., Barker, J. D., Pilote, M. and Swystun, K. A.: Variation in peak growing season net ecosystem production across the Canadian arctic, Environ. Sci. Technol., 46(15), 7971–7977, doi:10.1021/es300500m, 2012.

Lai, D.: Methane Dynamics in Northern Peatlands: A Review, Pedosphere, 19(4), 409–421, doi:10.1016/S1002-0160(09)00003-4, 2009.

Lasslop, G., Reichstein, M., Papale, D., Richardson, A., Arneth, A., Barr, A., Stoy, P. and Wohlfahrt, G.: Separation of net ecosystem exchange into assimilation and respiration using a light response curve approach: Critical issues and global evaluation, Glob. Chang. Biol., 16(1), 187–208, doi:10.1111/j.1365-2486.2009.02041.x, 2010.

Laurila, T., Soegaard, H., Lloyd, C. R., Aurela, M., Tuovinen, J. P. and Nordstroem, C.: Seasonal variations of net CO_2 exchange in European Arctic ecosystems, Theor. Appl. Climatol., 70(1–4), 183–201, doi:10.1007/s007040170014, 2001.

Leclerc, M. Y. and Foken, T.: Footprints in Micrometeorology and Ecology, 1st ed., Springer., 2014.

Lee, H., Schuur, E. A. G., Inglett, K. S., Lavoie, M. and Chanton, J. P.: The rate of permafrost carbon release under aerobic and anaerobic conditions and its potential effects on climate, Glob. Chang. Biol., 18(2), 515–527, doi:10.1111/j.1365-2486.2011.02519.x, 2012.

LI-COR Biosciences: Open-source software EddyPro, accessed 13th March 2016 [online] available from: www.licor.com/eddypro, 2016.

Liebner, S., Harder, J. and Wagner, D.: Bacterial diversity and community structure in polygonal tundra soils from Samoylov Island, Lena Delta, Siberia, Int. Microbiol., 11(3), 195–202, doi:10.2436/20.1501.01.60, 2008.

Liebner, S., Zeyer, J., Wagner, D., Schubert, C., Pfeiffer, E. M. and Knoblauch, C.: Methane oxidation associated with submerged brown mosses reduces methane emissions from Siberian polygonal tundra, J. Ecol., 99(4), 914–922, doi:10.1111/j.1365-2745.2011.01823.x, 2011.

Long, K. D., Flanagan, L. B. and Cai, T.: Diurnal and seasonal variation in methane emissions in a northern Canadian peatland measured by eddy covariance, Glob. Chang. Biol., 16(9), 2420–2435, doi:10.1111/j.1365-2486.2009.02083.x, 2010.

López-Blanco, E., Lund, M., Williams, M., Tamstorf, M. P., Westergaard-Nielsen, A., Exbrayat, J. F., Hansen, B. U. and Christensen, T. R.: Exchange of CO_2 in Arctic tundra: Impacts of meteorological variations and biological disturbance, Biogeosciences, 14(19), 4467–4483, doi:10.5194/bg-14-4467-2017, 2017.

Loranty, M. M., Goetz, S. J. and Beck, P. S. A.: Tundra vegetation effects on pan-Arctic albedo, Env. Res. Lett., 6(2), doi:10.1088/1748-9326/6/2/024014, 2011.

Lüers, J., Westermann, S., Piel, K. and Boike, J.: Annual CO_2 budget and seasonal CO_2 exchange signals at a high Arctic permafrost site on Spitsbergen, Svalbard archipelago, Biogeosciences, 11(22), 6307–6322, doi:10.5194/bg-11-6307-2014, 2014.

Lund, M., Falk, J. M., Friborg, T., Mbufong, H. N., Sigsgaard, C., Soegaard, H. and Tamstorf, M. P.: Trends in CO_2 exchange in a high Arctic tundra heath, 2000-2010, J. Geophys. Res., 117(G2), G02001, doi:10.1029/2011JG001901, 2012.

Luo, Y. and Zhou, X.: Soil Respiration and the Environment, Academic Press, 2006.

Mahecha, M. D., Reichstein, M., Carvalhais, N., Lasslop, G., Lange, H., Seneviratne, S. I., Vargas, R., Ammann, C., Arain, M. A., Cescatti, A., Janssens, I. A., Migliavacca, M., Montagnani, L. and Richardson, A. D.: Global convergence in the temperature sensitivity of respiration at ecosystem level, Sci. (New York), 329(5993), 838–840, doi:10.1126/science.1189587, 2010.

Marushchak, M. E., Kiepe, I., Biasi, C., Elsakov, V., Friborg, T., Johansson, T., Soegaard, H., Virtanen, T. and Martikainen, P. J.: Carbon dioxide balance of subarctic tundra from plot

to regional scales, Biogeosciences, 10(1), 437–452, doi:10.5194/bg-10-437-2013, 2013.

Marushchak, M. E., Friborg, T., Biasi, C., Herbst, M., Johansson, T., Kiepe, I., Liimatainen, M., Lind, S. E., Martikainen, P. J., Virtanen, T., Soegaard, H. and Shurpali, N. J.: Methane dynamics in the subarctic tundra: combining stable isotope analyses, plot- and ecosystem-scale flux measurements, Biogeosciences, 13(2), 597–608, doi:10.5194/bg-13-597-2016, 2016.

Masson-Delmotte, V., Schulz, M., Abe-Ouchi, A., Beer, J., Ganopolski, A., González Rouco, J. F., Jansen, E., Lambeck, K., Luterbacher, J., Naish, T., Osborn, T., Otto-Bliesner, B., Quinn, T., Ramesh, R., Rojas, M., Shao, X. and Timmermann, A.: Information from Paleoclimate Archives (Chapter 5). In: Climate Change 2013: The Physical Science Basis. Contribution of Working Group I to the Fifth Assessment Report of the Intergovernmental Panel on Climate Change, Cambridge University Press. [online] available from: http://www.ipcc.ch/report/ar5/wg1, 2013.

Mastepanov, M., Sigsgaard, C., Dlugokencky, E. J., Houweling, S., Ström, L., Tamstorf, M. P. and Christensen, T. R.: Large tundra methane burst during onset of freezing., Nature, 456(7222), 628–30, doi:10.1038/nature07464, 2008.

Mastepanov, M., Sigsgaard, C., Tagesson, T., Ström, L., Tamstorf, M. P., Lund, M. and Christensen, T. R.: Revisiting factors controlling methane emissions from high-Arctic tundra, Biogeosciences, 10(11), 5139–5158, doi:10.5194/bg-10-5139-2013, 2013.

Matthes, J. H., Sturtevant, C., Verfaillie, J., Knox, S. and Baldocchi, D.: Parsing the variability in CH_4 flux at a spatially heterogeneous wetland: Integrating multiple eddy covariance towers with high-resolution flux footprint analysis, J. Geophys. Res. G Biogeosciences, 119(7), 1322–1339, doi:10.1002/2014JG002642, 2014.

Mbufong, H. N., Lund, M., Aurela, M., Christensen, T. R., Eugster, W., Friborg, T., Hansen, B. U., Humphreys, E. R., Jackowicz-Korczynski, M., Kutzbach, L., Lafleur, P. M., Oechel, W. C., Parmentier, F. J. W., Rasse, D. P., Rocha, A. V., Sachs, T., van der Molen, M. M. and Tamstorf, M. P.: Assessing the spatial variability in peak season CO_2 exchange characteristics across the Arctic tundra using a light response curve parameterization, Biogeosciences, 11(17), 4897–4912, doi:10.5194/bg-11-4897-2014, 2014.

McEwing, K. R., Fisher, J. P. and Zona, D.: Environmental and vegetation controls on the spatial variability of CH_4 emission from wet-sedge and tussock tundra ecosystems in the Arctic, Plant Soil, 388(1–2), 37–52, doi:10.1007/s11104-014-2377-1, 2015.

McGuire, A. D., Anderson, L. G., Christensen, T. R., Dallimore, S., Guo, L. D., Hayes, D. J., Heimann, M., Lorenson, T. D., Macdonald, R. W. and Roulet, N.: Sensitivity of the carbon cycle in the Arctic to climate change, Ecol. Monogr., 79(4), 523–555, doi:10.1890/08-2025.1, 2009.

McGuire, A. D., Christensen, T. R., Hayes, D., Heroult, A., Euskirchen, E., Kimball, J. S., Koven, C., Lafleur, P., Miller, P. A., Oechel, W., Peylin, P., Williams, M. and Yi, Y.: An assessment of the carbon balance of Arctic tundra: Comparisons among observations, process models, and atmospheric inversions, Biogeosciences, 9(8), 3185–3204, doi:10.5194/bg-9-3185-2012, 2012.

Megonigal, J. P., Hines, M. E. and Visscher, P. T.: Anaerobic Metabolism: Linkages to Trace Gases and Aerobic Processes, edited by W. H. Schlesinger, H. D. Holland, and K. K. Turekian, Elsevier-Pergamon., 2004.

Merbold, L., Kutsch, W. L., Corradi, C., Kolle, O., Rebmann, C., Stoy, P. C., Zimov, S. a. and Schulze, E.-D.: Artificial drainage and associated carbon fluxes (CO_2/CH_4) in a tundra ecosystem, Glob. Chang. Biol., 15(11), 2599–2614, doi:10.1111/j.1365-2486.2009.01962.x, 2009.

Michalies, L. and Menten, M. L.: Die Kinetik der Invertinwirkung, Biochem. Z., 49, 333–369, 1913.

Minkkinen, K., Ojanen, P., Penttilä, T., Aurela, M., Laurila, T., Tuovinen, J. P. and Lohila, A.: Persistent carbon sink at a boreal drained bog forest, Biogeosciences, 15(11), 3603–3624, doi:10.5194/bg-15-3603-2018, 2018.

Moffat, A. M., Papale, D., Reichstein, M., Hollinger, D. Y., Richardson, A. D., Barr, A. G., Beckstein, C., Braswell, B. H., Churkina, G., Desai, A. R., Falge, E., Gove, J. H., Heimann, M., Hui, D., Jarvis, A. J., Kattge, J., Noormets, A. and Stauch, V. J.: Comprehensive comparison of gap-filling techniques for eddy covariance net carbon fluxes, Agric. For. Meteorol., 147(3–4), 209–232, doi:10.1016/j.agrformet.2007.08.011, 2007.

van der Molen, M. K., van Huissteden, J., Parmentier, F. J. W., Petrescu, A. M. R., Dolman, A. J., Maximov, T. C., Kononov, A. V., Karsanaev, S. V. and Suzdalov, D. A.: The growing season greenhouse gas balance of a continental tundra site in the Indigirka lowlands, NE Siberia, Biogeosciences, 4(6), 985–1003, doi:10.5194/bg-4-985-2007, 2007.

Moncrieff, J. B., Clement, R., Finnigan, J. and Meyers, T.: Averaging, detrending and filtering of eddy covariance time series, in Handbook of Micrometeorology: a guide for surface flux measurements, edited by X. Lee, W. J. Massman, and B. E. Law, Kluwer Academic., 2004.

Morgenstern, A., Röhr, C., Grosse, G. and Grigoriev, M. N.: The Lena River Delta - inventory of lakes and geomor-

phological terraces, accessed 24th Oct. 2016, [online] available from: https://doi.pangaea.de/10.1594/PANGAEA.758728, 2011.

Morin, T. H., Bohrer, G., Stefanik, K. C., Rey-Sanchez, A. C., Matheny, A. M. and Mitsch, W. J.: Combining eddy-covariance and chamber measurements to determine the methane budget from a small, heterogeneous urban floodplain wetland park, Agric. For. Meteorol., 237–238, 160–170, doi:10.1016/j.agrformet.2017.01.022, 2017.

Murray, K. J., Tenhunen, J. D. and Nowak, R. S.: Photoinhibition as a control on photosynthesis and production of Sphagnum mosses, Oecologia, 96(2), 200–207, doi:10.1007/BF00317733, 1993.

Muster, S., Langer, M., Heim, B., Westermann, S. and Boike, J.: Subpixel heterogeneity of ice-wedge polygonal tundra: a multi-scale analysis of land cover and evapotranspiration in the Lena River Delta, Siberia, Tellus B, 64, 1–19, doi:10.3402/tellusb.v64i0.17301, 2012.

Myers-Smith, I. H., Forbes, B. C., Wilmking, M., Hallinger, M., Lantz, T., Blok, D., Tape, K. D., MacIas-Fauria, M., Sass-Klaassen, U., Lévesque, E., Boudreau, S., Ropars, P., Hermanutz, L., Trant, A., Collier, L. S., Weijers, S., Rozema, J., Rayback, S. A., Schmidt, N. M., Schaepman-Strub, G., Wipf, S., Rixen, C., Ménard, C. B., Venn, S., Goetz, S., Andreu-Hayles, L., Elmendorf, S., Ravolainen, V., Welker, J., Grogan, P., Epstein, H. E. and Hik, D. S.: Shrub expansion in tundra ecosystems: Dynamics, impacts and research priorities, Env. Res. Lett., 6(4), 045509, doi:10.1088/1748-9326/6/4/045509, 2011.

Myhre, G., Shindell, D., Bréon, F.-M., Collins, W., Fuglestvedt, J., Huang, J., Koch, D., Lamarque, J.-F., Lee, D., Mendoza, B., Nakajima, T., Robock, A., Stephens, G., Takemura, T. and Zhang, H.: Anthropogenic and Natural Radiative Forcing (Chapter 8). In: Climate Change 2013: The Physical Science Basis. Contribution of Working Group I to the Fifth Assessment Report of the Intergovernmental Panel on Climate Change, Cambridge University Press. [online] available from: http://www.ipcc.ch/report/ar5/wg1, 2013.

NASA: Global temperature anomalies estmiated with GISS surface temperature analysis data including ship and buoy data from the Hadley Centre (Robert Simmon), accessed 12th December 2017, [online] available from: https://earthobservatory.nasa.gov/IOTD/view.php?id=81214, 2013.

NOAA: The NOAA annual greenhouse gas index (Butler, J.H.,Montzka, S.A.), accessed 9th Sept. 2016, [online] available from: http://www.esrl.noaa.gov/gmd/ aggi/aggi.html, 2016.

NOAA: Global Greenhouse Gas Reference Network, Trends in Atmospheric Carbon Dioxide, accessed 14th

January 2018, [online] available from: https://www.esrl.noaa.gov/gmd/ccgg/trends/, 2018a.

NOAA: Global Greenhouse Gas Reference Network, Trends in Atmospheric Methane, accessed 14th January 2018, [online] available from: https://www.esrl.noaa.gov/gmd/ccgg/trends_ch4/, 2018b.

Oberbauer, S. F. and Oechel, W. C.: Maximum CO_2-assimilation rates of vascular plants on an Alaskan arctic tundra slope, Ecography (Cop.)., 12(3), 312–316, doi:10.1111/j.1600-0587.1989.tb00851.x, 1989.

Obu, J., Westermann, S., Kääb, A. and Bartsch, A.: Ground Temperature Map, 2000-2016, Northern Hemisphere Permafrost. Alfred Wegener Institute for Polar and Marine Research, PANGAEA, doi:10.1594/pangaea.888600, 2018.

Oechel, W.: Seasonal patterns of temperature response of CO_2 flux and acclimation in Arctic mosses growing in situ, Photosynthetica, 10, 447–456 [online] available from: http://agris.fao.org/agris-search/search.do?recordID=US201301254787, 1976.

Oechel, W. C., Hastings, S. J., Vourlitis, L., Jenkins, M., Riechers, G. and Grulke, N.: Recent change of Arctic tundra ecosystems from a net carbon dioxide sink to a source, Nature, 361, 520–523, doi:10.1038/364706a0, 1993.

Oechel, W. C., Callaghan, T., Gilmanov, T., Holten, J. I., Maxwell, B., Molau, U. and Sveinbjörnsson, B.: Global Change and Arctic Terrestrial Ecosystems, Springer, New York., 1997.

Oechel, W. C., Vourlitis, G. L., Brooks, S., Crawford, T. L. and Dumas, E.: Intercomparison among chamber, tower, and aircraft net CO_2 and energy fluxes measured during the Arctic System Science Land-Atmosphere-Ice Interactions (ARCSS-LAII) flux study, J. Geophys. Res. Atmos., 103(D22), 28993–29003, doi:10.1029/1998JD200015, 1998.

Oechel, W. C., Laskowski, C. A., Burba, G., Gioli, B. and Kalhori, A. A. M.: Annual patterns and budget of CO_2 flux in an Arctic tussock tundra ecosystem, J. Geophys. Res. Biogeosciences, 119(3), 323–339, doi:10.1002/2013JG002431, 2014.

Oke, T. R.: Boundary Layer Climates, 2nd ed., Methuen & Co. Ltd., 1987.

Olefeldt, D., Turetsky, M. R., Crill, P. M. and McGuire, A. D.: Environmental and physical controls on northern terrestrial methane emissions across permafrost zones., Glob. Chang. Biol., 19(2), 589–603, doi:10.1111/gcb.12071, 2013.

ORNL: MODIS and VIIRS Land Products Global Subsetting and Visualisation Tool. Oak Ridge National Laboratory, Tennessee, USA, accessed 13th March 2017, doi:10.3334/ORNL DAAC/1379, 2017.

Osterkamp, T. E.: Sub-sea permafrost, in Encyclopedia of Ocean Sciences, edited by J. H. Steele, S. A. Thorpe, and K. K. Turekian, pp. 2902–12, Academic Press, 2001.

Parmentier, F. J. W., Van Der Molen, M. K., Van Huissteden, J., Karsanaev, S. A., Kononov, A. V., Suzdalov, D. A., Maximov, T. C. and Dolman, A. J.: Longer growing seasons do not increase net carbon uptake in the northeastern Siberian tundra, J. Geophys. Res. Biogeosciences, 116(G4), G04013, doi: 10.1029/2011JG001653, 2011a.

Parmentier, F. J. W., Van Huissteden, J., Kip, N., Op Den Camp, H. J. M., Jetten, M. S. M., Maximov, T. C. and Dolman, A. J.: The role of endophytic methane-oxidizing bacteria in submerged Sphagnum in determining methane emissions of Northeastern Siberian tundra, Biogeosciences, 8(5), 1267–1278, doi:10.5194/bg-8-1267-2011, 2011b.

Patankar, R., Mortazavi, B., Oberbauer, S. F. and Starr, G.: Diurnal patterns of gas-exchange and metabolic pools in tundra plants during three phases of the arctic growing season, Ecol. Evol., 3(2), 375–388, doi:10.1002/ece3.467, 2013.

Pearson, R. G., Phillips, S. J., Loranty, M. M., Beck, P. S. A., Damoulas, T., Knight, S. J. and Goetz, S. J.: Shifts in Arctic vegetation and associated feedbacks under climate change, Nat. Clim. Chang., 3(7), 673–677, doi:10.1038/nclimate1858, 2013.

Peichl, M., Sonnentag, O. and Nilsson, M. B.: Bringing Color into the Picture: Using Digital Repeat Photography to Investigate Phenology Controls of the Carbon Dioxide Exchange in a Boreal Mire, Ecosystems, 18(1), 115–131, doi: 10.1007/s10021-014-9815-z, 2014.

Petersen, S.: Export von gelösten Nährelementen und gelöster organischer Substanz im Abfluss eines Tundra-Einzugsgebietes, Lena Delta, Sibirien, Master thesis, University of Hamburg, 2015.

Pirk, N., Sievers, J., Mertes, J., Parmentier, F.-J. W., Mastepanov, M. and Christensen, T. R.: Spatial variability of CO_2 uptake in polygonal tundra: assessing low-frequency disturbances in eddy covariance flux estimates, Biogeosciences, 14, 3157–3169, doi: 10.5194/bg-14-3157-2017, 2017.

Plug, L. J. and West, J. J.: Thaw lake expansion in a two-dimensional coupled model of heat transfer, thaw subsidence, and mass movement, J. Geophys. Res., 114(1), doi:10.1029/2006JF000740, 2009.

Pogoda i Klimat: Climate Tiksi, accessed 8th May 2016, [online] available from: http://www.pogodaiklimat.ru/climate/21824.htm, 2016.

Räisänen, J.: CO_2-Induced Climate Change in CMIP2 Experiments: Quantification of Agreement and Role of Internal Variability, J. Clim., 14(9), 2088–2104, doi:10.1175/1520-0442(2001)014<2088:CICCIC>2.0.CO;2, 2001.

Raz-Yaseef, N., Torn, M. S., Wu, Y., Billesbach, D. P., Liljedahl, A. K., Kneafsey, T. J., Romanovsky, V. E., Cook, D. R. and Wullschleger, S. D.: Large CO_2 and CH_4 emissions from polygonal tundra during spring thaw in northern Alaska, Geophys. Res. Lett., 44(1), 504–513, doi:10.1002/2016GL071220, 2017.

Reeburgh, W. S., Whalen, S. C. and Alperin, M. J.: The role of methylotrophy in the global methane budget, in Microbial growth on C1 compounds, edited by J. C. Murrell and D. P. Kelly, pp. 1–14, Intercept Press, Andover., 1993.

Reichstein, M., Falge, E., Baldocchi, D., Papale, D., Aubinet, M., Berbigier, P., Bernhofer, C., Buchmann, N., Gilmanov, T., Granier, A., Grünwald, T., Havránková, K., Ilvesniemi, H., Janous, D., Knohl, A., Laurila, T., Lohila, A., Loustau, D., Matteucci, G., Meyers, T., Miglietta, F., Ourcival, J. M., Pumpanen, J., Rambal, S., Rotenberg, E., Sanz, M., Tenhunen, J., Seufert, G., Vaccari, F., Vesala, T., Yakir, D. and Valentini, R.: On the separation of net ecosystem exchange into assimilation and ecosystem respiration: Review and improved algorithm, Glob. Chang. Biol., 11(9), 1424–1439, doi:10.1111/j.1365-2486.2005.001002.x, 2005.

Rhein, M., Rintoul, S. R., Aoki, S., Campos, E., Chambers, D., Feely, R. A., Gulev, S., Johnson, G. C., Josey, S. A., Kostianoy, A., Mauritzen, C., Roemmich, D., Talley, L. D. and Wang, F.: Observations: Ocean (Chapter 3). In: Climate Change 2013: The Physical Science Basis. Contribution of Working Group I to the Fifth Assessment Report of the Intergovernmental Panel on Climate Change, Cambridge University Press, 2013.

Richardson, A. D.: PhenoCam, accessed 1rst June 2016 [online] available from: https://phenocam.sr.unh.edu/webcam/tools/, 2012.

Rinne, J., Riutta, T., Pihlatie, M., Aurela, M., Haapanala, S., Tuovinen, J.-P., Tuittila, E.-S. and Vesala, T.: Annual cycle of methane emission from a boreal fen measured by the eddy covariance technique, Tellus B, 59(3), 449–457, doi:10.1111/j.1600-0889.2007.00261.x, 2007.

Romanovsky, V. E., Drozdov, D. S., Oberman, N. G., Malkova, G. V., Kholodov, A. L., Marchenko, S. S., Moskalenko, N. G., Sergeev, D. O., Ukraintseva, N. G., Abramov, A. A., Gilichinsky, D. A. and Vasiliev, A. A.: Thermal state of permafrost in Russia,

Permafr. Periglac. Process., 21(2), 136–155, doi:10.1002/ppp.683, 2010.

Ruimy, A., Jarvis, P. G., Baldocchi, D. D. and Saugier, B.: CO_2 Fluxes over Plant Canopies and Solar Radiation: A Review, Adv. Ecol. Res., 26, 1–68, doi:10.1016/S0065-2504(08)60063-X, 1995.

Runkle, B. R. K., Sachs, T., Wille, C., Pfeiffer, E. M. and Kutzbach, L.: Bulk partitioning the growing season net ecosystem exchange of CO_2 in Siberian tundra reveals the seasonality of it carbon sequestration strength, Biogeosciences, 10(3), 1337–1349, doi:10.5194/bg-10-1337-2013, 2013.

Sachs, T., Wille, C., Boike, J. and Kutzbach, L.: Environmental controls on ecosystem-scale CH_4 emission from polygonal tundra in the Lena River Delta, Siberia, J. Geophys. Res., 113(G3), G00A03, doi:10.1029/2007JG000505, 2008.

Sachs, T., Giebels, M., Boike, J. and Kutzbach, L.: Environmental controls on CH_4 emission from polygonal tundra on the microsite scale in the Lena river delta, Siberia, Glob. Chang. Biol., 16(11), 3096–3110, doi:10.1111/j.1365-2486.2010.02232.x, 2010.

Salmon, V. G., Soucy, P., Mauritz, M., Celis, G., Natali, S. M., Mack, M. C. and Schuur, E. A. G.: Nitrogen availability increases in a tundra ecosystem during five years of experimental permafrost thaw, Glob. Chang. Biol., 22(5), 1927–1941, doi:10.1111/gcb.13204, 2016.

Schmid, H. P. and Lloyd, C. R.: Spatial representativeness and the location bias of flux footprints over inhomogeneous areas, Agric. For. Meteorol., 93(3), 195–209, doi:10.1016/S0168-1923(98)00119-1, 1999.

Schneider, J., Grosse, G. and Wagner, D.: Land cover classification of tundra environments in the Arctic Lena Delta based on Landsat 7 ETM+ data and its application for upscaling of methane emissions, Remote Sens. Environ., 113(2), 380–391, doi:10.1016/j.rse.2008.10.013, 2009.

Schütz, H., Schröder, P. and Rennenberg, H.: Role of plants in regulating the methane flux to the atmosphere, in Trace Gas Emissions by Plants, edited by T. D. Sharkey, E. A. Holland, and H. A. Mooney, pp. 29–63, Academic Press, San Diego, 1991.

Schuur, E. A. G., Bockheim, J., Canadell, J. G., Euskirchen, E., Field, C. B., Goryachkin, S. V., Hagemann, S., Kuhry, P., Lafleur, P. M., Lee, H., Mazhitova, G., Nelson, F. E., Rinke, A., Romanovsky, V. E., Shiklomanov, N., Tarnocai, C., Venevsky, S., Vogel, J. G. and Zimov, S. A.: Vulnerability of Permafrost Carbon to Climate Change: Implications for the Global Carbon Cycle, Bioscience, 58(8), 701–714, doi:10.1641/B580807, 2008.

Schuur, E. A. G., McGuire, A. D., Schädel, C., Grosse, G., Harden, J. W., Hayes, D. J., Hugelius, G., Koven, C. D., Kuhry, P., Lawrence, D. M., Natali, S. M., Olefeldt, D., Roma-

novsky, V. E., Schaefer, K., Turetsky, M. R. and Vonk, J. E.: Climate change and the permafrost carbon feedback, Nature, 520(7546), 171–179, doi:10.1038/nature14338, 2015.

Schwamborn, G., Rachold, V. and Grigoriev, M. N.: Late Quaternary sedimentation history of the Lena Delta, Quat. Int., 89(1), 119–134, doi:10.1016/S1040-6182(01)00084-2, 2002.

Sebacher, D. I., Harriss, R. C. and Bartlett, K. B.: Methane emission to the atmosphere through aquatic plants, J. Environ. Qual., 14, 40–46, doi:10.2134/jeq1985.00472425001400010008x, 1985.

Serreze, M. C., Walsh, J. E., Chapin, F. S. I., Osterkamp, T., Dyurgerov, M., Romanovsky, V., Oechel, W. C., Morison, J., Zhang, T. and Barry, R. G.: Observational evidence of recent change in the northern high- latitude environment, Clim. Change, 46(1–2), 159–207, doi:10.1023/A:1005504031923, 2000.

Shaver, G. R., Laundre, A. J., Giblin, A. E. and Nadelhoffer, K. J.: Changes in Live Plant Biomass, Primary Production and Species Composition along a Riverside Toposequence in Arctic Alaska, USA, Arct. Alp. Res., 28(3), 363–379, doi:10.2307/1552116, 1996a.

Shaver, G. R., Giblin, A. E., Nadelhoffer, K. J. and Rastetter, E. B.: Plant functional types and ecosystem change in arctic tundras, in Plant Functional Types, edited by T. Smith, H. Shugart, and I. Woodward, Cambridge University Press, 1996b.

Shaver, G. R., Street, L. E., Rastetter, E. B., Van Wijk, M. T. and Williams, M.: Functional convergence in regulation of net CO_2 flux in heterogeneous tundra landscapes in Alaska and Sweden, J. Ecol., 95(4), 802–817, doi:10.1111/j.1365-2745.2007.01259.x, 2007.

Smith, L. C., Sheng, Y., MacDonald, G. M. and Hinzman, L. D.: Disappearing Arctic lakes, Science, 308 (5727), 1429, doi:10.1126/science.1108142, 2005.

Sommerkorn, M., Bölter, M. and Kappen, L.: Carbon dioxide fluxes of soils and mosses in wet tundra of Taimyr Peninsula, Siberia: Controlling factors and contribution to net system fluxes, Polar Res., 18(2), 253–260, doi:10.3402/polar.v18i2.6582, 1999.

Sonnentag, O., Hufkens, K., Teshera-Sterne, C., Young, A. M., Friedl, M., Braswell, B. H., Milliman, T., O'Keefe, J. and Richardson, A. D.: Digital repeat photography for phenological research in forest ecosystems, Agric. For. Meteorol., 152(1), 159–177, doi:10.1016/j.agrformet.2011.09.009, 2012.

Stocker, T. F., Qin, D., Plattner, G.-K., Alexander, L. V., Allen, S. K., Bindoff, N. L., Bréon, F.-M., Church, J. A., Cubasch, U., Emori, S., Forster, P., Friedlingstein, P., Gillett, N., Gregory, J. M., Hartmann, D. L.,

Jansen, E., Kirtman, B., Knutti, R., Krishna Kumar, K., Lemke, P., Marotzke, J., Masson-Delmotte, V., Meehl, G. A., Mokhov, I. I., Piao, S., Ramaswamy, V., Randall, D., Rhein, M., Rojas, M., Sabine, C., Shindell, D., Talley, L. D., Vaughan, D. G. and Xie, S.-P.: Technical Summary. In: Climate Change 2013: The Physical Science Basis. Contribution of Working Group I to the Fifth Assessment Report of the Intergovernmental Panel on Climate Change, Cambridge University Press, 2013.

Stow, D. A., Hope, A., McGuire, D., Verbyla, D., Gamon, J., Huemmrich, F., Houston, S., Racine, C., Sturm, M., Tape, K., Hinzman, L., Yoshikawa, K., Tweedie, C., Noyle, B., Silapaswan, C., Douglas, D., Griffith, B., Jia, G., Epstein, H., Walker, D., Daeschner, S., Petersen, A., Zhou, L. and Myneni, R.: Remote sensing of vegetation and land-cover change in Arctic Tundra Ecosystems, Remote Sens. Environ., 89(3), 281–308, doi:10.1016/j.rse.2003.10.018, 2004.

Stoy, P. C., Williams, M., Evans, J. G., Prieto-Blanco, A., Disney, M., Hill, T. C., Ward, H. C., Wade, T. J. and Street, L. E.: Upscaling Tundra CO_2 Exchange from Chamber to Eddy Covariance Tower, Arctic, Antarct. Alp. Res., 45(2), 275–284, doi:10.1657/1938-4246-45.2.275, 2013.

Ström, L., Ekberg, A., Mastepanov, M. and Christensen, T. R.: The effect of vascular plants on carbon turnover and methane emissions from a tundra wetland, Glob. Chang. Biol., 9(8), 1185–1192, doi:10.1046/j.1365-2486.2003.00655.x, 2003.

Tagesson, T., Mölder, M., Mastepanov, M., Sigsgaard, C., Tamstorf, M. P., Lund, M., Falk, J. M., Lindroth, A., Christensen, T. R. and Ström, L.: Land-atmosphere exchange of methane from soil thawing to soil freezing in a high-Arctic wet tundra ecosystem, Glob. Ch. Biol., 18(6), 1928–1940, doi:10.1111/j.1365-2486.2012.02647.x, 2012.

Tarnocai, C., Canadell, J. G., Schuur, E. G., Kuhry, P., Mazhitova, G. and Zimov, S.: Soil organic carbon pools in the northern circumpolar permafrost region, Global Biogeoch. Cycles, 23(2), doi:10.1029/2008GB003327, 2009.

Tennekes, H. and Lumley, J. L.: A first course in turbulence, Massachusetts Institute of Technology., 1972.

Tieszen, L. L.: CO_2 exchanges in the Alaskan arctic tundra: seasonal changes in the rate of photosynthesis of four species, Photosynthetica, 9, 376–390 [online] available from: http://agris.fao.org/agris-search/search.do?recordID=US201303022075, 1975.

Tsuyuzaki, S., Nakano, T., Kuniyoshi, S. I. and Fukuda, M.: Methane flux in grassy marshlands near Kolyma River, north-eastern Siberia, Soil Biol. Biochem., 33(10), 1419–1423, doi:10.1016/S0038-0717(01)00058-X, 2001.

Turetsky, M. R., Bond-Lamberty, B., Euskirchen, E., Talbot, J., Frolking, S., McGuire, A. D. and Tuittila, E. S.: The resilience and functional role of moss in boreal and arctic ecosystems, New Phytol., 196(1), 49–67, doi:10.1111/j.1469-8137.2012.04254.x, 2012.

van't Hoff, J. H.: Lectures on Theoretical and Physical Chemistry, Part 1: Chemical Dynamics, Edward Arnold, London, 224–229, 1898.

Vaughan, D. G., Comiso, J. C., Allison, I., Carrasco, J., Kaser, G., Kwok, R., Mote, P., Murray, T., Paul, F., Ren, J., Rignot, E., Solomina, O., Steffen, K. and Zhang, T.: Observations: Cryosphere (Chapter 4). In: Climate Change 2013: The Physical Science Basis. Contribution of Working Group I to the Fifth Assessment Report of the Intergovernmental Panel on Climate Change, Cambridge University Press, 2013.

Vaughn, L. J. S., Conrad, M. E., Bill, M. and Torn, M. S.: Isotopic insights into methane production, oxidation, and emissions in Arctic polygon tundra, Glob. Ch. Biol., 22(10), 3487–3502, doi:10.1111/gcb.13281, 2016.

Wagner, D., Gattinger, A., Embacher, A., Pfeiffer, E.-M., Schloter, M. and Lipski, A.: Methanogenic activity and biomass in Holocene permafrost deposits of the Lena Delta, Siberian Arctic and its implication for the global methane budget, Glob. Chang. Biol., 13(5), 1089–1099, doi:10.1111/j.1365-2486.2007.01331.x, 2007.

Walter, K. M., Zimov, S. A., Chanton, J. P., Verbyla, D. and Chapin III, F. S.: Methane bubbling from Siberian thaw lakes as a positive feedback to climate warming, Nature, 443(7107), 71–75, doi:10.1038/nature05040, 2006.

Walz, J., Knoblauch, C., Böhme, L. and Pfeiffer, E. M.: Regulation of soil organic matter decomposition in permafrost-affected Siberian tundra soils - Impact of oxygen availability, freezing and thawing, temperature, and labile organic matter, Soil Biol. Biochem., 110, 34–43, doi:10.1016/j.soilbio.2017.03.001, 2017.

Webb, E. K., Pearman, G. I. and Leuning, R.: Correction of flux measurements for density effects due to heat and water vapour transfer, Q. J. R. Meteorol. Soc., 106, 85–100, doi:10.1002/qj.49710644707, 1980.

Whalen, C. and Reeburgh, W. S.: Interannual variations in tundra methane emission: a 4-year time series at fixed sites, Global Biogeochem. Cycles, 6(2), 139–159, doi:10.1029/92GB00430, 1992.

Whalen, S. C.: Biogeochemistry of Methane Exchange between Natural Wetlands and the Atmosphere, Environ. Eng. Sci., 22(1), 73–94, doi:10.1089/ees.2005.22.73, 2005.

Whalen, S. C., Reeburgh, W. S. and Kizer, K. S.: Methane consumption and emission by Taiga, Global Biogeochem. Cycles, 5(3), 261–273, doi:10.1029/91GB01303, 1991.

Wielgolaski, F. E.: Fennoscandian Tundra Ecosystems: Part 1 Plants and Microorganisms, Springer Science & Business Media, 2012.

Wille, C., Kutzbach, L., Sachs, T., Wagner, D. and Pfeiffer, E.-M.: Methane emission from Siberian arctic polygonal tundra: eddy covariance measurements and modeling, Glob. Ch. Biol., 14(6), 1395–1408, doi:10.1111/j.1365-2486.2008.01586.x, 2008.

Williams, M., Rastetter, E. B., Van der Pol, L. and Shaver, G. R.: Arctic canopy photosynthetic efficiency enhanced under diffuse light, linked to a reduction in the fraction of the canopy in deep shade, New Phytol., 202(4), 1267–1276, doi:10.1111/nph.12750, 2014.

Yang, D.: Siberian Lena River hydrologic regime and recent change, J. Geophys. Res., 107(D23), 4694, doi:10.1029/2002JD002542, 2002.

Yershov, D. E.: General Geocryology, (in Russian), University Press, Cambridge, 1998.

Zamolodchikov, D. G., Karelin, D. V., Ivaschenko, A. I., Oechel, W. C. and Hastings, S. J.: CO_2 flux measurements in Russian Far East tundra using eddy covariance and closed chamber techniques, Tellus B, 55(4), 879–892, doi:10.3402/tellusb.v55i4.16384, 2003.

Zhang, T.: Influence of seasonal snow cover on the ground thermal regime: an overview, Rev. Geophys., 43, doi:10.1029/2004RG000157, 2005.

Zhang, T., Heginbottom, J. A., Barry, R. G. and Brown, J.: Further statistics on the distribution of permafrost and ground ice in the Northern Hemisphere, Polar Geogr., 24(2), 126–131, doi:10.1080/10889370009377692, 2000.

Zhang, Y., Sachs, T., Li, C. and Boike, J.: Upscaling methane fluxes from closed chambers to eddy covariance based on a permafrost biogeochemistry integrated model, Glob. Chang. Biol., 18(4), 1428–1440, doi:10.1111/j.1365-2486.2011.02587.x, 2012.

Zona, D., Oechel, W. C., Richards, J. H., Hastings, S., Kopetz, I., Ikawa, H. and Oberbauer, S.: Light-stress avoidance mechanisms in a Sphagnum-dominated wet coastal Arctic tundra ecosystem in Alaska, Ecology, 92(3), 633–644, doi:10.1890/10-0822.1, 2011.

Zona, D., Gioli, B., Commane, R., Lindaas, J., Wofsy, S. C., Miller, C. E., Dinardo, S. J., Dengel, S., Sweeney, C., Karion, A., Chang, R. Y.-W., Henderson, J. M., Murphy, P. C., Goodrich, J. P., Moreaux, V., Liljedahl, A., Watts, J. D., Kimball, J. S., Lipson, D. A. and Oechel, W. C.: Cold season emissions dominate the Arctic tundra methane budget., PNAS, 113(1), 40–45, doi:10.1073/pnas.1516017113, 2016.

Zubrzycki, S., Kutzbach, L., Grosse, G. and Desyatkin, A.: Organic carbon and total nitrogen stocks in soils of the Lena River Delta, Biogeosciences, 10(6), 3507–3524, doi:10.5194/bg-10-3507-2013, 2013.

List of Figures

List of Tables

Acknowledgements

This study was conducted within the scope of the research projects “CarboPerm” and “KoPf”, funded by the German Federal Ministry of Education and Research (respective grant numbers 03G0836A and 03F0764A). Further support was obtained by the Cluster of Excellence “CliSAP” (EXC177), University of Hamburg, funded by the DFG.

First of all, I wish to sincerely thank my supervisors Lars Kutzbach and Mathias Göckede for the laissez faire environment, in which I could greatly evolve and enjoy my work. Moreover, I am grateful for all of their supportive help as well as the fruitful discussion, not least during the advisory panel meetings with Felix Ament, whom I also owe many thanks.

My deep appreciation must be to Christian Wille for the valuable support during numerous discussions, which largely extended my scientific knowledge. I also remember our mutual time in the Lena River Delta as an enormously instructive period. Further, I would like to give a shout-out to Ben Runkle for the closed chamber data and the wicked flood walking during the massive spring flood event with cold feet during the bright nights of polar day.

I gratefully acknowledge the support and shenanigans with my faithful PhD companions Tim “Dreckhardt” Eckhardt and Josefine “Susefine” Walz. The countless laughs we had brought a great deal of relief in one or another working hour. Many thanks also goes to Lutz “Lutse Lotzelot” Beckebanze for contributing to a humorous atmosphere in our office, a lovely spot equipped with both the roof terrace and the frustration score board, the remedy for all of us. For giving helpful tips during the daily walks to the cafeteria, David Holl deserves my cordial thanks as well as the plenty of fizzy mate drinks, which eased many drowsy arvos.

None of this study would have been possible without the colleagues in Potsdam and Tiksi organising transport, accommodation and logistics. So I would like to express my gratitude to them and to the staff of the research station on Samoylov Island. A warm word of thanks must also go to the people in CliSAP for the financial support.

Heaps of thanks shall go to my family and friends, who accompanied me on the long-lasting journey of completing my academic education after 25 semesters. They provided a whole-hearted backing I do appreciate as well as the refreshing equalisation of sailing on the Alster or climbing and setting routes at Kilimanschanzo.

Finally, I thank in awe and admiration the fortunate coincidences in the cosmic framework that allowed the evolution of life on earth, e.g. the exceptional synergy of both Sun and Moon's stabilising sizes and distances to the Earth in the circumstellar habitable zone, the Solar System as a single star system enabling stable planetary orbits, the protective planet Jupiter gravitationally attracting potential impactors, the planet Saturn that prevented the inward migration of Jupiter in the early Solar System, the safe location of the Solar System far away from star forming regions plus its preservative motion speed in the Milky Way, the remote occurrence of titanic supernovae producing heavy elements that enriched the metallicity in the Milky Way through the galactic fountain, the nearly imperceptible anisotropies in the cosmic microwave background, the matter-antimatter asymmetry in the early universe and many more magnificent miracles that are yet to be discovered...